Università degli Studi di Ferrara

DOCTORAL COURSE IN ENGINEERING SCIENCE

CYCLE XXXIII

DIRECTOR: Prof. Stefano Trillo

STRUCTURAL DURABILITY ANALYSIS WITH RANDOM LOADINGS

Scientific Disciplinary Sector (SDS) ING/IND 14

Candidate

Dott. Julian Marcell Enzveiler Marques

(signature)

Supervisor

Prof. Denis Benasciutti

(signature)

Co-Supervisor

Prof. Roberto Tovo

(signature)

Years 2017/2020

PREFACE

In 2017, having successfully completed my Master's degree in Mechanical Engineering, I sent an e-mail to Roberto Tovo asking if I could do my PhD under his supervision. Denis Benasciutti replied on behalf of Roberto Tovo with a positive answer and I moved to Italy. After a few months studying random process theory, Denis Benasciutti and Roberto Tovo proposed me a PhD about the structural durability analysis with random loadings. I accepted that great opportunity and now I am very glad with my choice.

Having done so much work about structural durability analysis under random loadings, I attempted to summarize my best research activities of all PhD years in this thesis. In particular, my thesis provides five original contributions, which I consider to be very relevant for students, researchers and engineers.

i) A critical review and analysis of methods for the variability of the fatigue damage due to randomness of a stationary Gaussian random loading. Based on numerical simulations, best-fitting expressions in Chapter 4 are derived to relate the variance of the damage directly to bandwidth parameters of a power spectrum. The proposed expressions apply to narrow-band or wide-band processes.

ii) Two theoretical models (Chapter 5) to assess the variance of the fatigue damage in non-Gaussian random processes with narrow-band power spectrum. The models extend two solutions existing in the literature and restricted to Gaussian processes.

iii) A damage-based run test to verify the stationarity of a random time-history with finite time length. The proposed run test (Chapter 6) can detect not only changes in

the variance and mean levels (commonly found by existing solutions), but also the frequency content over time.

iv) Confidence interval expressions (Chapter 7) to enclose the exact (but unknown) expected damage when only one or few time-histories are available. The proposed confidence intervals for expected damage is also investigated by measuring the random loadings acting on an instrumented Mountain-bike.

v) A new algorithm (Chapter 8) to implement the Carpinteri-Spagnoli-Vantadori (CSV) multiaxial fatigue criterion for random loading and to shorten the computation time.

The first activity i) is also collected in articles [MAR20a,MAR19b,MAR19a]. It was presented at 48th Conference on Stress Analysis and Mechanical Engineering Design (AIAS 2019) in Perugia (Italy) and "Dodicesima giornata di studio Ettore Funaioli" in Bologna (Italy).

The second point ii) in the previous list is further addressed in articles [MAR21b,MAR21a,MAR20c]. This work was presented at the First Virtual Conference on Structural Integrity (VCSI 2020). It will also be presented at Fatigue 2021, Downing College, Cambridge, United Kingdom. This conference has been rescheduled from June 2020 and is planned to take place 29-31 March 2021, again at Downing College.

The damage-based run test in point iii) is applied to measured random time-histories records from a Mountain-bike and its results are collected in [MAR21c]. This research activity was first presented at AIAS 2020 Virtual Conference and the paper [MAR21c] is in press in IOP conf. ser., Mater. Sci. Eng.

Another research activity of PhD course, confidence intervals of damage when only one or few time-histories are available, is published in article [MAR20a]. A further work [MAR21c] investigates such confidence interval expressions applied to measured random time-histories. In fact, this activity [MAR21c] was also presented at AIAS 2020 Virtual Conference and it is in press in IOP conf. ser., Mater. Sci. Eng.

The last point in the previous list, a new algorithm to implement the CSV multiaxial fatigue criterion, is addressed in articles [MAR20b,BEN19a]. The 12th International Conference on Multiaxial Fatigue and Fracture (ICMFF12) in Bordeaux (France) was attended and the work in [BEN19a] was presented on 25 June 2019.

This thesis collects considerations, theories and results of all five contributions in the previous list. It is the best synthesis that I could obtain during my PhD.

It would be a great pleasure for me if this thesis were of some help to students, researchers and/or engineers, along the complex way of structural durability analysis with random loadings.

Ferrara, 24/1/2021

Julian Marcell Enzveiler Marques

LIST OF PUBLICATIONS

Marques JME, Benasciutti D. Variance of the fatigue damage in non-Gaussian stochastic processes with narrow-band power spectrum. Manuscript under review in Struct. Saf. 2021.

Marques JME. Confidence intervals for the expected damage in random loadings: Application to measured time-history records from a Mountain-bike. In press in IOP conf. ser., Mater. Sci. Eng. 2021.

Marques JME, Benasciutti D. A model to assess the variance of fatigue damage in high-kurtosis asymmetrical random loadings with narrow-band power spectrum. To be presented at FATIGUE 2021, Downing College, Cambridge, UK.

Marques JME, Benasciutti D, Tovo R. Variability of the fatigue damage due to the randomness of a stationary vibration loading. Int. J. Fatigue 2020; 141 105891.

Marques JME, Benasciutti D. More on variance of fatigue damage in non-Gaussian random loadings – effect of skewness and kurtosis. Proc. Struct. Integrity 2020; 25: 101-111.

Marques JME, Benasciutti D, Carpinteri A, Spagnoli A. An algorithm for fast critical plane search in computer-aided engineering durability analysis under multiaxial random loadings: Application to the Carpinteri-Spagnoli-Vantadori spectral method. Fatigue Fract. Eng. Mater. Struct. 2020;43(9):78–93.

Marques JME, Benasciutti D, Tovo R. Variance of fatigue damage in stationary random loadings: comparison between time- and frequency-domain results. Proc. Struct. Integrity 2019;24:398-07.

Benasciutti D, Marques JME. An efficient procedure to speed up critical plane search in multiaxial fatigue: Application to the Carpinteri-Spagnoli spectral criterion. MATEC Web. Conf. 2019;300:16003.

Marques JME, Benasciutti D, Tovo R. Uncertainties on fatigue damage under random loadings through spectral methods. In: Quaderni del DIEM - GMA - Atti di giornate di studio (12); 2019.

NOMENCLATURE

$\mathbf{a_3}$, $\mathbf{a_4}$	auxiliary vectors
A_{PC}	computer constant
b	half spectral width
c_1, c_2, c_3, c_4	fitting coefficients
C_{D}	coefficient of variation of damage
$\hat{C}_{\mathrm{D}}$	sample coefficient of variation of damage
d	fatigue damage of a half-cycle
$\overline{D}$	sample mean of fatigue damage
$D(T)$	fatigue damage in time period T
$D_{\mathrm{B}}(T_{\mathrm{B}})$	fatigue damage of block in time period T_{B}
e	root-mean-square error
$E[-]$	expected value
$E[d]^2$	expected half-cycle damage squared
$E[d^2]$	expected value of half-cycle damage squared
f	frequency (Hz)
$f_{\mathrm{a}}(s)$	probability density function of stress amplitudes s
f_{c}	main (or center) frequency
f_{n}	natural frequency
f_{p}	peak frequency
$f_{\mathrm{P_0,P_1}}(-)$	joint probability density function of two peaks

$G(-)$, $g(-)$	direct and inverse transformation
G	scaling factor of Wirsching's formula
g	gravity constant
h_3, h_4, $\widetilde{h_3}$, $\widetilde{h_4}$	parameters of Hermite's model
H_s	significant wave height
k, A	material constants of S-N curve
$n(T)$	number of counted half-cycles in T
N	size of time-history sample
N_B	number of blocks
N_f	number of cycles to failure
n_a	number of frequency points
n_b	number of frequency points
n_f	number of frequency points
n_p	number of planes
n_runs	number of simulation runs
n_ϕ, n_θ, n_ψ, n_γ	number of rotation angles $\phi, \theta, \psi, \gamma$
P	peak value
P_XYZ	initial reference frame with origin
$P_{\mathrm{X'Y'Z'}}$, $P_{\mathrm{X''Y''Z''}}$	rotated reference frames
$\mathrm{P}_{\widehat{123}} = P_{\mathrm{X''Y''Z''}}$	average principal directions
r	number of runs
$R_\mathrm{X}(\tau)$, $R_\mathrm{Z}(\tau)$	correlation function of $X(t)$ and $Z(t)$
$R_{\mathrm{d_0,d_l}}(l)$	autocorrelation function of half-cycle damage
$\mathbf{R}(\phi, \theta, \psi) = \mathbf{R}_\psi \mathbf{R}_\theta \mathbf{R}_\phi$	rotation matrices
$\widetilde{\mathbf{R}}(\delta, \gamma) = \mathbf{I}_6 \mathbf{R}_\delta \mathbf{R}_\gamma$	rotation matrices
s	stress amplitude of half-cycle
$S_\mathrm{X}(f)$, $S_\mathrm{Z}(f)$	Power Spectral Density of $X(t)$ and $Z(t)$

$S_{\mathrm{eq}}(f)$	PSD of equivalent stress $\sigma_{\mathrm{eq}}(t)$
$\mathbf{S}_{\mathrm{XYZ}}(f)$	PSD matrix in initial reference frame XYZ
$\mathbf{S}_{\mathrm{X'Y'Z'}}(f)$, $\mathbf{S}_{\mathrm{X''Y''Z''}}(f)$	PSD matrix in rotated reference frames X′Y′Z′ and X″Y″Z″
T	time length
T_1	simulation (or elapsed) time in one run
T_{B}	block length
T_{std}	simulation (or elapsed) time of standard algorithm
T_{tot}	simulation (or elapsed) time in multiple runs
T_{W}	peak period
$U(t)$	absolute displacement process
$W(t)$	base acceleration process
$(x_{\mathrm{p}}, x_{\mathrm{v}})$, $(z_{\mathrm{p}}, z_{\mathrm{v}})$	peak and valley (Gaussian, non-Gaussian)
$x(t)$, $z(t)$	Gaussian and non-Gaussian time-history
$X(t)$, $Z(t)$	Gaussian and non-Gaussian process
$(\phi, \theta, \psi, \delta, \gamma)$	rotation angles (variable values)
$(\phi^*, \theta^*, \psi^*, \delta^*, \gamma^*)$	rotation angles (solution, constant values)
$100(1-\beta)$	confidence level
α_1, α_2	bandwidth parameters
γ_3, γ_4	skewness, kurtosis
γ	peakedness parameter of JONSWAP spectrum
$\Gamma(-)$	gamma function
Δ	angular resolution
Δf	frequency resolution
ε	Vanmarcke's bandwidth parameter
ε_{r}	statistical error
ζ	damping factor
κ	scaling factor of Winterstein's model
λ_{m}	spectral moment of order m

$\boldsymbol{\lambda}_{\mathrm{m,XYZ}}$	matrix of spectral moments (order m) in P_{XYZ}
μ_{d}	mean value of half-cycle damage
μ_{r}	mean value of run r
μ_{X}, μ_{Z}	mean value of $X(t)$ and $Z(t)$
μ_{x}, μ_{z}	mean value of $x(t)$ and $z(t)$
ν_0	average frequency of upward crossings of the mean
ν_{p}	average frequency of peaks
$\rho_{\mathrm{X}}(\tau)$, $\rho_{\mathrm{Z}}(\tau)$	autocorrelation coefficient of $X(t)$ and $Z(t)$
$\rho_{\mathrm{d_o,d_l}}(l)$	autocorrelation coefficient of half-cycle damage
$\sigma_{\mathrm{af-1}}$, $\tau_{\mathrm{af-1}}$	tension, torsion fatigue limits (fully-reversed loading)
$\hat{\sigma}_{\mathrm{D}}^2$	sample variance of fatigue damage
σ_{D}^2	variance of fatigue damage
σ_{d}^2	variance of half-cycle damage
$\sigma_{\mathrm{eq}}(t)$	equivalent stress on critical plane
σ_{r}^2	variance of run r
$\boldsymbol{\sigma}_{\mathrm{XYZ}}(t)$	stress vector in reference frame P_{XYZ}
$\boldsymbol{\sigma}_{\mathrm{X'Y'Z'}}(t)$, $\boldsymbol{\sigma}_{\mathrm{X''Y''Z''}}(t)$	stress vector in rotated reference frames $P_{\mathrm{X'Y'Z'}}$, $P_{\mathrm{X''Y''Z''}}$
σ_{X}^2, σ_{Z}^2	variance of $X(t)$ and $Z(t)$
σ_{x}^2, σ_{z}^2	variance of $x(t)$ and $z(t)$
σ_{xx}, σ_{yy}, σ_{zz}	stress components along x-, y- and z-direction
τ_{yz}, τ_{xz}, τ_{xy}	shear stress in the yz-, xz- and xy-plane
τ	time lag
φ	scaling factor of Wirsching's formula
y^{G}, y^{nG}	(superscript) Gaussian, non-Gaussian
CAE	Computer Aided Engineering
CoV	Coefficient of variation
CSV	Carpinteri-Spagnoli-Vantadori

FE	Finite element
JPDF	Joint probability density function
NB	Narrow-band approximation
PDF	Probability density function
PSD	Power Spectral Density
RMS	Root-mean-squared
STFT	Short-Time Fourier Transform
TB	Tovo-Benasciutti

CONTENTS

Chapter 1

INTRODUCTION

Structural durability describes the strength behaviors of mechanical component and structures under service loads. Different kinds of loads can be considered in structural durability analysis, e.g. constant amplitude loadings and blocking loadings. However, the service loads in most engineering applications are random in nature, which are uncertain and not deterministic. Examples are a vehicle excited by road irregularity, a turbine exposed to wind, an offshore platform or ship under wave loadings. The engineering challenges in these and many other applications are figuring out the structural durability, which needs to consider the strength of component and its random loading. Therefore, engineers have not only to be aware of the in-service random loadings but also if fatigue failures may occur in mechanical components and structures.

Fatigue phenomenon is a complicate degradation process of materials (e.g. metals) that results in progressive damage. The fatigue damage accumulation observed in real structures and components is affected by many uncertainties. Examples are material randomness and load randomness [BEN05a,JOH99,TOV01]. For material randomness, statistical methods exist for considering the uncertainties. Besides, statistical tools for fatigue loading characterization may be used when loads vary randomly [TOV01].

The fatigue damage of structures and components under random loadings is generally estimated using random stress response acting at critical points. In practice, one

or more random stress time-histories are obtained by measurements. Successively, the time-domain approach may be applied to calculate the damage by processing directly such time-histories. This approach usually adopts rainflow counting method and Palmgren-Miner damage rule. Based on these well-established procedures, the time-domain approach usually requests long random time-history to achieve good confidence in estimating the damage.

Alternatively, the fatigue damage may be computed by frequency-domain approach. This approach leads to the so-called “spectral methods”, which idealizes the random stress time-histories as a random process. All time-histories may be viewed as an infinite collection (or ensemble), which represent a random process. The uniaxial or multiaxial random stress process is hypothesized to be stationary or non-stationary, ergodic or non-ergodic, Gaussian or non-Gaussian, and with narrow-band or wide-band Power Spectral Density (PSD) [LUT04,BEN10c,BEN18b]. If the process is stationary, it may be characterized by a PSD. Consequently, analytical expressions are then used to estimate the expected damage directly from a PSD. From a statistical point of view, the expected damage is the value that would result from averaging all the damage values of an infinite ensemble of time-histories.

Indeed, the expected damage computed from an infinite number of time-histories does not have a sampling variability. However, the damage computed from only one stationary random time-history of finite length has an intrinsic scatter. This damage value must be viewed as being one sample value out of an infinite collection. The scatter of fatigue damage is explained by the inherent randomness of each random time-history recorded, which has a random number of counted cycles, as well as randomly distributed amplitudes and mean values [MAR19b,MAR20a,MAR20c,MAR21a,MAR21b].

In any case, the damage value from one time-history of finite length is a random variable following a certain damage probability distribution. The variance around the expected damage is an essential property of the damage probability distribution – from now on, this will be called the “variance of the damage”. In the structural durability

analysis, estimating the variance of the damage becomes as much important as estimating the expected damage [MAR19a,MAR20a,MAR21b].

It is important to highlight that the expected damage and its variance may be calculated from Gaussian or even non-Gaussian random stress process. Non-Gaussian loadings are encountered, for example, in certain types of wind or wave loadings, or when the structure has a non-linear behavior that transforms a Gaussian input into a non-Gaussian output [MAR20c,MAR21a,MAR21b].

Furthermore, several methods to estimate fatigue damage or even variance of damage are usually restricted to random loadings assumed as stationary. Since this hypothesis is not valid for all structures and mechanical components, a non-parametric statistical method should be used to verify the stationarity of measured random time-histories. Methods existing in literature [ROU14] typically consider to the root-mean-square (RMS) value as the statistical parameters. However, they can detect change only in the variance and mean value of random time-history. It would be more effective to take into account the damage as statistical parameter so that it is possible to identify changes in variance, mean value and frequency content.

Similarly, to expected damage, the variance of the damage requires the knowledge of an infinite ensemble of time-histories (which in practice is never available). By contrast, in the situation with only few measured stationary time-histories, the infinite ensemble of time-histories is never known and expected damage and its variance can only be estimated. Nothing can be said about the “exact” expected damage and its variance of the whole time-history ensemble constituting the random process. In this situation, confidence interval can be used to bound the exact (but unknown) expected damage.

Finally, it is worth to mention that some mechanical components with complex geometries provide random stress responses which are multiaxial. Consequently, the structural durability analysis becomes obviously more complex. In these cases, spectral methods applied to multiaxial random loadings, which is characterized by a PSD matrix, can be used to compute fatigue damage. Spectral methods are classified based on the

concept of critical plane, stress invariants or equivalent stress [BEN16a,CAR17,BEL07, BEN08]. An example of critical plane method is the Carpinteri–Spagnoli–Vantadori (CSV) multiaxial fatigue criterion. Such a method may be implemented in a numerical routine that needs a sequence of five rotations to find the critical plane by ‘for/end’ loops. In some cases, where is not possible to predict the most critical regions (especially if of complex geometry), CSV algorithm seems to be slow [BEN19a,MAR20b]. An algorithm with analytical expressions to identify the critical plane and not making use of 'for/end' loops would much faster than the standard algorithm.

This thesis presents original contributions on the variance of damage in both Gaussian and non-Gaussian random loadings, statistical method to verify the stationarity, confidence interval of damage with one or few time-histories and last, but not least a new algorithm to shorten the computation time of CSV multiaxial spectral method. Figure 1.1 summarizes all contributions presented in this thesis and their connection to random loadings.

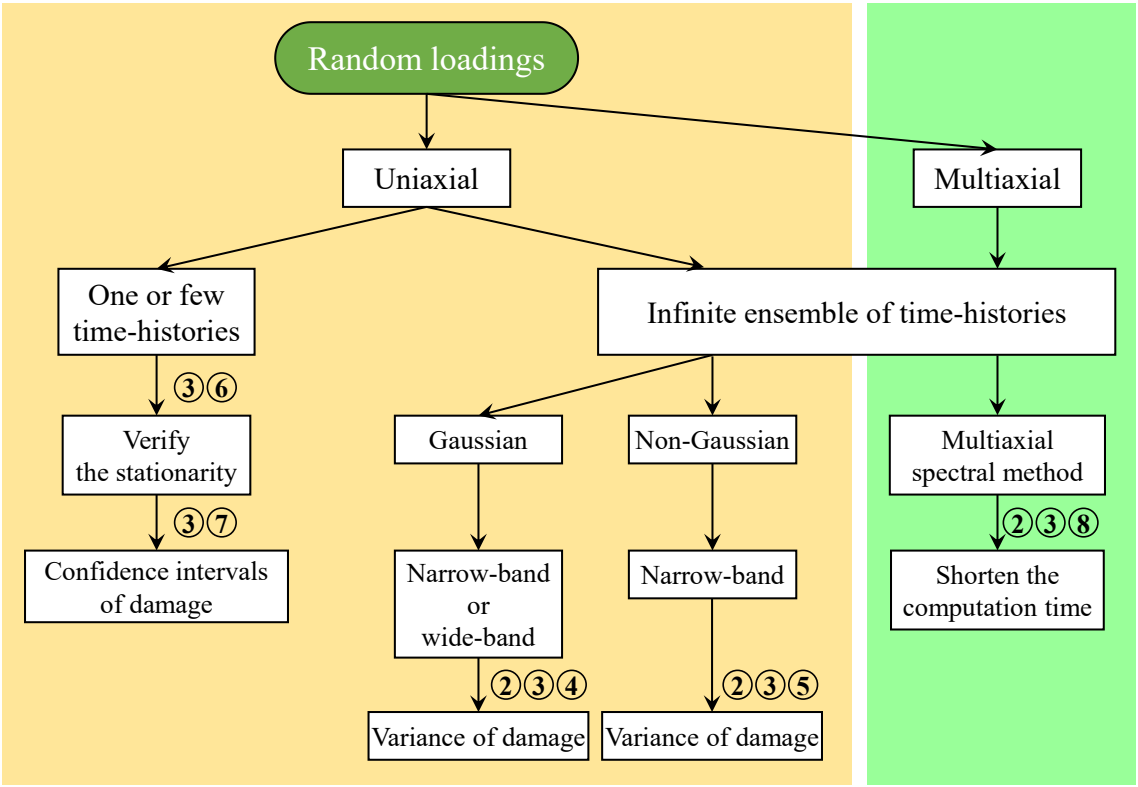

Figure 1.1. Overview of the thesis. Numbers indicate the chapters.

More particularly, empirical expressions are obtained for the variance of damage applied to narrow-band or wide-band Gaussian process. Four methods from the literature valid for narrow-band PSD, i.e. Mark and Crandall [MAR61], Bendat [BEN64], Madsen et al. [MAD86] and Low [LOW12], are reviewed and compared them with Monte Carlo simulations in the time- and frequency-domain. Based on simulation results, best-fitting expressions are derived to relate the variance of damage to the bandwidth parameter α_1.

In addition, two theoretical models to compute the variance of damage in narrow-band non-Gaussian random processes are proposed. The models proposed are based on a non-linear transformation that enables the models to calculate the variance. The correctness of the theoretical models is verified by Monte Carlo simulations.

The thesis also proposes an improved approach to verify the stationarity of time-histories. As an alternative to Rouillard's approach [ROU14] that considers RMS values,

the proposed statistical method considers the damage as the statistical parameters. The proposed method is then compared with Rouillard's using stationary and non-stationary simulation time-histories.

The confidence intervals are further derived to enclose the expected damage when only one or few time-histories are available. A numerical example considers the stress PSD in an offshore platform, as proposed by [WIR76]. The confidence intervals as well as the proposed method to verify the stationarity are also investigated by measuring the random loads acting on a Mountain-bike.

Finally, the thesis gives a new algorithm to implement the spectral method by CSV. The proposed algorithm reduces drastically the computation time when all the Finite Element (FE) model nodes are considered (especially with complex geometries).

All numerical simulations and routines are performed using MATLAB [MAT18]; the WAFO (Wave Analysis for Fatigue and Oceanography) toolbox is also used [BRO00].

1.1 OVERVIEW OF THE THESIS

While an overview of the thesis from random loadings to structural analysis is provided in Figure 1.1, each chapter is described in more details below. This description produces the main contents considered in the thesis.

1.1.1 Random process theory

In Chapter 2, the essential definitions of random process are presented to give a basis of later chapters, e.g. statistical moments of random process, autocorrelation coefficient function, Power Spectral Density (PSD) and its spectral moments. The random stress process in frequency-domain are presented in uniaxial and multiaxial.

1.1.2 Fatigue damage under random loading

Chapter 3 gives particular attention to the fatigue damage in time-domain and frequency-domain approaches. In time-domain, the fatigue damage is calculated by rainflow method and Palmgren-Miner rule and it strictly depends on a particular time-history of finite length. The fatigue damage is then defined as a random variable. In frequency-domain, the expected fatigue damage is computed from an infinite collection (or ensemble) of random time-histories. Indeed, this damage value, which does not have sampling variability, represents the damage of random process. Finally, Chapter 3 reviews Narrow-band approximation and Tovo-Benasciutti method to estimate the expected fatigue damage.

1.1.3 Variance of fatigue damage in Gaussian random loading

Chapter 4 reviews Mark and Crandall, Bendat, Madsen et al. and Low methods which allow estimating the variance of fatigue damage in narrow-band Gaussian process. Chapter 4 also gives a critical review of such methods and later compares them with Monte Carlo simulations in the time- and frequency-domain approaches. Based on all simulation results, best-fitting expressions were derived to relate the coefficient of variation of damage to the bandwidth parameter α_1. Following the best-fitting coefficients, the proposed expressions apply to a wide range of PSDs, from narrow-band to wide-band processes.

1.1.4 Variance of fatigue damage in non-Gaussian random loading

Two theoretical models to assess the variance of damage in non-Gaussian random process are presented in Chapter 5. The models extend two solutions existing in the literature and restricted to Gaussian processes. The models make use of a non-linear transformation that links Gaussian and non-Gaussian domains based on skewness and kurtosis coefficients, which are used to quantify the deviation from the Gaussian distribution. Monte Carlo

numerical simulations in time-domain are performed to verify the correctness of the proposed non-Gaussian models. Finally, Chapter 5 investigates the sensitivity of the variance of fatigue damage to the values of skewness, kurtosis, and inverse slope of the S-N curve.

1.1.5 Test of stationarity of random loading

In Chapter 6, a non-parametric statistic method (e.g. run test) is proposed to verify the stationarity of time-histories with finite length. In summary, the run test proceeds a sequence of non-overlapping blocks. For each block, a value is calculated for the statistical parameter under investigation. The Rouillard's approach considers RMS values for each independent block as the statistical parameters. As an improvement to Rouillard's approach, the proposed run test computes the damage values for each block in which can detect changes not only in the variance and mean value of random time-history but also in the frequency content.

1.1.6 Variability of fatigue damage: A real-world scenario

Chapter 7 proposes an approach to estimate the statistical variability of damage computed from only one or few time-histories. For both cases, confidence interval expressions are derived to enclose the exact (but unknown) expected damage. A numerical example, which considers a stress PSD in an offshore platform [WIN76], verifies the correctness of both confidence interval expressions. The confidence intervals for the expected damage are also investigated by measuring the random loads acting on a Mountain-bike. Several time-histories were measured directly in the Mountain-bike in a typical north Italian off-road track. The stationarity hypothesis of all measured time-history records was also verified by proposed damage-based run test in Chapter 6. Finally, a calibrator sample damage checks whether the confidence intervals correctly encloses the expected damage.

1.1.7 Multiaxial random loading: Application to the CSV criterion

Chapter 8 proposes a new algorithm for implementing the CSV criterion and to shorten the computation time. In most cases, the analysis of all nodal results in an FE model is not needed because it may be restricted to small subsets of nodes from the most stressed regions; but, if it is not possible to predict *a priori* which regions are the most critical ones, such a new algorithm significantly reduces the computation time for the critical plane search. This goal was achieved in two phases. The first one consisted in computing the analytical expressions of only those spectral moments used for determining the largest variance and expected largest peak of normal/shear stress in any rotated reference frame at a given point. The second one was to employ those analytical expressions into a numerical routine that, dismissing “for/end” loops, is much faster than the standard algorithm.

The new approach applied to the CSV criterion has a general validity. Indeed, theoretical framework of this approach may apply to any multiaxial spectral method in which the critical plane or the direction of maximum stress variance is identified through rotation angles or direction cosines.

Chapter 2

RANDOM PROCESS THEORY

2.1 INTRODUCTION

Mechanical structures are often exposed to random loadings during their service life. For example, a car travelling on an irregularity road is excited by random loading, where the term "random" simply means that, at each time instant, the load value is inherently uncertain and not predictable exactly [BEN18b]. In structural durability analysis, random excitations play an important role to characterize the random stress response of such structures. The random stress process as well as fatigue damage—which will be addressed in Chapter 3—can be tackled in two alternative fields: time-domain or frequency-domain approach. Stationary random stress process is more usefully studied in frequency domain than time-domain due to better description of process [WIN95,BEN05a,BEN05b].

This chapter discusses elementary concepts of random process to form a foundation for applications to analysis in later chapters. It is expected that the reader is familiar with the theory of probability, random variables and their probability distributions. Otherwise, the reader is referred to texts as [WIN95,LUT04,BEN10c].

The random processes characterization in time-domain are first presented as stationary and ergodic with Gaussian or non-Gaussian distribution. A useful way to consider a random process $X(t)$ is in terms of all possible time-histories or infinite

collection of time-histories $x_{\mathrm{i}}(t)$, $\mathrm{i} = 1,2,3 \ldots \infty$. It is typically called an ensemble. Hereafter, both uniaxial and multiaxial random stress, which are modelled as stationary random process $X(t)$, are exploited in frequency-domain. Since multiaxial random stress in frequency-domain is described by uniaxial components and based on reformulations of classical fatigue criteria in time-domain, uniaxial and multiaxial stress are addressed separately.

2.2 BASIC CONCEPTS

Any measured random loading on an engineering structure may be assumed as one of the many random loadings that could be measured. The stress dynamic response of this structure is usually a single random stress time-history out of an infinite collection. In this example, as in many others, the set of all possible random stress time-histories $x_{\mathrm{i}}(t)$, $\mathrm{i} = 1,2,3 \ldots \infty$ should be modelled as an infinite collection (or ensemble). This idea of infinite time-histories allows the stationary random process $X(t)$, $-\infty < t < \infty$ to be exploited.

The first statistical quantity of the random process $X(t)$ is the ensemble mean value or expected value $\mu_{\mathrm{X}} = E[X(t)]$, where symbol $E[-]$ is the probabilistic expectation. It is also called as first moment of $X(t)$ [BEN10c,LUT04]. Similarly, the expected value of $X(t)$ squared $E[X^2(t)]$ is commonly called the second moment. This term $E[X^2(t)]$ may be subtracted by the mean-squared value μ_X^2 to define the second central moment, or the variance of the process $\sigma_{\mathrm{X}}^2 = \mathrm{Var}[X(t)]$ [BEN10c,LUT04]:

$$\sigma_{\mathrm{X}}^2 = E[(X(t) - \mu_{\mathrm{X}})^2] = E[X^2(t)] - \mu_{\mathrm{X}}^2 \tag{2.1}$$

The standardized third and fourth central moment of the random process are known as skewness γ_3 and kurtosis γ_4 [LUT04]:

$$\gamma_3 = \frac{E[(Z(t) - \mu_Z)^3]}{\sigma_Z^3} \; ; \qquad \gamma_4 = \frac{E[(Z(t) - \mu_Z)^4]}{\sigma_Z^4} \tag{2.2}$$

A stationary random process $X(t)$ is completely defined with $\gamma_3 = 0$ and $\gamma_4 = 3$ if its values follow a normal (or Gaussian) distribution around its mean value. On the contrary a non-Gaussian process $Z(t)$ deviates from the Gaussian distribution when $\gamma_3 \neq 0$ and $\gamma_4 \neq 3$. The skewness and kurtosis are parameters devised to measure the degree of non-Gaussianity. The skewness measures the asymmetry degree of a non-Gaussian distribution. The kurtosis measures the contribution of tails: values away from the mean can be either higher ($\gamma_4 > 3$, leptokurtic case) or lower ($\gamma_4 < 3$, platykurtic case) than the values from a Gaussian distribution.

Under the hypothesis of stationarity, the random process $X(t)$ is uniquely characterized in the time-domain by the autocorrelation function [BEN10c,LUT04]:

$$R_X(\tau) = E[X(t)X(t+\tau)] \tag{2.3}$$

in which τ is a time-lag. The autocorrelation function $R_X(\tau)$ can be normalized to the mean-squared value μ_X^2 and variance σ_X^2 of the process to obtain the autocorrelation coefficient function (or normalized autocorrelation function) [BEN10c,LUT04]:

$$\rho_X(\tau) = \frac{R_X(\tau) - \mu_X^2}{\sigma_X^2} \tag{2.4}$$

Eq. (2.4) indicates a linear relationship between the two random variables of the same process separated by a time difference τ. For all τ, the autocorrelation coefficient satisfies $-1 \leq \rho_X(\tau) \leq 1$. A perfect linear relationship (correlated) is provided by $\rho_X(\tau) = \pm 1$ while the other extreme $\rho_X(\tau) = 0$ is called uncorrelated random variables.

2.3 SPECTRAL PROPERTIES

After a short account on time-domain description of the random process, which may be a mechanical random stress process, this section introduces a few concepts of stationary random stress process in the frequency-domain.

2.3.1 Uniaxial random stress

The uniaxial stationary random stress $X(t)$ is described in frequency-domain by a one-sided Power Spectral Density (PSD) or power spectrum function $S_{\mathrm{X}}(f)$, $0 < f < \infty$. This function constitutes a Fourier transform pair (Wiener–Khintchine relations) [WIR95]:

$$S_{\mathrm{X}}(f) = 4\int_0^{\infty} R_X(\tau)\, cos(2\pi f\tau)\, \mathrm{d}\tau \tag{2.5}$$

where f is the frequency in Hertz. The PSD function of a narrow-band process is centered on a restrict range of frequencies, while wide-band process extends over a wider range of frequencies.

The spectral moments are commonly used to characterize the PSD in frequency-domain [WIR95]:

$$\lambda_{\mathrm{m}} = \int_0^{\infty} (2\pi f)^{\mathrm{m}}\, S_{\mathrm{X}}(f)\, \mathrm{d}f, \quad m = 0,1,2 \ldots \tag{2.6}$$

They are useful for describing some statistical properties of random process $X(t)$ in the time-domain. For example, the variances for the process and its derivatives $X(t)$, $\dot{X}(t)$, $\ddot{X}(t)$ are $\sigma_{\mathrm{X}}^2 = \lambda_0$, $\sigma_{\dot{\mathrm{X}}}^2 = \lambda_2$ and $\sigma_{\ddot{\mathrm{X}}}^2 = \lambda_4$, respectively.

Spectral moments are also used to compute the average frequency of upward crossings of the mean, ν_0, and peaks, ν_p [WIR95]:

$$\nu_0 = \frac{1}{2\pi}\sqrt{\frac{\lambda_2}{\lambda_0}}, \qquad \nu_\mathrm{p} = \frac{1}{2\pi}\sqrt{\frac{\lambda_4}{\lambda_2}} \tag{2.7}$$

The bandwidth parameters, which are calculated by spectral moments, are typically exploited to classify the PSD. One of them is the bandwidth parameter proposed by Vanmarcke [VAN72]:

$$\varepsilon = \sqrt{1 - \frac{\lambda_1^2}{\lambda_0 \lambda_2}} \tag{2.8}$$

When the process is narrowband, $\varepsilon \to 0$ is close to zero; conversely, $\varepsilon \to 1$ for wideband processes. However, the most used bandwidth parameters are [WIR95]:

$$\alpha_1 = \frac{\lambda_1}{\sqrt{\lambda_0 \lambda_2}}, \qquad \alpha_2 = \frac{\lambda_2}{\sqrt{\lambda_0 \lambda_4}} \tag{2.9}$$

In contrast to Vanmarcke's bandwidth parameter ε, both parameters are close to unity $\alpha_1 \to 1$, $\alpha_2 \to 1$ when the process is narrow-band (PSD with a well-defined frequency). Conversely, they tend to zero $\alpha_1 \to 0$, $\alpha_2 \to 0$ when the process is wideband (PSD over a larger frequency range).

In addition to provide a measure of spectral width, the quantity α_1 is called the groupness parameter in ocean engineering [LON84,RYC03] and it is related to the definition and properties of the envelope of a random process [VAN72]. Instead, the parameter α_2 is equal to the irregularity factor $IF = \nu_0/\nu_\mathrm{p}$ for Gaussian case, defined as the ratio of the average frequency of upward crossings of the mean to the average

frequency of peaks. One disadvantage of α_2, as compared with α_1, is its increased sensitivity to high-frequency components of the PSD function [LUT04].

2.3.2 Multiaxial random stress

The previous description of uniaxial random stress may be extended to multiaxial random stress in frequency-domain. It is described by six non-redundant components of normal stress and shear stress, which are conveniently grouped into the vector $\boldsymbol{\sigma}_{\mathrm{XYZ}}(t) = \left[\sigma_{\mathrm{xx}}(t), \sigma_{\mathrm{yy}}(t), \sigma_{\mathrm{zz}}(t), \tau_{\mathrm{yz}}(t), \tau_{\mathrm{xz}}(t), \tau_{\mathrm{xy}}(t)\right]^{\mathrm{T}}$. The subscript XYZ specifies that $\boldsymbol{\sigma}_{\mathrm{XYZ}}(t)$ refers to the reference frame P_{XYZ}, with origin at a material given point. If every stress component is a stationary random process, vector $\boldsymbol{\sigma}_{\mathrm{XYZ}}(t)$ is characterized by a 6×6 PSD matrix [BEN19a,BEN19b,MAR20b]:

$$\begin{aligned}\mathbf{S}_{\mathrm{XYZ}}(f) &= \begin{bmatrix} S_{\mathrm{xx}} & S_{\mathrm{xx,yy}} & S_{\mathrm{xx,zz}} & S_{\mathrm{xx,yz}} & S_{\mathrm{xx,xz}} & S_{\mathrm{xx,xy}} \\ S^*_{\mathrm{xx,yy}} & S_{\mathrm{yy}} & S_{\mathrm{yy,zz}} & S_{\mathrm{yy,yz}} & S_{\mathrm{yy,xz}} & S_{\mathrm{yy,xy}} \\ S^*_{\mathrm{xx,zz}} & S^*_{\mathrm{yy,zz}} & S_{\mathrm{zz}} & S_{\mathrm{zz,yz}} & S_{\mathrm{zz,xz}} & S_{\mathrm{zz,xy}} \\ S^*_{\mathrm{xx,yz}} & S^*_{\mathrm{yy,yz}} & S^*_{\mathrm{zz,yz}} & S_{\mathrm{yz}} & S_{\mathrm{yz,xz}} & S_{\mathrm{yz,xy}} \\ S^*_{\mathrm{xx,xz}} & S^*_{\mathrm{yy,xz}} & S^*_{\mathrm{zz,xz}} & S^*_{\mathrm{yz,xz}} & S_{\mathrm{xz}} & S_{\mathrm{xz,xy}} \\ S^*_{\mathrm{xx,xy}} & S^*_{\mathrm{yy,xy}} & S^*_{\mathrm{zz,xy}} & S^*_{\mathrm{yz,xy}} & S^*_{\mathrm{xz,xy}} & S_{\mathrm{xy}} \end{bmatrix} \\ &= \begin{bmatrix} S_{11} & S_{12} & S_{13} & S_{14} & S_{15} & S_{16} \\ S^*_{21} & S_{22} & S_{23} & S_{24} & S_{25} & S_{26} \\ S^*_{31} & S^*_{32} & S_{33} & S_{34} & S_{35} & S_{36} \\ S^*_{41} & S^*_{42} & S^*_{43} & S_{44} & S_{45} & S_{46} \\ S^*_{51} & S^*_{52} & S^*_{53} & S^*_{54} & S_{55} & S_{56} \\ S^*_{61} & S^*_{62} & S^*_{63} & S^*_{64} & S^*_{65} & S_{66} \end{bmatrix}\end{aligned} \tag{2.10}$$

The order of elements in $\mathbf{S}_{\mathrm{XYZ}}(f)$ must strictly correspond to the order of stress components in $\boldsymbol{\sigma}_{\mathrm{XYZ}}(t)$. The elements on the main diagonal, $S_{\mathrm{ii}}(f)$, are auto-PSDs, whereas those outside the diagonal, $S_{\mathrm{ij}}(f)$ $(i \neq j)$, are cross-PSDs. Matrix $\mathbf{S}_{\mathrm{XYZ}}(f)$ is Hermitian as $S_{\mathrm{ij}}(f) = S^*_{\mathrm{ji}}(f)$, where $*$ means complex conjugate. Some elements in

$\mathbf{S}_{\mathrm{XYZ}}(f)$ can be zero if the stress state is biaxial, or even uniaxial, for more details [BEN19b].

Each element in matrix $\mathbf{S}_{\mathrm{XYZ}}(f)$ is a one-sided spectrum, which admits a description through its set of spectral moments. By applying the definition in Eq. (2.6) to the whole PSD matrix $\mathbf{S}_{\mathrm{XYZ}}(f)$ yields the set of *m*-th order spectral moments, grouped in the following symmetric matrix [BEN19a,BEN19b,MAR20b]:

$$\boldsymbol{\lambda}_{\mathrm{m,XYZ}} = \begin{bmatrix} \lambda_{\mathrm{m},11} & \lambda_{\mathrm{m},12} & \lambda_{\mathrm{m},13} & \lambda_{\mathrm{m},14} & \lambda_{\mathrm{m},15} & \lambda_{\mathrm{m},16} \\ \lambda_{\mathrm{m},21} & \lambda_{\mathrm{m},22} & \lambda_{\mathrm{m},23} & \lambda_{\mathrm{m},24} & \lambda_{\mathrm{m},25} & \lambda_{\mathrm{m},26} \\ \lambda_{\mathrm{m},31} & \lambda_{\mathrm{m},32} & \lambda_{\mathrm{m},33} & \lambda_{\mathrm{m},34} & \lambda_{\mathrm{m},35} & \lambda_{\mathrm{m},36} \\ \lambda_{\mathrm{m},41} & \lambda_{\mathrm{m},42} & \lambda_{\mathrm{m},43} & \lambda_{\mathrm{m},44} & \lambda_{\mathrm{m},45} & \lambda_{\mathrm{m},46} \\ \lambda_{\mathrm{m},51} & \lambda_{\mathrm{m},52} & \lambda_{\mathrm{m},53} & \lambda_{\mathrm{m},54} & \lambda_{\mathrm{m},55} & \lambda_{\mathrm{m},56} \\ \lambda_{\mathrm{m},61} & \lambda_{\mathrm{m},62} & \lambda_{\mathrm{m},63} & \lambda_{\mathrm{m},64} & \lambda_{\mathrm{m},65} & \lambda_{\mathrm{m},66} \end{bmatrix}, \quad m = 0, 1, 2 \ldots \quad (2.11)$$

Analogous to $\mathbf{S}_{\mathrm{XYZ}}(f)$, elements on the main diagonal, $\lambda_{\mathrm{m,ii}}(f)$, are the moments of auto-PSDs and outside the diagonal elements $\lambda_{\mathrm{m,ij}}(f)$ $(i \neq j)$ are the moments of cross-PSDs [BEN19a,BEN19b,MAR20b]:

$$\begin{aligned} \lambda_{\mathrm{m,ii}} &= \int_0^\infty f^{\mathrm{m}} S_{\mathrm{ii}}(f)\, df; \\ \lambda_{\mathrm{m,ij}} &= \int_0^\infty f^{\mathrm{m}} S_{\mathrm{ij}}(f)\, df = \int_0^\infty f^{\mathrm{m}} S_{\mathrm{ji}}^*(f)\, df \qquad (i \neq j) \end{aligned} \quad (2.12)$$

Note that the zero-order moments $(m = 0)$ equal to the variance and covariance of stress components $\lambda_{0,\mathrm{ii}} = \mathrm{Var}[\sigma_{\mathrm{i}}(t)]$ and $\lambda_{0,\mathrm{ij}} = \mathrm{Cov}[\sigma_{\mathrm{i}}(t), \sigma_{\mathrm{j}}(t)]$, respectevely. Different terms are obtained for each value of m (e.g. $\lambda_{0,\mathrm{ii}} \neq \lambda_{2,\mathrm{ii}}$ for any i). Consequently, matrix $\boldsymbol{\lambda}_{\mathrm{m,XYZ}}$ changes according to *m*-th order of the spectral moments. The zero-order matrix agrees with the covariance matrix $\boldsymbol{\lambda}_{0,\mathrm{XYZ}} = \mathbf{C}_{\mathrm{XYZ}}$ of vector

$\boldsymbol{\sigma}_{\mathrm{XYZ}}(t)$, in which each element is $\mathbf{C}_{\mathrm{XYZ,ij}} = \mathrm{Cov}\left(\boldsymbol{\sigma}_{\mathrm{XYZ,i}}, \boldsymbol{\sigma}_{\mathrm{XYZ,j}}\right)$. Also, the second-order moment matrix $\boldsymbol{\lambda}_{2,\mathrm{XYZ}}$ coincides with the covariance of first derivative vector $\dot{\boldsymbol{\sigma}}_{\mathrm{XYZ}}(t)$.

Chapter 3

FATIGUE DAMAGE UNDER RANDOM LOADING

3.1 INTRODUCTION

The previous chapter introduced a few concepts of random process in time and frequency-domain. Simple classifications of process are assumed for example stationary, ergodic and Gaussian or non-Gaussian distribution. The random process theory is also used to describe the uniaxial and multiaxial random stress response, which are of interest to engineers.

The random loading acting on a mechanical structure may be modelled as a random process. The randomness of the loading seems to provide a larger scatter in estimating the fatigue damage compared to other uncertainties [TOV01,LOW12, LOW14a]. In any case, for structural durability analysis, an efficient procedure to estimate fatigue damage of structures subjected to random loadings needs to take into account.

Indeed, fatigue damage can be estimated in time or frequency-domain approach. The time-domain computes the damage by processing directly one or more measured time-histories. It is based on well-established procedures, i.e. rainflow counting method and Palmgren-Miner rule. The rainflow method is the most accurate counting procedure and its stress amplitudes distribution may be represented by an amplitude histogram or a

loading spectrum. Under the linear damage rule as Palmgren-Miner, the damage is computed given a measured time-history. An acceptable small statistical scatter of damage is usually achieved by performing one sufficiently long or many different measurements [BEN05a,BEN05b], which may be costly and time-consuming.

On the other hand, the frequency-domain approach makes use of mathematical expressions (e.g. Narrow-band approximation and Tovo-Benasciutti method) to calculate the expected damage by a Power Spectral Density (PSD) [BEN05a,BEN05b,BEN18b]. A more complex theory is required to estimate the rainflow distribution and then approximating the damage under the linear damage hypothesis. From a statistical point of view, the expected damage represents the value that would result from averaging all the damage values of an infinite ensemble of time-histories.

This chapter reviews key parameters of mechanical materials, rainflow counting method, histogram and loading spectrum of rainflow, fatigue damage under Palmgren-miner rule and expected fatigue damage. Due to its important in subsequent chapters, special attention is paid to the fatigue damage in time-domain and frequency-domain. In frequency-domain, Narrow-band approximation is only appropriate for narrow-band processes, while Tovo-Benasciutti method is also appropriate for wide-band random processes. Although several spectral methods have been developed in the past two decades, e.g., Dirlik [DIR85], Gao-Moan [GAO08], Petrucci-Zuccarello [PET04], Tovo-Benasciutti [BEN05b], Wirsching-Light [WIR80] and Zhao-Baker [ZHA92]; Dirlik and Tovo-Benasciutti method demonstrated to be more accurate than the others [CAP20,MRŠ13]. For this reason, it is reviewed in this chapter and will be used as a reference in later chapters when estimating the expected damage for wide-band random processes.

3.2 MATERIAL PROPERTIES

The material used in engineering components and structures may be characterized by a few parameters. These parameters are defined by experimental tests in laboratory. Indeed, they are determined by the fatigue resistance expressed as the number of cycles to failure under constant amplitude loading. Mathematically, the fatigue resistance is a power-law function, which is called S-N curve or Wöhler curve [SCH96]:

$$s^{\mathrm{k}} N_{\mathrm{f}} = A \tag{3.1}$$

where A is the fatigue strength of the material, k the damage exponent or inverse slope, and N_{f} is the number of cycles to failure at a given stress amplitude s. The S-N curve is represented by a straight-line in double-logarithmic scale. However, some materials exhibit a fatigue limit, below which failure appears not to occur. In such cases, the log-log diagram is characterized by two straight-lines as N_{f} tending to infinity under low stress amplitudes.

In laboratory, material parameters A and k may present a large scatter using exactly the same controlled conditions (e.g. loading kinds). Consequently, these parameters should be modelled as random variables by statistical methods [LIN87,SVE97]. For example, parameters A and k may represent best-fitting estimates of experimental data considering their statistical variability, see [ISO17].

3.3 RAINFLOW COUNTING METHOD

The rainflow is the most popular and used counting method to determine the distribution of cycles and the fatigue damage of structures and components under random loadings. It has been recognized as the most accurate in identifying damaging events in complex loadings [DOW72]. Different definitions of rainflow counting algorithms, which are similar to each other, can be found in literature. They include the "pagoda-roof" method

proposed by Matsuishi and Endo [MAT68], the "3-points" algorithm [AST85] or the alternative "4-points" algorithm [AMZ94], and the non-recursive definition proposed by Rychlik [RYC87]. All different algorithms provide the same cycle counts if the random time-history begins and ends with its maximum peak. Here, the common rainflow method described in the ASTM standard, "3-points" algorithm, is analyzed.

The method considers a sequence of local minima (valley) and maxima (peak) of time-history, which are used to form and to compare stress ranges. Rules for the "3-points" algorithm are illustrated in Figure 1.1, where X denotes the range under consideration, Y is the previous range adjacent to X and S is the starting point.

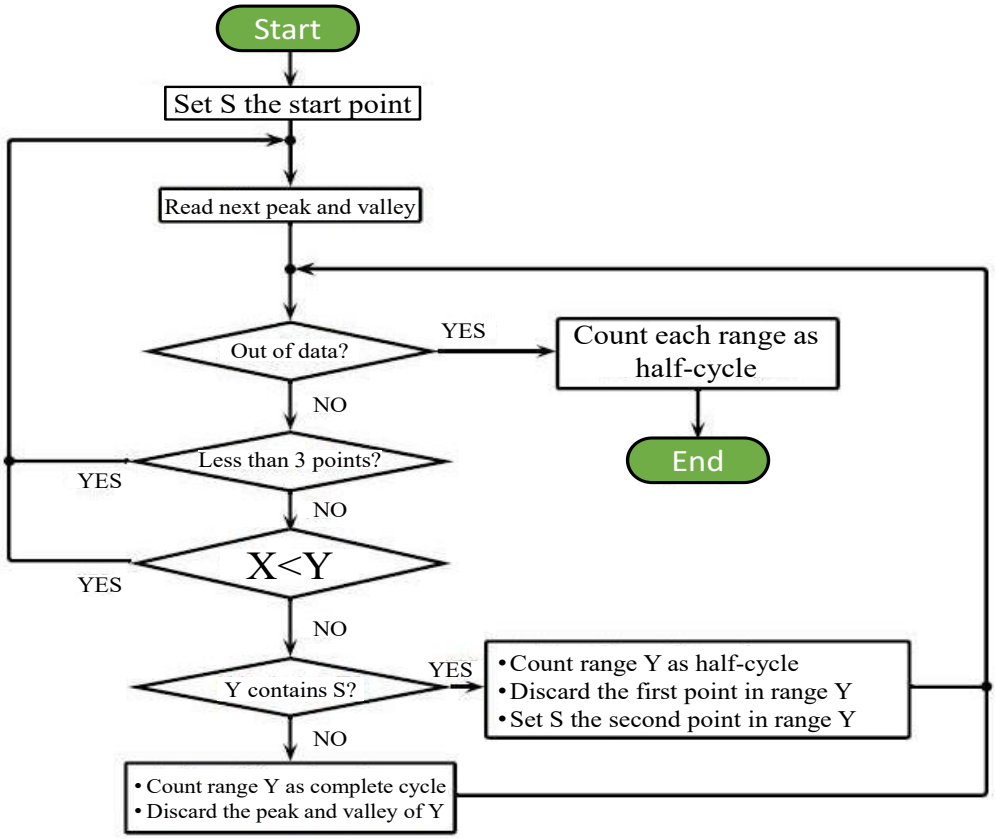

Figure 3.1. Rainflow counting rules ("3-points" algorithm).

Figure 3.2 provides a simple example of the "3-points" algorithm applied to a time-history. The first two ranges (ranges AB and BC) are counted as half-cycles (all contain the starting point S) and are then removed; ranges EF and HI are counted as complete cycles; the remaining ranges (residual) are CD, DG and GJ.

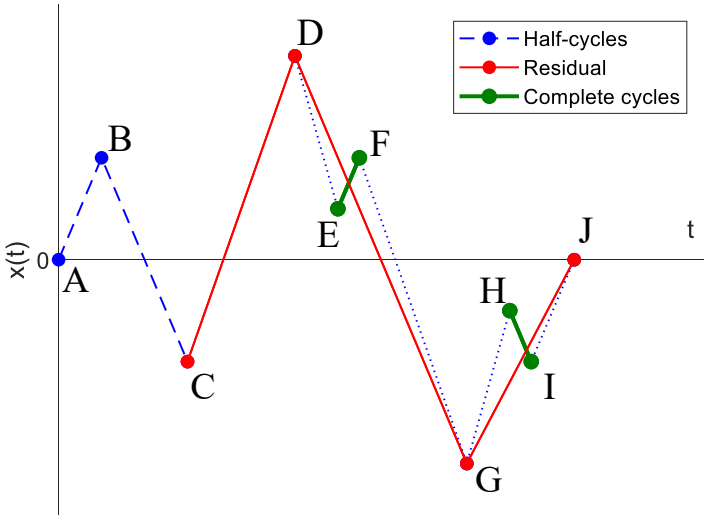

Figure 3.2. "3-points" algorithm applied to a time-history.

Note that the rainflow method successively extracts the half-cycles and complete cycles from a sequence, which describes the stress-strain hysteresis loops [MAT68]. When the rainflow method does not start the counting from the largest peak or the lowest valley in the time-history, the stress-strain does not close the path, see Figure 3.3.

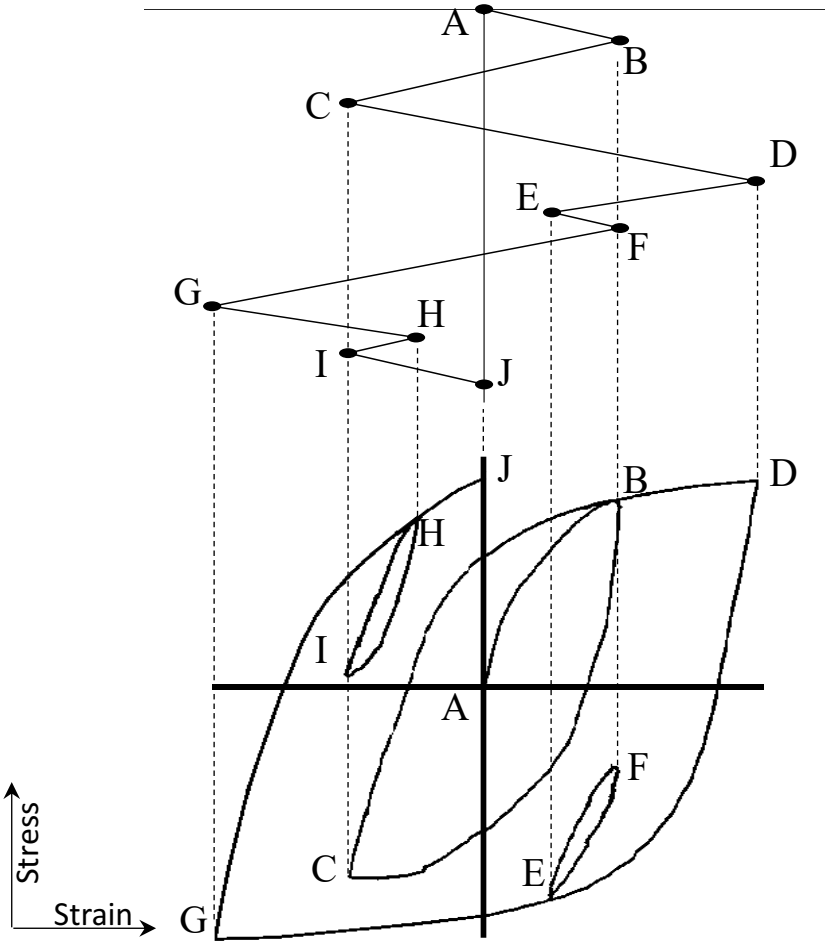

Figure 3.3. Stress-strain hysteresis loops for the time-history of Figure 3.2.

The method, finally, collects the half-cycles and complete cycles and tabulates their ranges, their means, and the points at which they start and end. These results can then be used to construct an amplitude histogram of cycles or loading (or cumulative) spectrum.

3.4 AMPLITUDE HISTOGRAM AND LOADING SPECTRUM

The amplitudes of a random time-history $x(t)$ are often represented in the form of a histogram or a loading (or cumulative) spectrum $C(s)$. For a random time-history $x(t)$ of duration T, the loading spectrum is:

$$C(s) = \frac{n(T)[1 - F(s)]}{2} \tag{3.2}$$

where $n(T)$ the total number of half-cycles counted in time T and $F(s)$ the amplitude distribution of counted cycles. Figure 3.4(a) shows the rainflow amplitude histogram from a particular time-history $x(t)$, while Figure 3.4(b) corresponds to its cumulated cycles.

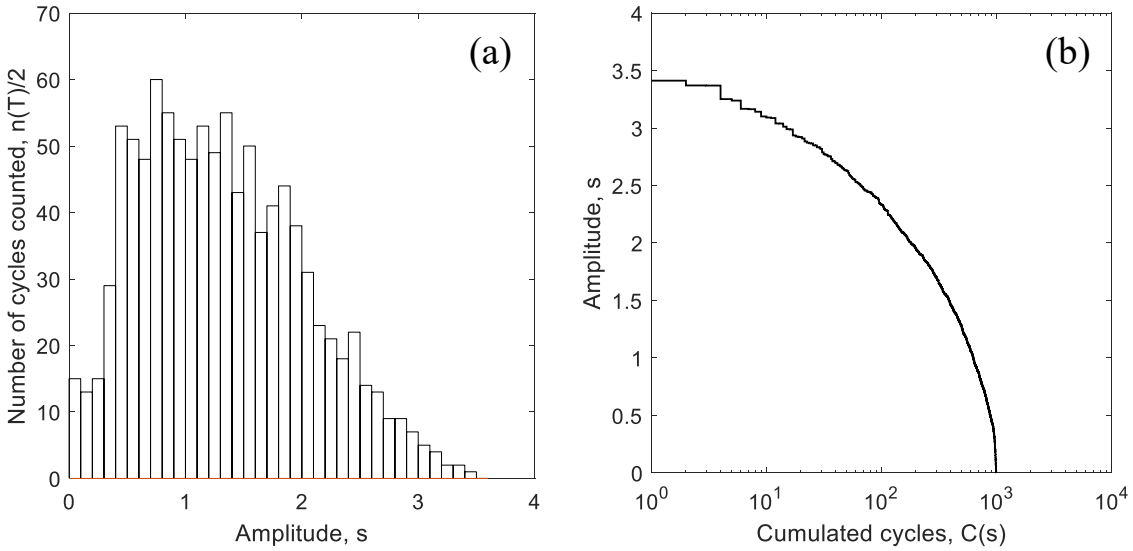

Figure 3.4. Rainflow cycles: (a) amplitude histogram and (b) loading spectrum.

In laboratory, standardized loading spectra are used to conducted tests by virtual simulation programs. They reproduce real service conditions of structures and

components (e.g. vehicles and car suspension systems), which encompass all possible most damaging service loadings [BER02].

3.5 PALMGREN-MINER RULE

Palmgren-Miner rule is a linear damage hypothesis which sums up the damage contribution from each cycle or half-cycle during time T. Thus, damage in T caused by a random loading under Palmgren-Miner rule is given by:

$$D(T) = \sum_{\mathrm{i}=0}^{\mathrm{n(T)}-1} d_{\mathrm{i}} = \sum_{\mathrm{i}=0}^{\mathrm{n(T)}-1} \frac{s_{\mathrm{i}}^{\mathrm{k}}}{2A} \tag{3.3}$$

where d_{i} is the damage of the i-th half-cycle, s_{i} is the stress amplitude, and A and k are material constants of the S–N curve $s^k N = A$. Fatigue failures often occur when the damage $D(T)$ reaches a critical value. Critical damage value is often assumed unity. Experimental results given by Miner however highlighted that the critical $D(T)$ is not unity [MIN45].

Damage $D(T)$ in Eq. (3.3) strictly depends on the particular time-history $x(t)$ of time duration T. This means that $D(T)$ would take a different value if $x(t)$ were longer, or if it were computed from another time-history under same conditions. The damage $D(T)$ is then a random variable. The fact that $D(T)$ is a random variable is due to the randomness in the stress amplitude s values and in the number of half-cycles counted $n(T)$, which both take on slightly different values from one time-history to another [MAR19b, MAR20a].

3.6 EXPECTED FATIGUE DAMAGE

The expected fatigue damage denotes the damage $D(T)$ computed from an infinite collection (or ensemble) of random time-histories. Indeed, this damage value thus represents the damage of random process $X(t)$. The expected fatigue damage is calculated by taking the expectation of Eq. (3.3):

$$E[D(T)] = E\left[\sum_{\mathrm{i}=0}^{\mathrm{n(T)}-1} d_{\mathrm{i}}\right] = E[n(T)]\frac{E\left[s^{\mathrm{k}}\right]}{2A} \tag{3.4}$$

where $E[n(T)]$ is the expected number of half-cycles counted in T and the term $E[d] = E\left[s^{\mathrm{k}}\right]/2A$ is the expected damage per half-cycle.

The number of half-cycles $n(T)$ is usually assumed deterministic for the reason that it has a small statistic variability around the mean [MAR20a]. Consequently, the expectation $E[n(T)]$ in Eq. (3.4) under the hypothesis of stationary random processes may be written as $E[n(T)] = 2\nu_{\mathrm{a}}T$, where ν_{a} is the expected intensity of counted cycles; in complete counts (e.g. rainflow method), $\nu_{\mathrm{a}} = \nu_{\mathrm{p}}$, where the average frequency of peaks ν_{p} uniquely depends on the random process $X(t)$ [BEN05a,BEN05b].

Using the probability distribution of stress amplitudes $f_{\mathrm{a}}(s)$ and neglecting mean value effect, the term $E[d] = E\left[s^{\mathrm{k}}\right]/2A$, which relates to the *k*-th moment, results in:

$$E[d] = \frac{1}{2A}\int_0^{\infty} s^{\mathrm{k}} f_{\mathrm{a}}(s)\,\mathrm{d}s \tag{3.5}$$

Note that the expected damage per half-cycle in Eq. (3.5) exclusively depends on stress amplitude distribution $f_{\mathrm{a}}(s)$, which is defined by a counting method.

In turns, Eq. (3.4) can be written as a function of probability distribution $f_{\mathrm{a}}(s)$:

$$E[D(T)] = \frac{\nu_\mathrm{p} T}{A} \int_0^\infty s^\mathrm{k} f_\mathrm{a}(s)\, \mathrm{d}s \tag{3.6}$$

To date no exact analytical solution for $E[D(T)]$ in Eq. (3.6) is available due to the complicate algorithm of rainflow method. However, a few methods [RYC93, BEN05a,BEN05b] address this issue by estimating the rainflow distribution and then approximating the fatigue damage (e.g. Narrow band approximation and Tovo-Benasciutti method).

3.6.1 Narrow-band approximation

In a narrow-band process, the stress amplitude distribution $f_\mathrm{a}(s)$ equals the peak distribution; if the process $X(t)$ is also Gaussian, the peak distribution is Rayleigh. The resulting expected damage per half-cycle is [BEN05a,BEN05b]:

$$E[d^\mathrm{G}]_\mathrm{NB} = \frac{1}{2A} \left(\sqrt{2\lambda_0}\right)^\mathrm{k} \Gamma\left(1 + \frac{k}{2}\right) \tag{3.7}$$

where $\Gamma(-)$ is the gamma function.

The average frequency of peaks in Eq. (3.6) equals the average frequency of upward crossings of the mean in a strictly narrow-band Gaussian process, $\nu_\mathrm{p} = \nu_0^\mathrm{G}$. Accordingly, the expected number of counted half-cycles is $E[n(T)] = 2\nu_0^\mathrm{G} T$. Using the relationship $E[D^\mathrm{G}(T)]_\mathrm{NB} = 2\nu_0^\mathrm{G} T \cdot E[d^\mathrm{G}]_\mathrm{NB}$, the expected damage in Eq. (3.6) for a narrow-band Gaussian process $X(t)$ then becomes [WIR95,LUT04,RYC93]:

$$E[D^\mathrm{G}(T)]_\mathrm{NB} = \frac{\nu_0^\mathrm{G} T}{A} \left(\sqrt{2\lambda_0}\right)^\mathrm{k} \Gamma\left(1 + \frac{k}{2}\right) \tag{3.8}$$

Eq. (3.8) is exact only for a strictly narrow-band process, which has the bandwidth parameters $\alpha_1 = 1$ and $\alpha_2 = 1$. If the process becomes more wide-banded, i.e. $\alpha_1 \to 0$

and $\alpha_2 \to 0$, rainflow amplitude distribution is no longer Rayleigh. In particular, damage $E[D^{\mathrm{G}}(T)]_{\mathrm{NB}}$ in wide-band process is a conservative estimate of the exact expected damage [BEN05a,BEN05b], i.e. it tends to overestimate the $E[D(T)]$ in Eq. (3.6). Consequently, some authors proposed approximating $E[D(T)]$ by reducing the value calculated using the "Narrow-band approximation" [BEN05a, BEN05b].

3.6.2 Tovo-Benasciutti method

Tovo and Benasciutti developed a more general theoretical method based on estimating the stress amplitude distribution of rainflow cycles [BEN05a,BEN05b]. The method assumes that rainflow cycle distribution can be linearly interpolated from two other distributions. A bandwidth correction λ_{TB} of "Narrow-band approximation" is thus derived by approximating the rainflow distribution. The expected damage per half-cycle of Tovo-Benasciutti method is [BEN05a,BEN05b]:

$$E[d^{\mathrm{G}}]_{\mathrm{TB}} = \lambda_{\mathrm{TB}} E[d^{\mathrm{G}}]_{\mathrm{NB}} = \frac{\lambda_{\mathrm{TB}}}{2A}\left(\sqrt{2\lambda_0}\right)^{\mathrm{k}}\Gamma\left(1+\frac{k}{2}\right) \tag{3.9}$$

The correction factor $\lambda_{\mathrm{TB}} = b_{\mathrm{app}} + \left(1-b_{\mathrm{app}}\right)\alpha_2^{\mathrm{k}-1}$ is a function of a weighting coefficient b_{app}, which was approximated by fitting results of time-domain simulations, including a variety of power spectral density shapes to cover a wide range of bandwidth parameters, see [BEN05a,BEN05b,BEN18b].

With this bandwidth correction λ_{TB} and invoking Eq. (3.8), the expected damage in Eq. (3.6) yields in the form:

$$E[D^{\mathrm{G}}(T)]_{\mathrm{TB}} = \frac{\lambda_{\mathrm{TB}}\nu_0^{\mathrm{G}}T}{A}\left(\sqrt{2\lambda_0}\right)^{\mathrm{k}}\Gamma\left(1+\frac{k}{2}\right) \tag{3.10}$$

Note that damage $E[D^{\mathrm{G}}(T)]_{\mathrm{TB}}$ equals to $E[D^{\mathrm{G}}(T)]_{\mathrm{NB}}$ when the process is strictly narrow-band $\alpha_1 = 1$ and $\alpha_2 = 1$. It is also possible to observe the relationship

$E[D^{\mathrm{G}}(T)]_{\mathrm{TB}} = E[D^{\mathrm{G}}(T)]_{\mathrm{NB}}$ when the inverse slope of S-N curve is unity $k = 1$. Finally, if the process is strictly wide-band $\alpha_2 = 0$, the expected damage proposed by Tovo and Benasciutti reduces to $E[D^{\mathrm{G}}(T)]_{\mathrm{TB}} = b_{\mathrm{app}} E[D^{\mathrm{G}}(T)]_{\mathrm{NB}}$, see [BEN05a,BEN05b].

Chapter 4

VARIANCE OF FATIGUE DAMAGE IN GAUSSIAN RANDOM LOADING

4.1 INTRODUCTION

Chapter 2 presented some fundamental concepts associated with the random process in time-domain. Statistical properties of the process were also introduced via a frequency-domain approach. They are commonly used for describing uniaxial and multiaxial random stress.

Chapter 3 provided a short review on material properties, the rainflow counting method, the amplitude histogram and the loading spectrum, the linear damage accumulation rule, and the expected fatigue damage. Such procedures may take two different methods to estimate fatigue damage. In a frequency-domain approach, the expected damage is the result of averaging all the damages of an infinite ensemble of time-histories. In contrast, the time-domain approach calculates the damage by directly handling one or more time-histories. It is typically based on the rainflow counting method and the Palmgren-Miner rule.

The hypothesis adopted in practice is that theoretical methods (e.g. time-domain approach) typically work on very few or even one time-history record collected through measurements. In any case, the damage computed from one random time-history $x_1(t)$

of finite length T must be considered as being one sample value out of an infinite population. This value has an inherent statistical scatter. In fact, the damage is likely to change if it is computed based on a different time-history $x_2(t)$, even if this record has precisely the same time length and statistical properties of $x_1(t)$. The two time-histories may have different rainflow cycles. The same thing happens if the damage is computed using a third time-history $x_3(t)$ [BEN18b]. This result is explained by the random nature of each time-history. Viewed from the theory of random processes (see Chapter 2), each time-history $x_{\mathrm{i}}(t)$ is conceived of as being one element out of an infinite ensemble; its fatigue damage is one value out of an infinite set of damage values.

Indeed, damage $D(T)$ of $x_{\mathrm{i}}(t)$ of finite length T is a random variable according to a certain damage probability distribution. The variance around the expected damage is an important characteristic of the damage probability distribution. Estimating the variance of damage becomes as important as estimating the expected damage in the structural durability assessment of structures [MAR19b,MAR19a]. Some authors (e.g. Mark and Crandall, Bendat, Madsen et al., Low) have proposed empirical expressions to evaluate the variance of fatigue damage for stationary random loading [MAR61,BEN64,MAD86,LOW12]. However, all methods are required to determine the autocorrelation coefficient function $\rho_{\mathrm{d_o,d_l}}(l)$ of damage. This chapter will show that this quantity follows from the autocorrelation function of the process, $R_{\mathrm{X}}(\tau)$, or equivalently from the PSD. This computation would not be necessary if a mathematical expression to relate the variance of fatigue damage directly to some PSD bandwidth parameters was available.

This chapter introduces relevant equations of variance of fatigue damage, which have general validity in narrow-band processes. Such equations will be further specified by four methods from the literature about narrow-band Gaussian random loading, i.e. Mark and Crandall, Bendat, Madsen et al. and Low. This chapter also presents a critical review of such methods and later compares them with Monte Carlo simulations in the time- and frequency-domain approaches. Simulations considered a linear oscillator

system, an ideal unimodal random process, and the JONSWAP and Pierson-Moskowitz power spectral densities. Based on all simulation results, best-fitting expressions were derived to relate the coefficient of variation of damage to the bandwidth parameter α_1. In accordance with the best-fitting coefficients, the proposed expressions apply to a wide range of PSDs, from narrow-band to wide-band processes.

The variance of fatigue damage in non-Gaussian random processes will be addressed in Chapter 5.

4.2 GENERAL EQUATIONS IN NARROW-BAND PROCESS

This section provides a general equation in a narrow-band process for the variance of fatigue damage. They will be discussed in greater detail by the four different methods from literature.

The variance is derived by taking the variance of damage $D(T)$ [MAR61]:

$$\sigma_{\mathrm{D}}^2 = \mathrm{Var}\left[\sum_{\mathrm{i}=0}^{\mathrm{n(T)}-1} d_{\mathrm{i}}\right] = E\left[\sum_{\mathrm{i}=0}^{\mathrm{n(T)}-1}\sum_{\mathrm{j}=0}^{\mathrm{n(T)}-1} d_{\mathrm{i}} d_{\mathrm{j}}\right] - \left(E\left[\sum_{\mathrm{i}=0}^{\mathrm{n(T)}-1} d_{\mathrm{i}}\right]\right)^2 \tag{4.1}$$

The second equality arises from the definition of the variance of a random variable $\mathrm{Var}[D(T)] = E[D^2(T)] - (E[D(T)])^2$. As for the damage, the variance considers two sources of randomness, which are the stress amplitudes and the number of half-cycles. The number of counted cycles $n(T)$ can be assumed to be a deterministic value due to a small scatter around its mean value. In a narrow-band process, the number of cycles is equal to $n(T) = 2\nu_0 T$. The variance in Eq. (4.1) is then a direct function of $n(T)$ and an indirect function of T.

Since $n(T)$ is deterministic, both expectations in Eq. (4.1) can move inside the double and single summation, respectively. Omitting time T, the variance expression turns into:

$$\sigma_{\mathrm{D}}^2 = \sum_{\mathrm{i}=0}^{\mathrm{n}-1}\sum_{\mathrm{j}=0}^{\mathrm{n}-1} E\left[d_{\mathrm{i}}d_{\mathrm{j}}\right] - \left(\sum_{\mathrm{i}=0}^{\mathrm{n}-1} E[d_{\mathrm{i}}]\right)^2 \tag{4.2}$$

The double summation in Eq. (4.2) can be clarified by a $n \times n$ matrix, as exemplified in Figure 1.1.

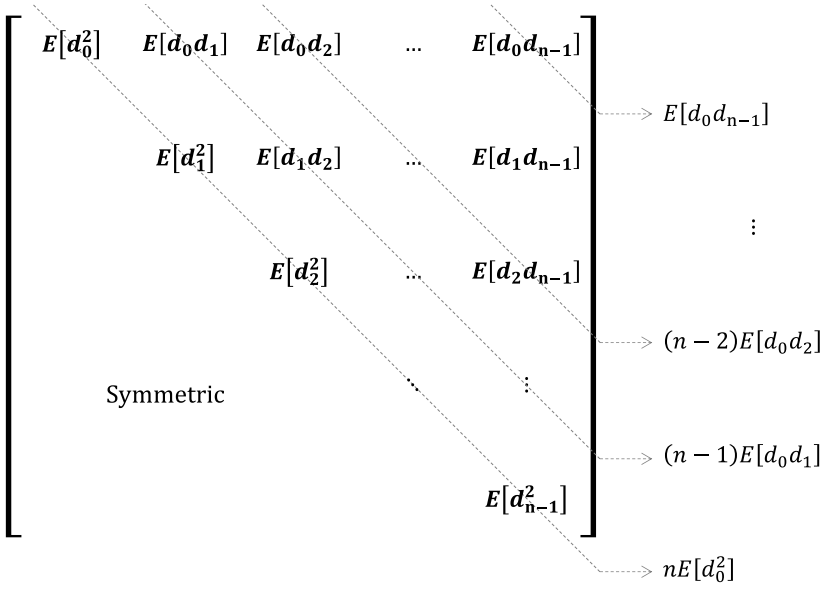

Figure 4.1. The double summation in Eq. (4.2) as an $n \times n$ matrix and the sum of elements in any diagonal.

Since the process is stationary, the half-cycle damage process d_{i} is stationary, too. This suggests that the sum of all elements in the main diagonal (see Figure 1.1) yields the term $nE[d_0^2]$ and the sum of off-diagonal terms corresponds to $(n-l)E[d_0d_{\mathrm{l}}]$, where $l = j - i$ takes on integer values from 1 to $n-1$. On this end, the double summation may reduce to a single summation because the elements in any diagonal are the same.

On the hypothesis of stationary half-cycle damage, the expectation $E[d_\mathrm{i}]$ in Eq. (4.2) implies that $E[d_0] = E[d_1] = \cdots = E[d_{\mathrm{n}-1}]$, from where the single summation squared outcomes into $n^2 E[d_0]^2$. The variance of fatigue damage in Eq. (4.2) can thus be rewritten as [LOW12]:

$$\sigma_\mathrm{D}^2 = n(E[d_0^2] - E[d_0]^2) + 2\sum_{\mathrm{l}=1}^{\mathrm{n}-1}(n-l)(E[d_0 d_\mathrm{l}] - E[d_0]^2) \tag{4.3}$$

The expected cross-product describes the autocorrelation function of the half-cycle damage, $R_{\mathrm{d_o,d_l}}(l) = E[d_0 d_\mathrm{l}]$. The term $E[d_0^2]$ is the value at zero-time lag, $E[d_0^2] = R_{\mathrm{d_o,d_l}}(0)$. The difference between $R_{\mathrm{d_o,d_l}}(0)$ and the mean squared $E[d_0]^2 = \mu_\mathrm{d}^2$ provides the variance of the half-cycle damage, $R_{\mathrm{d_o,d_l}}(0) - \mu_\mathrm{d}^2 = \sigma_\mathrm{d}^2$.

In similarity with the random process $X(t)$, the autocorrelation coefficient of half-cycle damage is introduced:

$$\rho_{\mathrm{d_o,d_l}}(l) = \frac{R_{\mathrm{d_o,d_l}}(l) - \mu_\mathrm{d}^2}{\sigma_\mathrm{d}^2} \tag{4.4}$$

which is bounded as $0 \leq \rho_{\mathrm{d_o,d_l}}(l) \leq 1$. This range results from the fact that the damage is always positive [BEN64]. The parameter $\rho_{\mathrm{d_o,d_l}}(l)$ measures the correlation between the random variables d_0 and d_l drawn from the same random process.

Under the hypothesis of deterministic number of half-cycles, Eq. (4.3) represents the expression of the variance of the damage for a stationary narrow-band random process. It is possible to demonstrate that Eq. (4.3) can also be written as a function of $\rho_{\mathrm{d_0,d_l}}(l)$ [LOW12]:

$$\sigma_{\mathrm{D}}^2 = \left[n + 2 \sum_{\mathrm{l}=1}^{\mathrm{n}-1} (n-l) \rho_{\mathrm{d_0,d_l}}(l) \right] (E[d_0^2] - E[d_0]^2) \tag{4.5}$$

Eq. (4.5) makes clear the fundamental role of the autocorrelation coefficient function $\rho_{\mathrm{d_0,d_l}}(l)$ in the calculation of the variance of the damage. The four methods reviewed in the next section differ based on which expression is assumed for the autocorrelation coefficient function of the process. In turn, the amount $\rho_{\mathrm{d_0,d_l}}(l)$ depends on the damage autocorrelation function $R_{\mathrm{d_0,d_l}}(l) = E[d_0 d_{\mathrm{l}}]$ by Eq. (4.4).

From now on, two peaks, P_0 and P_{l}, are separated by a time difference $\tau = l/(2\nu_0)$. Like in [LOW12], all over the text ‘‘peak’’ is used in a broad sense to also mean valley. Noted that the stress amplitude is equal to the peak value, $s_{\mathrm{l}} = P_{\mathrm{l}}$ in a narrow-band process. Therefore, the damage per half-cycle d_{l} is proportional to $P_{\mathrm{l}}^{\mathrm{k}}$. Consequently, the product $E[d_0 d_{\mathrm{l}}]$ can be computed from the joint probability density function (JPDF) of two peaks, $f_{\mathrm{P_0,P_l}}(x_{\mathrm{p}}, x_{\mathrm{v}})$ as:

$$E[d_0 d_{\mathrm{l}}] = \frac{1}{4A^2} \iint_{-\infty}^{\infty} x_{\mathrm{p}}^{\mathrm{k}} x_{\mathrm{v}}^{\mathrm{k}} \, f_{\mathrm{P_0,P_l}}(x_{\mathrm{p}}, x_{\mathrm{v}}) \, \mathrm{d}x_{\mathrm{p}} \, \mathrm{d}x_{\mathrm{v}} \tag{4.6}$$

This equation shows that $E[d_0 d_{\mathrm{l}}]$ is a function of the JPDF $f_{\mathrm{P_0,P_l}}(x_{\mathrm{p}}, x_{\mathrm{v}})$, which thus performs a significant role in the calculation of the variance of the damage. For example, the Low’s method takes into account the Rice’s formula valid for a narrow-band process [LOW12].

4.3 ANALYTICAL SOLUTIONS

In this section, a summary of various analytical methods for the variance of fatigue damage is provided. The four methods reviewed in this section will be further discussed by the critical analysis of them.

4.3.1 Mark and Crandall's method (1961)

Mark and Crandall developed the first explicit formula to compute the variance of the fatigue damage [MAR61]. Their method assumes that stress time-histories are related to the response of a light damped linear oscillator system. This case is a narrow-band Gaussian process that allowed Mark and Crandall to approximate the expression for the variance as:

$$(\sigma_{\mathrm{D}}^2)_{\mathrm{Mar}}^{\mathrm{G}} = \frac{f(k)\nu_0^{\mathrm{G}}T}{\zeta A^2}(2\lambda_0)^{\mathrm{k}}\,\Gamma^2\left(1+\frac{k}{2}\right), \quad \text{for } \zeta \le 0.05 \text{ and } \zeta\nu_0^{\mathrm{G}}T \gg 1 \tag{4.7}$$

where $f(k)$ is a function of odd k and ζ is the damping coefficient of linear oscillator system. The whole mathematical expansion leading to $f(k)$ is too long to be replicated here. The function $f(k)$ has been pre-computed up to $k = 15$; some values are $f(1) = 0.041$, $f(3) = 0.369$, $f(5) = 1.28$, $f(7) = 3.72$ [MAR61,CRA62]. Note that the function $f(k)$ is nonlinear with k. On the other hand, the variance in Eq. (4.7) increases linearly with $\nu_0^{\mathrm{G}}T$ arising the same trend as the expected damage for a narrow-band Gaussian process $E[D^{\mathrm{G}}(T)]_{\mathrm{NB}}$ (see Chapter 3). The variance of damage also increases with k or if the damping coefficient ζ turns smaller.

The coefficient of variation (CoV) of the damage $C_{\mathrm{D}} = \sigma_{\mathrm{D}}/E[D(T)]$, equal to the ratio of the standard deviation σ_{D} to the expected value $E[D(T)]$. After substituting the expected damage $E[D^{\mathrm{G}}(T)]_{\mathrm{NB}}$ and Eq. (4.7) one obtains the expression for the Mark and Crandall's method:

$$(C_{\mathrm{D}})^{\mathrm{G}}_{\mathrm{Mar}} = \sqrt{\frac{f(k)}{\zeta \nu_0^{\mathrm{G}} T}}, \qquad \text{for } \zeta \leq 0.05 \text{ and } \zeta \nu_0^{\mathrm{G}} T \gg 1 \tag{4.8}$$

Note that the CoV increases only in proportion to $\sqrt{\nu_0^{\mathrm{G}} T}$ in the range where Eq. (4.8) is valid [MAR61] while the expected damage $E[D^{\mathrm{G}}(T)]_{\mathrm{NB}}$ and variance of damage increase linearly with $\nu_0^{\mathrm{G}} T$.

4.3.2 Bendat's method (1964)

Based on the assumption that the variance of fatigue damage applies the linear oscillator system, Bendat established a more general expression [BEN64]. His method assumes that the autocorrelation coefficient of the half-cycle damage decays exponentially as $\rho^{\mathrm{G}}_{\mathrm{d_0,d_1}}(l) = \exp(-2\pi\zeta l)$ as an alternative to solving the product $E\left[d_0^{\mathrm{G}} d_1^{\mathrm{G}}\right]$ for narrow-band Gaussian process. With such simplification, by substituting the expected damage per half-cycle $E[d^{\mathrm{G}}(T)]_{\mathrm{NB}}$ into Eq. (4.5), the variance of damage turns into:

$$(\sigma_{\mathrm{D}}^2)^{\mathrm{G}}_{\mathrm{Ben}} = \frac{\nu_0^{\mathrm{G}} T}{\zeta A^2} (2\lambda_0)^{\mathrm{k}} \left[\Gamma(1+k) - \Gamma^2\left(1 + \frac{k}{2}\right)\right] \tag{4.9}$$

Eq. (4.9) no longer depends on $f(k)$ compared to Mark and Crandall's one Eq. (4.7).

The closed-form expression of the CoV results into:

$$(C_{\mathrm{D}})^{\mathrm{G}}_{\mathrm{Ben}} = \sqrt{\frac{1}{\zeta \nu_0^{\mathrm{G}} T}\left[\frac{\Gamma(1+k)}{\Gamma^2\left(1+\frac{k}{2}\right)} - 1\right]} \tag{4.10}$$

Equations (4.9) and (4.10) hold for both even and odd integer values of k. Likewise, the Crandal and Mark's solution, also the Bendat's equation of the variance is relative to the $\nu_0^{\mathrm{G}} T$, whereas that of the CoV is inversely proportional to $\sqrt{\zeta \nu_0^{\mathrm{G}} T}$.

4.3.3 Madsen et al.'s method (1986)

Madsen et al. suggested a method for any value of k and any narrow-band Gaussian process [MAD86]. This method calculates the parameter $\rho^{\mathrm{G}}_{\mathrm{d_0,d_1}}(l)$ in the form of expectation of even powers of correlated normal variables by the envelope process, whose result for $k = 2$ is known from [PAR62,KRE83,MAD86]:

$$\rho^{\mathrm{G}}_{\mathrm{d_0,d_1}}(l) = \frac{1}{2}\left[\rho^2_{\mathrm{X}}(l) + 2\left(\frac{\rho'_{\mathrm{X}}(l)}{2\pi\nu_0^{\mathrm{G}}}\right)^2 + \frac{\left(\rho''_{\mathrm{X}}(l)\right)^2}{\left(2\pi\nu_0^{\mathrm{G}}\right)^4}\right] \tag{4.11}$$

in which $\rho_{\mathrm{X}}(l)$ is the autocorrelation coefficient calculated at lag l, while $\rho'_{\mathrm{X}}(l)$ and $\rho''_{\mathrm{X}}(l)$ are the first and second derivative of $\rho_{\mathrm{X}}(l)$ with respect to l. After the assumption that $\rho''_{\mathrm{X}}(l) \cong -\left(2\pi\nu_0^{\mathrm{G}}\right)^2 \rho_{\mathrm{X}}(l)$, Madsen et al. arrived at [MAD86]:

$$\rho^{\mathrm{G}}_{\mathrm{d_0,d_1}}(l) \cong \rho^2_{\mathrm{X}}(l) + \left(\frac{\rho'_{\mathrm{X}}(l)}{2\pi\nu_0^{\mathrm{G}}}\right)^2 \tag{4.12}$$

By introducing the expected damage per half-cycle $E[d^{\mathrm{G}}(T)]_{\mathrm{NB}}$ and Eq. (4.12) into Eq. (4.5), the variance is computed as:

$$(\sigma_{\mathrm{D}}^2)_{\mathrm{Mad}}^{\mathrm{G}} =$$

$$\left\{n + 2\sum_{\mathrm{l}=1}^{\mathrm{n}-1}(n-l)\left[\rho_{\mathrm{X}}^2(l) + \left(\frac{\rho_{\mathrm{X}}'(l)}{2\pi\nu_0^{\mathrm{G}}}\right)^2\right]\right\}\frac{(2\lambda_0)^k}{4A^2}\left[\Gamma(1+k) - \Gamma^2\left(1+\frac{k}{2}\right)\right] \tag{4.13}$$

Eq. (4.13) implies a summation of terms linked to the autocorrelation coefficient $\rho_{\mathrm{X}}(l)$. Note how the variance of damage derived by Madsen et al. does not need to compute the product $E\left[d_0^{\mathrm{G}} d_{\mathrm{l}}^{\mathrm{G}}\right]$. The proper CoV of damage is:

$$(C_{\mathrm{D}})_{\mathrm{Mad}}^{\mathrm{G}} =$$

$$\frac{1}{n}\sqrt{\left\{n + 2\sum_{l=1}^{n-1}(n-l)\left[\rho_{\mathrm{X}}^2(l) + \left(\frac{\rho_{\mathrm{X}}'(l)}{2\pi\nu_0^{\mathrm{G}}}\right)^2\right]\right\}\left[\frac{\Gamma(1+k)}{\Gamma^2\left(1+\frac{k}{2}\right)} - 1\right]} \tag{4.14}$$

Eq. (4.14) is also a function of the autocorrelation coefficient $\rho_{\mathrm{X}}(l)$. Being valid for any narrow-band Gaussian process (other than a linear oscillator system), the Madsen et al.'s expressions are not a function of the damping coefficient ζ.

Furthermore, for the case of $k \neq 2$, the autocorrelation coefficient of half-cycle damage $\rho_{\mathrm{d_0,d_l}}^{\mathrm{G}}(l)$ may be approximated as:

$$\rho_{\mathrm{d_0,d_l}}^{\mathrm{G}}(l) \cong \frac{\Gamma^2\left(1+\frac{k}{2}\right)\left[{}_2F_1\left(-\frac{k}{2},-\frac{k}{2};1;\rho_{\mathrm{X}}^2(l) + \left(\frac{\rho_{\mathrm{X}}'(l)}{2\pi\nu_0^{\mathrm{G}}}\right)^2\right) - 1\right]}{\left[\Gamma(1+k) - \Gamma^2\left(1+\frac{k}{2}\right)\right]} \tag{4.15}$$

where ${}_2F_1(-)$ is the hypergeometric function. From this expression the variance and CoV of damage can then be computed for $k \neq 2$ [MAD86].

4.3.4 Low's method (2012)

Low proposed a method for any narrow-band Gaussian process by a best-fitting expression of $\rho^{\mathrm{G}}_{\mathrm{d_0,d_l}}(l)$. His method calculates the product expectation $E\left[d_0^{\mathrm{G}} d_{\mathrm{l}}^{\mathrm{G}}\right]$ using the Rice JDPF of peaks and valleys [LOW12]:

$$f^{\mathrm{G}}_{\mathrm{P_0,P_l}}(x_{\mathrm{p}}, x_{\mathrm{v}}) = \frac{x_{\mathrm{p}} x_{\mathrm{v}}}{1-\rho_{\mathrm{X}}^2(l)} I_0\left(\frac{x_{\mathrm{p}} x_{\mathrm{v}}\, \rho_{\mathrm{X}}(l)}{1-\rho_{\mathrm{X}}^2(l)}\right) \exp\left(-\frac{x_{\mathrm{p}}^2 + x_{\mathrm{v}}^2}{2\left(1-\rho_{\mathrm{X}}^2(l)\right)}\right) \tag{4.16}$$

where $I_0(-)$ is the modified Bessel function of the first kind with order zero. Replacing the $f^{\mathrm{G}}_{\mathrm{P_0,P_l}}(x_{\mathrm{p}}, x_{\mathrm{v}})$ into Eq. (4.6), the double integral has been solved for even values $k = 2, 4, 6$ with the aid of symbolic computation software [LOW12]. Subsequently, in order to add the odd value of k, the autocorrelation coefficient function $\rho^{\mathrm{G}}_{\mathrm{d_0,d_l}}$ has been quite accurately approximated by a quadratic interpolation function of $\rho_{\mathrm{X}}^2(l)$ as [LOW12]:

$$f^{\mathrm{G}}_{\mathrm{P_0,P_l}}(x_{\mathrm{p}}, x_{\mathrm{v}}) = \alpha_{\mathrm{k}} \rho_{\mathrm{X}}^2(l) + \beta_{\mathrm{k}} \rho_{\mathrm{X}}^4(l) \tag{4.17}$$

where the fitting coefficients α_k and β_k are functions of k (their values are tabulated in [LOW12]). These coefficients included the integer values within the range $1 \le k \le 9$. A linear interpolation is recommended to hold non-integer k values [LOW12].

With this estimate and the expected damage per half-cycle $E[d^{\mathrm{G}}(T)]_{\mathrm{NB}}$ (see Chapter 3), the variance of the fatigue damage in Eq. (4.5) results in the form:

$$(\sigma_{\mathrm{D}}^2)^{\mathrm{G}}_{\mathrm{Low}} = \left\{ n + 2\sum_{\mathrm{l}=1}^{\mathrm{n}-1} (n-l)\left(\alpha_{\mathrm{k}} \rho_{\mathrm{X}}^2(l) + \beta_{\mathrm{k}} \rho_{\mathrm{X}}^4(l)\right)\right\} \frac{(2\lambda_0)^{\mathrm{k}}}{4A^2}\left[\Gamma(1+k) - \Gamma^2\left(1+\frac{k}{2}\right)\right] \tag{4.18}$$

Hence the CoV can be written as:

$$(C_{\mathrm{D}})^{\mathrm{G}}_{\mathrm{Low}} = \frac{1}{n}\sqrt{\left\{n + 2\sum_{l=1}^{\mathrm{n}-1}(n-l)\left(\alpha_{\mathrm{k}}\rho_{\mathrm{X}}^{2}(l) + \beta_{\mathrm{k}}\rho_{\mathrm{X}}^{4}(l)\right)\right\}\left[\frac{\Gamma(1+k)}{\Gamma^{2}\left(1+\frac{k}{2}\right)} - 1\right]} \tag{4.19}$$

Note similarity between the expression of the CoV by Madsen et al. Eq. (4.14) and Low (4.19).

4.3.5 Critical analysis of analytical methods

The primary difference among the preceding methods is the process considered (linear oscillator or any narrow-band Gaussian process) and how the quantity $\rho^{\mathrm{G}}_{\mathrm{d_0},\mathrm{d_l}}(l)$ is calculated. In this context, another hypothesis is the values allowed for the S-N inverse slope (i.e. even and/or odd integers, or also non-integers).

Mark and Crandall's pioneering work has the highly restrictive hypotheses (light damped oscillator and odd k), which make its application not much general. Bendat's method has the same assumptions of Mark and Crandall's approach, the key difference being that it allows for both odd and even values of k and that it does not impose restrictions to the damping ζ. The hypothesis of an autocorrelation $\rho^{\mathrm{G}}_{\mathrm{d_0},\mathrm{d_l}}(l)$ decaying exponentially seems to be empirical.

In contrast, the method of Madsen et al. and that of Low are far more general. By autocorrelation coefficient $\rho_{\mathrm{X}}(l)$, both methods apply to any narrow-band Gaussian process. The only difference is how this coefficient enters into the expressions of the variance and CoV, compare Eq. (4.13)-(4.14) to Eq. (4.18)-(4.19). Basically, this difference is clear from the relationship between the autocorrelation coefficient function

of the process, $\rho_X(l)$, and that of the damage, $\rho^G_{d_0,d_1}(l)$, which is derived by each of the two methods via Eq. (4.12) or .(4.17).

Among the two, Madsen et al.'s method nevertheless appears to be the most general since it has no restriction on the k values. Because of this, it will be used as a reference in the simulation study of next section.

One possible limitation of Madsen et al.'s and Low's method is that they ask for the autocorrelation coefficient function of the process $\rho_X(l)$ in order to compute the CoV in Eq. (4.14) and (4.19), where $\rho_X(l)$ depends on $R_X(\tau)$. Also, $R_X(\tau)$ can be found directly from the PSD after a Fourier transform computation if it is not available. It would be much simpler to avoid this Fourier transformation by linking the CoV directly to the PSD bandwidth parameters (e.g. α_1 and α_2). This argument will be discussed in Section 4.5.

Finally, it seems important to point out that all the four reviewed methods are restricted to random loadings that are Gaussian and narrow-band. A solution valid for random loadings with multiple frequency modes including two or more narrowband components was proposed by Low [LOW14a]. The multimodal Low's method works in connection with Low's method for estimating the fatigue damage [LOW10]. The Low [LOW10] approach is, however, intricate and difficult to implement. In fact, Low proposed a surrogate model [LOW14b] that approximates the exact expected fatigue damage from bimodal process. The Low's surrogate model does not provide explicitly the low- and high-frequency damages, which thus makes impossible to apply the multimodal Low's method. A simple and accurate model for both low- and high-frequency damages is required to apply the multimodal Low's method without too much effort. Consequently, the multimodal method by Low is not considered here; for details see [LOW14a].

4.4 NUMERICAL SIMULATIONS

Monte Carlo simulations in time- and frequency-domain are used in this section to investigate the accuracy of the explicit formulas provided by the four previous methods. Two types of power spectrum $S_{\mathrm{X}}(f)$ are considered: linear oscillator response, ideal unimodal (rectangular shape). Both are centered at 10 Hz and normalized to $\lambda_0 = 1$, see Figure 4.2(a) and (b). Other two power spectra (Pierson-Moskowitz and JONSWAP) are analyzed in Section 4.4.3 when it comes to find a best-fitting expression to link the CoV to bandwidth parameters.

For every spectrum $S_{\mathrm{X}}(f)$, a total of $N = 2 \cdot 10^5$ stationary Gaussian random time-histories $x_{\mathrm{i}}(t)$, $i = 1,2,3, \dots N$ with time length T are simulated. Note that the total number of simulated time-histories is comparable or larger than that used in other similar studies [LOW12,LOW14a,BEN09a]. The digitalized time-histories are created by the Discrete Fourier Transform approach, which uses deterministic spectral amplitudes and uniformly distributed random phases [SMA93,WIR95]. Three distinct values of T are selected so that the simulated time-histories have about 10^3, 10^4 and 10^5 counted cycles.

An estimated power spectral density $\hat{S}_{\mathrm{X,i}}(f)$ is also obtained from each simulated time-history $x_{\mathrm{i}}(t)$ by means of the Welch's windowed overlapped block (or segment) averaging technique [BEN10c,WIR95]. A Hanning window was chosen to mitigate the side-lobe leakage; a 75% overlapping allowed a total of 97 blocks for which the statistical error of the spectrum estimate is $\varepsilon_{\mathrm{r}} = 1/\sqrt{97} = 0.10$. For each of the three selected values of T, the analysis provides $N = 2 \cdot 10^5$ estimated power spectra $\hat{S}_{\mathrm{X,i}}(f)$, one for each simulated time-history.

Time- and frequency-domain approach are employed to compute the fatigue damage $D_{\mathrm{i}}(T)$ for every time-history $x_{\mathrm{i}}(t)$. By rainflow counting algorithm and Palmgren-Miner rule, the time-domain damage is calculated from $x_{\mathrm{i}}(t)$. In contrast, the frequency-domain damage is calculated by the expected damage $E[D^{\mathrm{G}}(T)]_{\mathrm{NB}}$ from the

estimated power spectrum $\hat{S}_{\mathrm{X,i}}(f)$. In this view, the frequency-domain damage should be interpreted as a sample estimate of the expected damage $E[D^{\mathrm{G}}(T)]_{\mathrm{NB}}$.

Each estimated power spectrum $\hat{S}_{\mathrm{X,i}}(f)$ is evaluated from one single time-history of finite duration, which has an inherent sampling variability [BEN10c,WIR95]. This sampling variability makes every estimation $\hat{S}_{\mathrm{X,i}}(f)$ not the same as the "true" power spectral density $S_{\mathrm{X}}(f)$ – indeed, the spectral values $\hat{S}_{\mathrm{X,i}}(f)$ are random variables following a chi-square probability distribution [BEN10c,WIR95]. The sampling variability in power spectrum estimate transfers to the frequency-domain damage and it sums to the variability resulting from the randomness of time-history realizations, which instead is the only source of variability included in the time-domain damage.

Integer k values from 2 to 9 and S-N curve with $A = 1$ are assumed to calculate the damage $D_{\mathrm{i}}(T)$ values. The sample mean damage $\overline{D}(T) = N^{-1}\sum_{\mathrm{i}=1}^{\mathrm{N}} D_{\mathrm{i}}(T)$, sample variance $\hat{\sigma}_{\mathrm{D}}^2 = (N-1)^{-1}\sum_{\mathrm{i}=1}^{\mathrm{N}}[D_{\mathrm{i}}(T) - \overline{D}(T)]^2$ and sample CoV $\hat{C}_{\mathrm{D}} = \hat{\sigma}_{\mathrm{D}}/\overline{D}(T)$ are estimated from the set of damage values in time- and frequency-domain. Instead, the expected damage $E[D^{\mathrm{G}}(T)]_{\mathrm{NB}}$ is calculated directly from the power spectrum $S_{\mathrm{X}}(f)$.

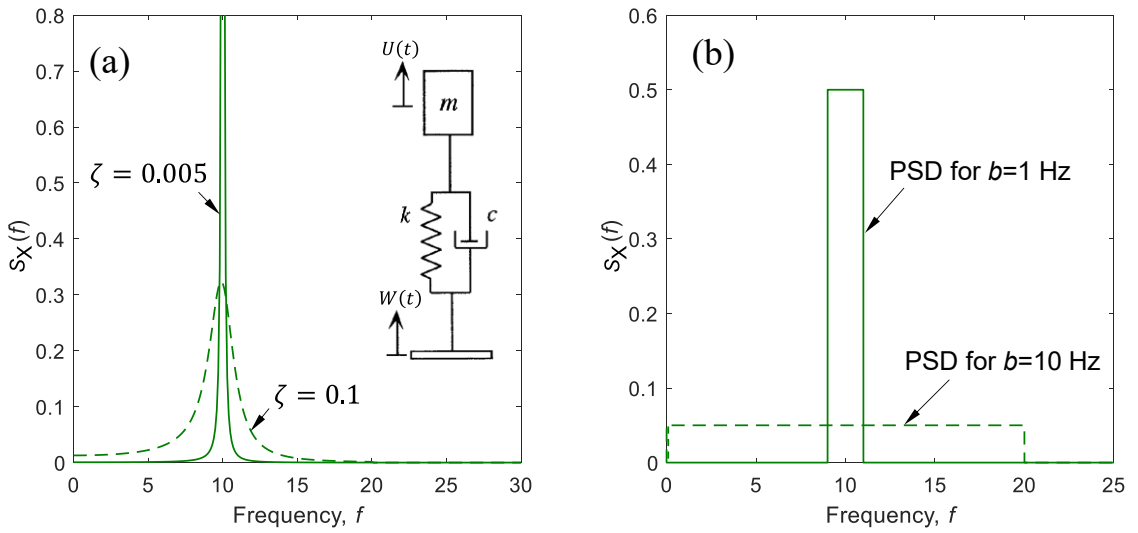

Figure 4.2. PSDs considered in numerical simulations: (a) linear oscillator system (for two limit values of damping), (b) ideal unimodal process (the dashed and the continuous line show the PSD with the narrowest and the widest half-spectral bandwidth).

4.4.1 Linear oscillator system

The linear oscillator system is here chosen because the explicit formulas can be applied through all the previous methods. The same system with different light damping $\zeta = 0.005, 0.01, 0.02, 0.05, 0.1$ was subject to a band-limited random base acceleration $W(t)$ with frequency content from 0 to 20 Hz. Analytical expressions are derived for the mass absolute displacement, $U(t)$, and the relative displacement, $X(t) = U(t) - W(t)$. The relative displacement response spectrum $S_X(f)$ is centered around the natural frequency (see Figure 4.2(a)) and it is a narrow-band Gaussian process $X(t)$, with bandwidth parameters ranging from $\alpha_1 = 0.998$, $\alpha_2 = 0.994$ (for $\zeta = 0.005$) to $\alpha_1 = 0.961$, $\alpha_2 = 0.895$ (for $\zeta = 0.1$).

Figure 4.3 illustrates the trend of the sample mean and the sample standard deviation of the fatigue damage (both normalized to the expected damage) for both time- and frequency-domain results, as a function of the number of counted cycles. The figure refers to the inverse slope $k = 3$ and damping $\zeta = 0.005$, but similar trends are obtained for other values (a higher damping only decreases the variance values). The box on the left side compares the observed probability distributions corresponding to the three different number of cycles examined. The distributions demonstrate that the standard deviation increases as the number of cycles diminishes. The highest (normalized) standard deviation (i.e. the CoV) is due to the unfavorable combination of a low number of cycles and a low damping ζ, as predicted by Eq. (4.8). The variability of the damage is quite large in time-histories of short length (that is, those with a small number of counted cycles). Figure 4.3 also shows that the greater is the number of counted cycles, the lower is the dispersion around the mean of the damage distribution. For any number of counted cycles, the standard deviation in the frequency-domain seems to be slightly lower (about 1%) than that in the time-domain. In addition, the mean damage in the frequency-domain seems closer to the expected damage. This result seems to confirm that the PSD estimation does not introduce a significant error in the frequency-domain damage.

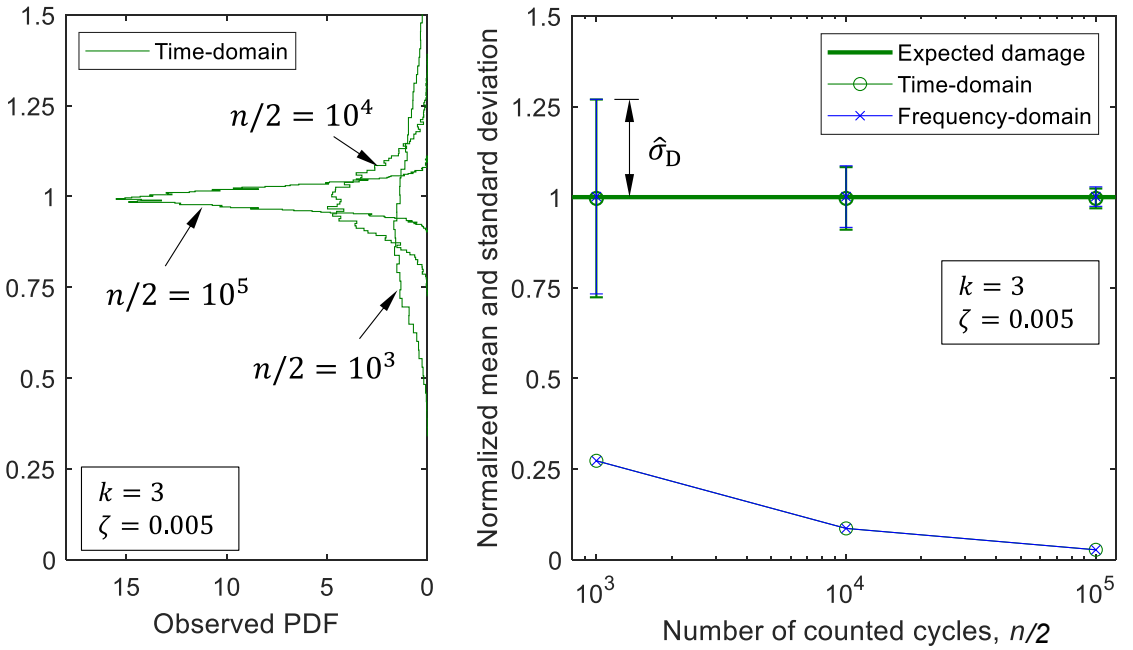

Figure 4.3. Simulation results for the linear oscillator system. Sample mean and sample standard deviation of the damage (both normalized to the expected damage) as function of the number of counted cycles (damping $\zeta = 0.005$, inverse slope $k = 3$). The left box displays the observed probability distributions.

Figure 4.4 clarifies not only the CoV by varying the number of counted cycles but also the trend in Figure 4.3. Comparison between the CoV from simulations and all analytical methods shows a good agreement over all number of counted cycles. The straight lines on a log-log scale have in some way to be expected, as the CoV from any analytical method is inversely related to the square root of the number of counted cycles, $\sqrt{\nu_0^{\mathrm{G}} T}$ [MAR61].

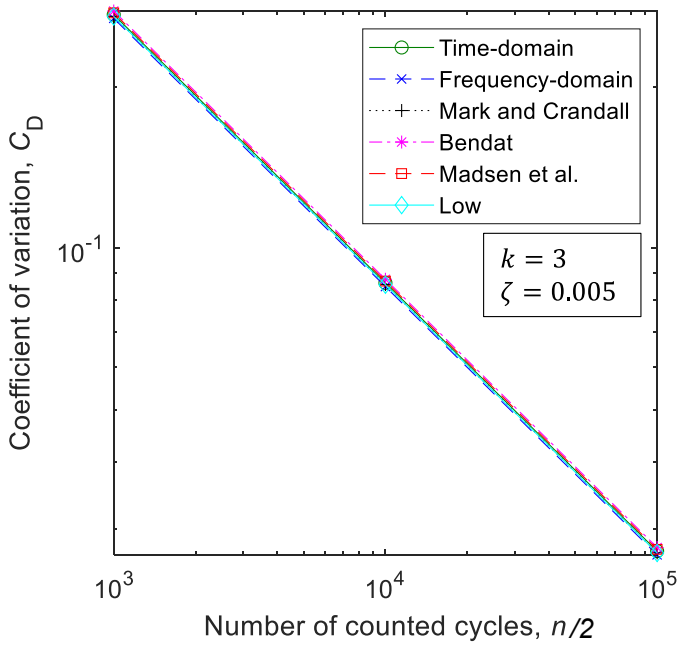

Figure 4.4. Simulation results for the linear oscillator system. CoV of the damage as function of the number of counted cycles (damping $\zeta = 0.005$, inverse slope $k = 3$).

4.4.2 Ideal unimodal process

Ideal unimodal process refers to a rectangular spectrum, see Figure 4.2(b). The effect of the bandwidth (from narrow-band to wide-band Gaussian process) is incorporated in the half spectral width b, which takes on integer values in the interval from 1 to 10 Hz. Figure 4.2(b) presents the PSD for these two limit values of b. The bandwidth parameters decrease from $\alpha_1 = 0.998$ and $\alpha_2 = 0.993$ (most narrow-band case) to $\alpha_1 = 0.866$ and $\alpha_2 = 0.745$ (lowest values for the most wide-band case) by increasing b. Using this range of bandwidth parameters, the CoV from Monte Carlo simulations in the time-domain is compared with the Madsen et al.'s method. Contrary to the example with the linear oscillator, not all the methods can be applied to the unimodal PSD. In fact, the ideal unimodal PSD – even if narrow-band – is not include in the range of applicability of both Mark and Crandall's and Bendat's methods, while the other two methods of Madsen et al. and Low applies to the ideal unimodal. Instead, these methods provide almost coincident results, as shown for example in Figure 4.3, although as already emphasized the Madsen

et al.'s method gives the most general expressions for variance and CoV. For this reason, only the Madsen et al.'s method will be included in the figures.

Figure 4.5 displays the autocorrelation coefficient function of the process, $\rho_X(\tau)$, and of the half-cycles damage, $\rho^G_{d_0,d_1}$, and compares them for the two limit spectral bandwidths corresponding to the most narrow-band and most wide-band process. The figure allows one to understand immediately the different behavior of $\rho^G_{d_0,d_1}$: its amplitude decays faster in a wide-band process than in a narrow-band one. In the former case, the process is less "correlated" and thus even adjacent half-cycles do not have similar values of their amplitude and, in turn, of their damage – on average, the product $E\left[d_0^G d_1^G\right]$ in the definition of $\rho^G_{d_0,d_1}$ is close to zero even for small l.

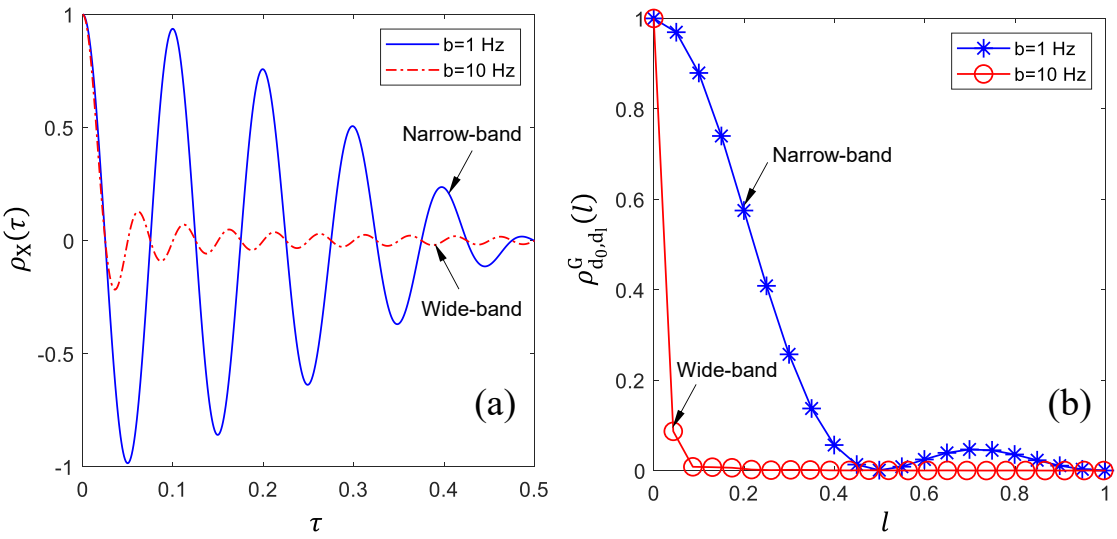

Figure 4.5. Comparison between the most narrow-band and most wide-band ideal unimodal process. Autocorrelation coefficient function of (a) the process and (b) the half-cycles damage.

Figure 4.6(a) displays, for $k = 3$, a typical trend of the CoV over the number of counted cycles, for two limit cases $b = 1$ Hz and $b = 10$ Hz (the curves for other intermediate cases are not shown to avoid clutter). Other k values lead to identical trends.

Madsen et al.'s method overlaps results of time-domain simulations for a narrow-band process ($\alpha_1 = 0.998$, $\alpha_2 = 0.993$). The CoV decreases when the ideal unimodal tends to the limit wide-band case ($\alpha_1 = 0.866$, $\alpha_2 = 0.745$). Despite Madsen et al.'s method only applies to the narrow-band case, it agrees well (difference of about 25%) with the time-domain results for the wide-band case, too.

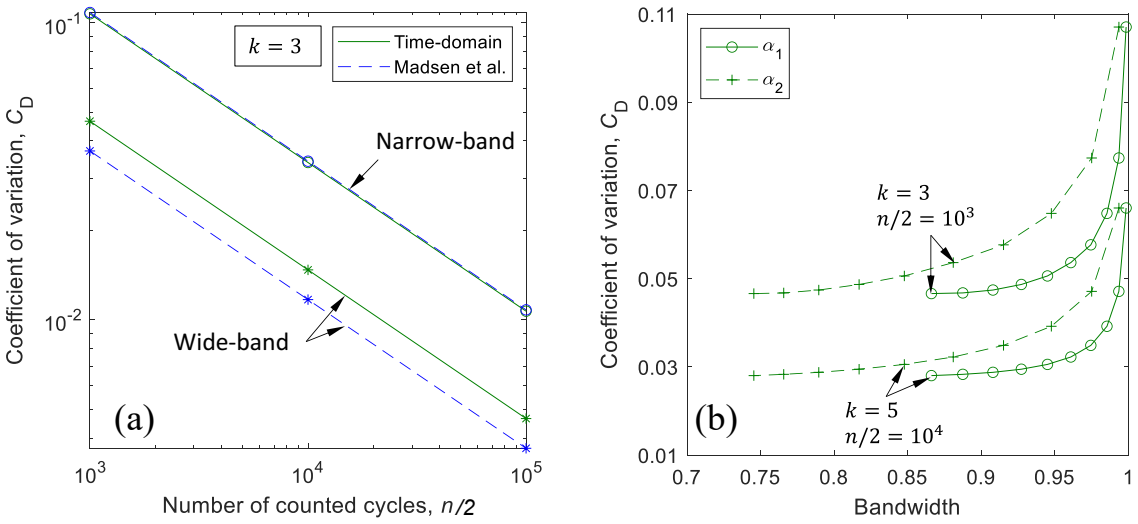

Figure 4.6. Ideal unimodal process: (a) CoV versus the number of cycles (for $k = 3$); (b) CoV versus α_1 and α_2, for two combinations of number of cycles and inverse slope k.

Figure 4.6(b) investigates the CoV as a function of the bandwidth parameters α_1 and α_2. This relationship in Figure 4.6(b) considers two combinations of inverse slope and number of cycles ($k = 3$ and 10^3; $k = 5$ and 10^4); similar trends are obtained for other combinations. The two bandwidth parameters, as already stated in Chapter 2, represent important physical properties of the random process: α_1 provides a unitless measure of the frequency distribution of the PSD of the process (and it controls some properties of the envelope of the process), whereas α_2 coincides with the irregularity factor of a Gaussian process. Not only are such bandwidth parameters used to classify a PSD type from narrow-band to wide-band, but they often enter the expressions used for

estimating the expected damage directly from a PSD (for example, the correction factor λ_{TB} in TB method is a function of α_1 and α_2, see [BEN05a,BEN05b]).

Figure 4.6(b) shows that the CoV increases with α_1 and α_2 (from wide-band to narrow-band process). If k and n are changed, the two trend lines shift upward or downward, while remaining almost unaltered.

4.4.3 Pierson-Moskowitz (P-M) and JONSWAP and power spectra

The results in Figure 4.6 suggests that similar tendencies could also characterize other power spectral densities. It was then decided to carry out additional simulations with the two PSDs considered in this section. Such power spectra are often encountered in offshore engineering and are selected here for illustrative purposes.

The Pierson-Moskowitz spectrum is described by the following equation [PIE64, BEN09]:

$$S_{\mathrm{X}}(f) = \frac{\alpha g^2}{(2\pi f)^4} \exp\left(-\frac{5}{4}\left(\frac{f_{\mathrm{p}}}{f}\right)^4\right) \tag{4.20}$$

where $f_{\mathrm{p}} = 1/T_{\mathrm{W}}$ is the peak frequency and T_{W} the dominant wave period of the spectrum, $\alpha \approx 5.061(H_s^2/T_{\mathrm{W}}^4)$, H_{s} the significant wave height, and g is the gravity constant.

The JONSWAP (Joint North Sea Wave Project) spectrum is a generalization of the P-M spectrum [BEN09b,HAS73]:

$$S_{\mathrm{X}}(f) = \frac{\alpha g^2}{(2\pi f)^4} \exp\left(-\frac{5}{4}\left(\frac{f_{\mathrm{p}}}{f}\right)^4 + \log(\gamma) \exp\left(\frac{-\left(\frac{f}{f_{\mathrm{p}}} - 1\right)^2}{2\sigma^2} \right) \right) \tag{4.21}$$

where $\alpha \approx 5.061(H_{\mathrm{s}}^2/T_{\mathrm{W}}^4)[1 - 0.287\ln(\gamma)]$ is the normalization factor and $\sigma = 0.07$ if $f < f_{\mathrm{p}}$ and $\sigma = 0.09$ if $f \geq f_{\mathrm{p}}$, and it is often $\gamma = 3.3$. Note that the two PSDs here analyzed, being not strictly narrow-band, are outside the range of applicability of the methods reviewed in Section 4.3, which therefore will not be applied for comparison purposes. The parameters defining both power spectra were assigned so to let the corresponding bandwidth parameters α_1 and α_2 vary over a wide range. The inverse slope varied from 2 to 9, as before.

For the two power spectra in this section, the relationship of CoV to parameter α_1 (see Figure 4.7) is of more interest than examining the relationship between CoV and the number of cycles, which follows a trend identical of other PSDs (see for example Figure 4.6(a)). For comparison purposes, Figure 4.7 plots the curves of all the four spectra examined so far. A common trend stands out clearly. Interestingly, when α_1 approaches unity, the linear oscillator has the higher values of CoV compared to the unimodal PSD with same α_1. In the region of lower α_1, the JONSWAP power spectrum is characterized by larger values of CoV. Instead, the ideal unimodal PSD always returns the lowest CoV.

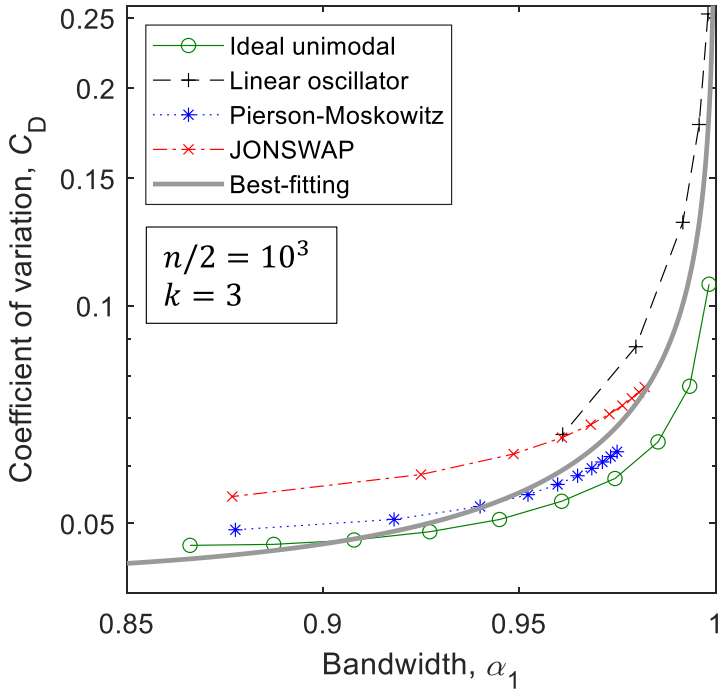

Figure 4.7. Comparison of the CoV for different PSDs, as a function of the bandwidth parameter α_1 (for $k = 3$ and 10^3 cycles). The continuous curve stands for the best-fitted line.

4.5 Empirical expressions to relate the CoV to bandwidth parameters

Figure 4.7 suggests that a common relationship exists between the CoV of the damage and the bandwidth parameter α_1. Furthermore, the curves in Figure 4.7 are not only increasing but – more importantly – also smooth. This attribute is helpful to represent the curves by a best-fitting expression. This expression should be as simple as possible to allow a straightforward evaluation of the CoV.

Based on the previous insights, it is reasonable to assume that the CoV be a function of α_1, k and $\nu_{\mathrm{p}}^{\mathrm{G}}T$ in the general form $(C_{\mathrm{D}})_{\mathrm{fit}}^{\mathrm{G}} = B(\alpha_1, k) \cdot \left(\nu_{\mathrm{p}}^{\mathrm{G}}T\right)^{-1/2}$. The constant of proportionality $B(\alpha_1, k)$ only depends on α_1 and k. The quantity $\nu_{\mathrm{p}}^{\mathrm{G}}T$ is the number of counted cycles in time T, which indeed equals the number of peaks. Using $\nu_{\mathrm{p}}^{\mathrm{G}}$

instead of ν_0^{G} to count the number of half-cycles makes the formula applicable to wide-band processes, either. In the narrow-band case obviously $\nu_0^{\mathrm{G}} \cong \nu_{\mathrm{p}}^{\mathrm{G}}$.

Cast this way, the $(C_{\mathrm{D}})_{\mathrm{fit}}^{\mathrm{G}}$ has the desirable property to approach zero for large T, and also to depend on four spectral moments λ_0, λ_1, λ_2, λ_4 through α_1 and $\nu_{\mathrm{p}}^{\mathrm{G}}$, similarly to the TB method [BEN05a,BEN05b].

The trends in Figure 4.7 suggest that, for k and $\nu_{\mathrm{p}}^{\mathrm{G}}T$ fixed, the function $(C_{\mathrm{D}})_{\mathrm{fit}}^{\mathrm{G}}$ has to be monotonic and satisfy the constraint $(C_{\mathrm{D}})_{\mathrm{fit}}^{\mathrm{G}} \to \infty$ when $\alpha_1 \to 1$. At the same time, when α_1 decreases the function seems to approach a limit value that changes with k and $\nu_{\mathrm{p}}^{\mathrm{G}}T$, see Figure 4.6 for the unimodal PSD. Among the mathematical expressions, a rationale polynomial is a candidate:

$$(C_{\mathrm{D}})_{\mathrm{fit}}^{\mathrm{G}} = \frac{c_1 \exp(k^{c_2})}{(1-{\alpha_1}^{c_3})^{c_4}} \left(\nu_{\mathrm{p}}^{\mathrm{G}}T\right)^{-1/2} \tag{4.22}$$

where c_1, c_2, c_3 and c_4 are unknown fitting coefficients, determined by minimizing the root-mean-square error between the proposed fitting expression, $(C_{\mathrm{D}})_{\mathrm{fit}}^{\mathrm{G}}$ and the time-domain simulations, $\hat{C}_{\mathrm{D}}$:

$$e = \sqrt{\frac{1}{q}\sum_{\mathrm{i}=1}^{\mathrm{q}} \left((C_{\mathrm{D}})_{\mathrm{fit,i}}^{\mathrm{G}} - \hat{C}_{\mathrm{D,i}}\right)^2} \tag{4.23}$$

The sum covers q combinations that result from all the considered values of α_1 and the inverse slope in the range $2 \le k \le 9$.

At first glance, a single curve to describe the trends seems hard to use in Figure 4.7 with a satisfactory degree of accuracy. For this reason, the coefficients c_{i} were calibrated for each PSD separately, see Table 4.1. As an example, for the unimodal PSD the final expression is:

$$(C_{\mathrm{D}})_{\mathrm{fit}}^{\mathrm{G}} = \frac{0.241\,\exp(k^{0.583})}{(1-{\alpha_1}^{19.4})^{0.253}}\left(\nu_{\mathrm{p}}^{\mathrm{G}}T\right)^{-\frac{1}{2}},\ \text{for } 2 \le k \le 9 \quad \text{and } 0.866 \le \alpha_1 \le 1 \tag{4.24}$$

The equation has no restrictions in the values of $\nu_{\mathrm{p}}^{\mathrm{G}}T$. Figure 4.8 confirms that the proposed formula agrees very well with the time-domain results, for a range of combinations of k and α_1 of practical interest – the figure refers to 10^3 cycles, but similar results are obtained for other values. In particular, the formula encompasses processes from narrow-band to mildly wide-band.

Table 4.1. Best-fitting coefficients of Eq. (4.22) for each type of PSD, along with the fitting error e from Eq. (4.23).

PSD type	c_1	c_2	c_3	c_4	e
Linear oscillator	0.148	0.589	5.57	0.459	0.012
Unimodal	0.241	0.583	19.3	0.253	0.006
JONSWAP	0.237	0.590	10.3	0.238	0.003
Pierson-Moskowitz	0.223	0.594	22.4	0.319	0.002
All spectra	0.195	0.593	13.4	0.389	0.060

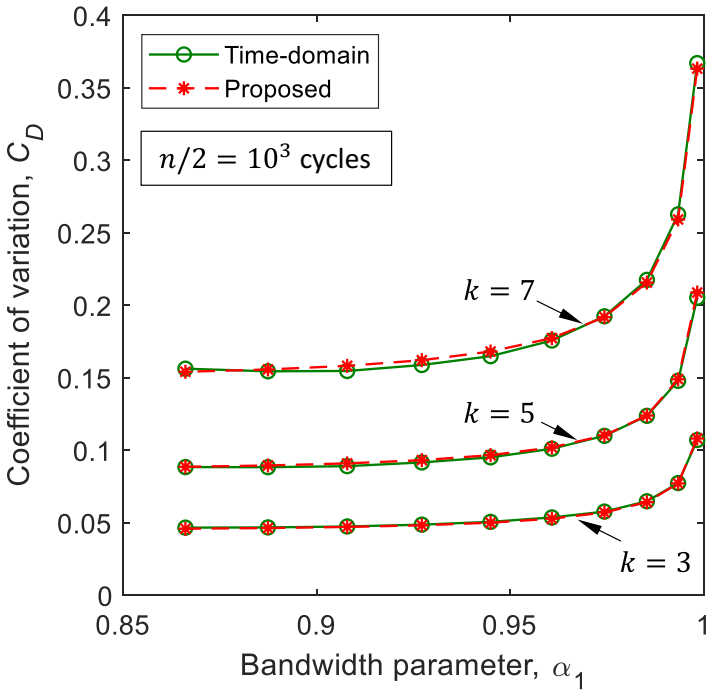

Figure 4.8. Ideal unimodal process: CoV versus α_1 (for 10^3 cycles). Comparison between the proposed best-fitting expression and the time-domain simulation results.

A comparable agreement was obtained for all the other PSDs, as confirmed by the similar fitting errors in the rightmost column of Table 4.1. Despite the data in Figure 4.7 are not perfectly overlapped, an effort was also performed to find out a single trend line, by calibrating Eq. (4.22) on all the data merged together. The coefficients are listed in the last row of Table 4.1. As expected, a larger error is obtained.

The advantage of using Eq. (4.22) lies in the fact that it does not require computing the autocorrelation coefficient function $\rho_X(l)$, which makes its practical use much easier than using the formula provided by the methods from the literature.

The relationship between CoV and α_1 emphasizes that Eq. (4.22) is merely empirical. In fact, it has been suggested by the observation of numerical results, rather than it being the outcome of theoretical arguments. Consequently, Eq. (4.24) does not compromise the validity of the theoretical solutions reviewed in the previous sections, but rather it is complementary to them.

Chapter 5

VARIANCE OF FATIGUE DAMAGE IN NON-GAUSSIAN RANDOM LOADING

5.1 INTRODUCTION

Chapter 4 reviewed four methods (i.e. Mark and Crandall, Bendat, Madsen et al., and Low) developed to calculate the variance of damage under narrow-band Gaussian random loading. Explicit formulae from the literature were compared with Monte Carlo simulations in time- and frequency-domain approaches. The coefficient of variation was presented as a smooth monotonic function of bandwidth parameters α_1 and α_2, a feature that permitted the proposition of a best-fitting expression. The proposed approach demonstrated to be simple and easy to use in practice and agreed well with time-domain simulation results. However, all methods including the proposed one are strictly applicable to Gaussian processes only. The hypothesis of the Gaussian process is not often satisfied by random loads acting on real engineering structures.

Non-Gaussian loads are encountered, for example, in certain types of wind or wave loading, or when the structure has a non-linear behavior that transforms a Gaussian input into a non-Gaussian output [BEN18b]. One interesting situation is that of offshore structures subjected to wave random loading, in which structural nonlinearity combines

with non-Gaussian input excitation. These examples emphasize that the study of non-Gaussian random loading is of particular relevance in structural durability. In spite of this, at present there are no analytical approaches able to assess the variance of fatigue damage in non-Gaussian loads. Apart from some exceptions [BEN09a], the methods existing in the literature are indeed valid for Gaussian loading only.

This chapter introduces the non-linear transformation, then it develops two theoretical models to estimate the variance of damage in stationary narrow-band non-Gaussian random processes. The models presented here extend two methods (Madsen et al. and Low) developed for narrow-band Gaussian processes. The models proposed in this chapter are based on a time-invariant non-linear transformation that links a non-Gaussian random process to its underlying Gaussian one. The transformation is calibrated on the values of skewness γ_3 and kurtosis γ_4 coefficients of the non-Gaussian process. This transformation enables the proposed models to estimate variance for any combination of skewness and kurtosis coefficients. The correctness of the proposed theoretical models was verified by Monte Carlo simulations, considering a linear oscillator response spectrum.

5.2 DEFINITION OF TRANSFORMATION

In this section a time-independent non-linear transformation $G(-)$ aims to include non-Gaussian effects in the Madsen et al.'s and the Low's method (see Chapter 4). The transformation relates a non-Gaussian loading with its underlying Gaussian one and vice versa. After this definition, one transformation form is reviewed to relate a non-Gaussian loading with its underlying Gaussian one and vice versa, i.e. the Winterstein's model.

The transformation $G(-)$ establishes a one-to-one relationship between the values of Gaussian and non-Gaussian processes. The non-Gaussian process is thus obtained as $Z(t) = G(X(t))$. Conversely, the Gaussian process $X(t) = g(Z(t))$ is transformed back

with the inverse function $g(-) = G^{-1}(-)$. The degree of non-linearity of the transformation is adjusted on the values of skewness γ_3 and kurtosis γ_4 characterizing the non-Gaussian process (usually, $\gamma_3 \neq 0$ and $\gamma_4 \neq 3$). If $\gamma_3 = 0$ and $\gamma_4 = 3$, the process $Z(t)$ becomes Gaussian and the transformation linear. The transformation should be monotonically increasing to obtain a non-Gaussian process correctly. The transformation is independent of t.

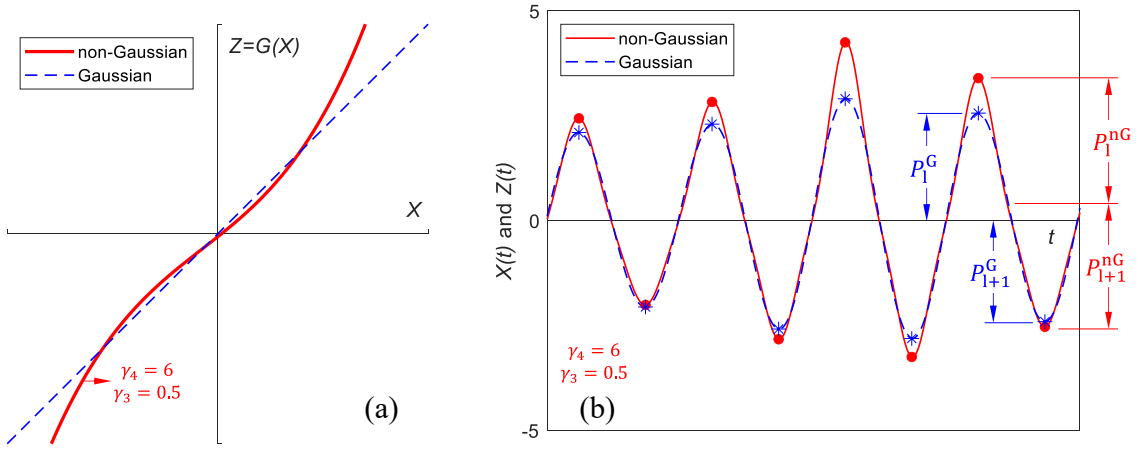

Figure 5.1. (a) Linear and non-linear transformation; (b) Gaussian and its corresponding transformed non-Gaussian random process (dashed line refers to Gaussian and solid line to non-Gaussian).

Different forms of either the direct or the inverse transformation are available in the literature: Ochi's model is a monotonic exponential function [OCH94], Winterstein's model is based on cubic Hermite polynomials [WIN85,WIN88,WIN94], whereas the transformation of Sarkani et al. employs a power law model [KIH95,SAR94]. Among them, only the Winterstein's model provides the analytical expressions of both $G(-)$ and $g(-)$. This aspect is very beneficial in the development of the non-Gaussian solutions for the variance, presented in this section. An example of linear and non-linear transformations is represented in Figure 1.1(a); the non-linear case is obtained by the Winterstein's model and refers to values $\gamma_3 = 0.5$ and $\gamma_4 = 6$.

The transformation may introduce some harmonic distortion on the power spectrum $S_Z(f)$ of the transformed process $Z(t)$ if a high degree of non-linearity (e.g. high kurtosis value) has in the process [SMA05]. However, if the degree of non-linearity of $G(-)$ is not too high, the distortion is satisfactory and both processes have similar spectral contents [SMA05].

5.2.1 Winterstein's model

The Winterstein's model is reviewed in this section depending upon the Hermite polynomials. In particular, it reports only the expressions of the inverse transformation $g(-)$, as this function along with its first derivative are utilized by the models developed in next sections.

For a leptokurtic process ($\gamma_4 > 3$), the inverse transformation is (the time t variable is omitted for clarity) [WIN94]:

$$g(Z) = \left[\sqrt{\xi^2(Z) + a_3} + \xi(Z)\right]^{\frac{1}{3}} - \left[\sqrt{\xi^2(Z) + a_3} - \xi(Z)\right]^{\frac{1}{3}} - a_1 \tag{5.1}$$

where

$$\xi(Z) = \frac{3a_2}{2}\left(a_1 + \frac{Z - \mu_Z}{\kappa\sigma_Z}\right) - a_1^3 \tag{5.2}$$

in which μ_Z is the mean value and σ_Z the standard deviation of the non-Gaussian process, and the constants $a_1 = h_3/(3h_4)$, $a_2 = 1/(3h_4)$, $a_3 = (a_2 - 1 - a_1^2)^3$. The scale factor $\kappa = (1 + 2h_3^2 + 6h_4^2)^{-1/2}$ assures that both the Gaussian and non-Gaussian process have a common value of variance, $\sigma_X^2 = \sigma_Z^2$.

The non-dimensional coefficients h_3 and h_4 carry on slightly different expressions, depending on the version of the method. The earliest version [WIN85] was

a first-order model limited to small non-Gaussian degrees. The later version [WIN94] incorporated also a second-order term and provides the following expressions:

$$h_3 = \frac{\gamma_3}{6}\left[\frac{1 - 0.015|\gamma_3| + 0.3\gamma_3^2}{1 + 0.2(\gamma_4 - 3)}\right]; \qquad h_4 = h_{40}\left(1 - \frac{1.43\gamma_3^2}{\gamma_4 - 3}\right)^{1-0.1\gamma_4^{0.8}} \tag{5.3}$$

where

$$h_{40} = \frac{[1 + 1.25(\gamma_4 - 3)]^{1/3} - 1}{10} \tag{5.4}$$

These coefficients fit in the intervals $0 < \gamma_3^2 < 2(\gamma_4 - 3)/3$ and $3 < \gamma_4 < 15$, which comprise most non-Gaussian cases.

For a platykurtic process ($\gamma_4 < 3$), the inverse transformation is:

$$g(Z) = Z_0 - \widetilde{h_3}(Z_0^2 - 1) - \widetilde{h_4}(Z_0^3 - 3Z_0) \tag{5.5}$$

where $Z_0 = (Z - \mu_Z)/\sigma_Z$ is a standardised process; the parameters $\widetilde{h_3} = \gamma_3/6$ and $\widetilde{h_4} = (\gamma_4 - 3)/24$ are Hermite moments.

Despite the fact that the Winterstein's model includes several non-Gaussian cases, it does not accept all combinations of γ_3, γ_4 values. For more details, see [WIN88].

5.3 SOLUTION BASED ON LOW'S METHOD

The Low's model for the variance of damage in Chapter 4 is now extended to the non-Gaussian case. This model depends on four properties of a narrow-band Gaussian process:

i) the expected number of half-cycles in time interval T is equal to the frequency of upward crossings, $E[n(T)] = 2\nu_0^{\mathrm{G}}T$;

ii) the time lag between two peaks $P_{\mathrm{l}}^{\mathrm{G}}$ and $P_{\mathrm{l}+1}^{\mathrm{G}}$ is $\tau = l/\left(2\nu_0^{\mathrm{G}}\right)$;

iii) the JPDF of two peaks $f_{\mathrm{P}_0,\mathrm{P}_{\mathrm{l}}}^{\mathrm{G}}\left(x_{\mathrm{p}}, x_{\mathrm{v}}\right)$ is the Rice distribution (see Chapter 4), which is used to derive the autocorrelation coefficient $\rho_{\mathrm{d}_0,d_{\mathrm{l}}}^{\mathrm{G}}(l)$;

iv) the probability distribution of peaks $f_{\mathrm{P}_0}^{\mathrm{G}}(x_{\mathrm{p}})$ is known to be a Rayleigh distribution.

The first and second conditions are, indeed, very general and hold true also for a narrow-band process that is non-Gaussian, as they only depend on characteristics of a narrow-band process. The third and fourth conditions, instead, require the Gaussian hypothesis for the process.

A useful characteristic of the non-linear transformations $G(-)$ and $g(-)$ is that to establish a one-to-one relationship between a value in a Gaussian process at any time instant and its transformed value in the non-Gaussian process, at the same time instant. This relationship guarantees that peaks, valleys and mean value crossings are placed exactly at the same time instants in both processes. Figure 1.1(b) highlights this relationship for the peaks in the Gaussian and non-Gaussian process.

For example, if the Gaussian process crosses its mean value μ_{X} at time t_1, that is $X(t_1) = \mu_{\mathrm{X}}$, the non-Gaussian process will cross its mean value μ_{Z} also at t_1, that is $Z(t_1) = \mu_{\mathrm{Z}}$. Furthermore, if $X(t)$ has a peak $x_{\mathrm{p}}(t)$ or valley $x_{\mathrm{v}}(t)$ at time instant t, the non-Gaussian process will have a corresponding peak or valley at the same time instant, $z_{\mathrm{p}}(t) = G\left(x_{\mathrm{p}}(t)\right)$ and $z_{\mathrm{v}}(t) = G(x_{\mathrm{v}}(t))$. The same condition holds true also for the

inverse relationship $x_{\mathrm{p}}(t) = g\big(z_{\mathrm{p}}(t)\big)$ and $x_{\mathrm{v}}(t) = g(z_{\mathrm{v}}(t))$. Consequently, the previous property suggests that both the Gaussian and non-Gaussian process have in common the autocorrelation coefficient, that is $\rho_{\mathrm{X}}(l) \cong \rho_{\mathrm{Z}}(l)$.

Another and more important consequence is that the relative positions of peaks and valleys in both processes are maintained for a monotonic transformation. For example, two peaks will be $z_{\mathrm{p}}(t_1) > z_{\mathrm{p}}(t_2)$ in the non-Gaussian process if they are transformed by $G(-)$ from two peaks $x_{\mathrm{p}}(t_1) > x_{\mathrm{p}}(t_2)$ at any time instants t_1, t_2 in the Gaussian process. Obviously, the same concept relates to valleys as well. This is the same as saying that if the Gaussian process has peaks $P_{\mathrm{l}}^{\mathrm{G}} > P_{\mathrm{l}+1}^{\mathrm{G}}$ at time lag l, the non-Gaussian process will have peaks $P_{\mathrm{l}}^{\mathrm{nG}} > P_{\mathrm{l}+1}^{\mathrm{nG}}$ at the same time lag.

The above insights may be summarized by stating that a non-linear transformation from a Gaussian to a non-Gaussian process preserves the number of mean value crossings, and either increases or decreases (depending on γ_3, γ_4) the values of peaks and valleys, keeping their relative positions unaltered. This property, in particular, guarantees that, in the non-Gaussian process, half-cycles are formed by peak/valley pairs that are transformed from the corresponding peak/valley pairs in the Gaussian process, and that the non-Gaussian half-cycles have amplitudes smaller or larger (depending on γ_3, γ_4) than the corresponding amplitudes of the Gaussian half-cycles.

Considering the earlier observations, the four properties summarized in the previous list can easily be adapted to the non-Gaussian case. More precisely, in a non-Gaussian narrow-band process:

i) the expected number of half-cycles in time interval T is equal to the frequency of upward crossings: $E[n(T)] = 2\nu_0^{\mathrm{nG}}T$, where $\nu_0^{\mathrm{nG}} = \nu_0^{\mathrm{G}}$;
ii) the time lag between two peaks $P_{\mathrm{l}}^{\mathrm{nG}}$ and $P_{\mathrm{l}+1}^{\mathrm{nG}}$ is $\tau = l/(2\nu_0^{\mathrm{nG}})$;
iii) the autocorrelation coefficient $\rho_{\mathrm{d_0,d_l}}^{\mathrm{nG}}(l)$ is derived from the JPDF $f_{\mathrm{P_0,P_l}}^{\mathrm{nG}}(z_{\mathrm{p}}, z_{\mathrm{v}})$ of two peaks, which is obtained as a variable transformation of the Rice distribution;
iv) the distribution of peaks for non-Gaussian $f_{\mathrm{P_0}}^{\mathrm{nG}}(z_{\mathrm{p}})$ is obtained by a variable transformation of the Rayleigh distribution valid in the Gaussian case;

The first two properties are evident; the other two requires some explaining. The third condition is now elaborated further. Hereafter, a pair of any two extremes z_{p} and z_{v} (peak and valley) is considered in the non-Gaussian process. They are random variables with joint probability density function, say $f_{\mathrm{P_0,P_l}}^{\mathrm{nG}}(z_{\mathrm{p}}, z_{\mathrm{v}})$. Such extremes are transformed back to two corresponding extremes $x_{\mathrm{p}} = g(z_{\mathrm{p}})$ and $x_{\mathrm{v}} = g(z_{\mathrm{v}})$ (peak and valley) in the Gaussian process through the inverse transformation $g(-)$. For the Gaussian extremes is valid the joint Rice distribution. The joint distribution of the non-Gaussian extremes can be derived by the rule of transformed random variables [LUT04]:

$$f_{\mathrm{P_0,P_l}}^{\mathrm{nG}}(z_{\mathrm{p}}, z_{\mathrm{v}}) = f_{\mathrm{P_0,P_l}}^{\mathrm{G}}(x_{\mathrm{p}}, x_{\mathrm{v}}) \cdot |\,\mathbf{J}(x_{\mathrm{p}}, x_{\mathrm{v}})\,| \tag{5.6}$$

where symbol $|-|$ means "absolute value" and $\mathbf{J}$ is the Jacobian of the transformation $g(-)$, which turns out from the following 2×2 determinant:

$$\mathbf{J}(x_{\mathrm{p}}, x_{\mathrm{v}}) = \begin{vmatrix} \dfrac{\partial g(z_{\mathrm{p}})}{\partial z_{\mathrm{p}}} & \dfrac{\partial g(z_{\mathrm{p}})}{\partial z_{\mathrm{v}}} \\ \dfrac{\partial g(z_{\mathrm{v}})}{\partial z_{\mathrm{p}}} & \dfrac{\partial g(z_{\mathrm{v}})}{\partial z_{\mathrm{v}}} \end{vmatrix} \tag{5.7}$$

The inverse transformation should be applied to peak and valley variables separately. As a result, the Jacobian in Eq. (5.7) is, in fact, a diagonal matrix. Intuition suggests, for

example, that an infinitesimal change in the non-Gaussian peak ∂z_{p} produces no variation in the corresponding valley ∂z_{v}, and therefore $\partial g(z_{\mathrm{p}})/\partial z_{\mathrm{v}} = 0$. A similar interpretation applied to the other out-of-diagonal term explains why $\partial g(z_{\mathrm{v}})/\partial z_{\mathrm{p}} = 0$.

By the Rice formula (see Chapter 4), the general expression in Eq. (5.6) can be written more specifically as:

$$f_{\mathrm{P_0,P_1}}^{\mathrm{nG}}(z_{\mathrm{p}}, z_{\mathrm{v}}) = \frac{g(z_{\mathrm{p}})g(z_{\mathrm{v}})}{1-\rho_{\mathrm{Z}}^2(l)} I_0\left(\frac{g(z_{\mathrm{p}})g(z_{\mathrm{v}})\,\rho_{\mathrm{Z}}(l)}{1-\rho_{\mathrm{Z}}^2(l)}\right) e^{-\frac{g(z_{\mathrm{p}})^2+g(z_{\mathrm{v}})^2}{2\left(1-\rho_{\mathrm{Z}}^2(l)\right)}} \left|\frac{\partial g(z_{\mathrm{p}})}{\partial z_{\mathrm{p}}} \cdot \frac{\partial g(z_{\mathrm{v}})}{\partial z_{\mathrm{v}}}\right| \tag{5.8}$$

Although not written explicitly, the Bessel function $I_0(z_{\mathrm{p}}, z_{\mathrm{v}})$ in Eq. (5.8) is a function of z_{p} and z_{v}, and it is obtained by a simple change of variables in the corresponding function $I_0(x_{\mathrm{p}}, x_{\mathrm{v}})$ (see Chapter 4), which instead depends on the variables x_{p} and x_{v}.

The expression in Eq. (5.8) represents the joint distribution of two peaks in the non-Gaussian process $Z(t)$. As the transformation of variables involves the non-linear function $g(z_{\mathrm{p}})$ and its derivatives, the final expression is so complex that is not possible to arrive at a closed-form solution. A numerical approach should be used.

Eq. (5.8) depends on both γ_3 and γ_4 through function $g(z_{\mathrm{p}})$. It is also function of μ_{Z}, σ_{Z}^2 and ρ_{Z}. Obviously, in the limiting case $\gamma_3 = 0$ and $\gamma_4 = 3$ (Gaussian process), Eq. (5.8) converges to Rice distribution.

Figure 5.2(a) compares the Gaussian and non-Gaussian joint probability distributions of peaks (the latter obtained with $\mu_{\mathrm{Z}} = 0$, $\sigma_{\mathrm{Z}}^2 = 1$, $\rho_{\mathrm{Z}} = 0$, $\gamma_3 = 0.5$ and $\gamma_4 = 6$). The distributions are plotted on the region of positive values about peaks. The shift of probabilities is clear. If compared to the Gaussian case, the non-Gaussian distribution shows higher levels of probability towards larger peak values.

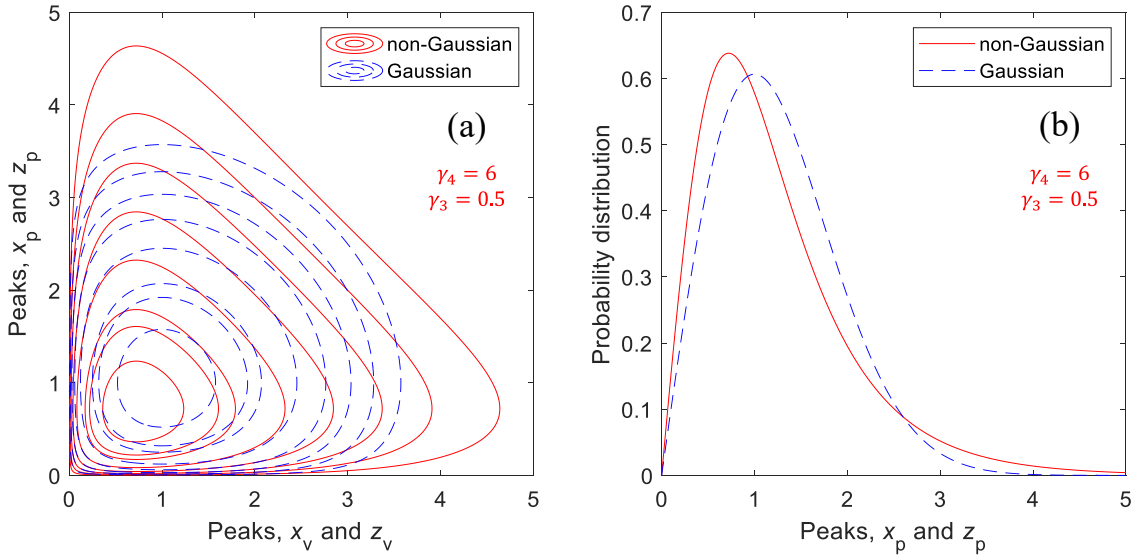

Figure 5.2. (a) Joint probability density function of peaks and (b) its marginal probability density function of peaks.

The non-Gaussian peak-peak joint distribution obtained so far allows the damage correlation $E\left[d_0^{\mathrm{nG}} d_1^{\mathrm{nG}}\right]$ to be computed with no much effort by solving numerically the double integral in Chapter 4. Attention should be paid in the numerical integration when the kurtosis γ_4 is very large. In this circumstance, indeed, the non-Gaussian variables z_{p}, z_{v} extend over a wide interval that needs to be finely discretized to assure the necessary numerical precision.

The last point iv) in the previous list for the non-Gaussian process is finally considered. In the same way as Eq. (5.6), the probability density function of peaks in the non-Gaussian process is determined by a variable transformation [LUT04]:

$$f_{\mathrm{P_0}}^{\mathrm{nG}}(z_{\mathrm{p}}) = f_{\mathrm{P_0}}^{\mathrm{G}}(x_{\mathrm{p}}) \left| \frac{\partial g(z_{\mathrm{p}})}{\partial z_{\mathrm{p}}} \right| \tag{5.9}$$

Making use of Eq. (5.9) and introducing the transformed random variable $x_\mathrm{p} = g(z_\mathrm{p})$ into the formula of the Rayleigh distribution $f_{\mathrm{P}_0}^{\mathrm{G}}(x_\mathrm{p})$, the probability distribution of peaks in the non-Gaussian case can be written as:

$$f_{\mathrm{P}_0}^{\mathrm{G}}(z_\mathrm{p}) = \frac{g(z_\mathrm{p})}{\sigma_\mathrm{Z}^2}\, e^{-\frac{\left(g(z_\mathrm{p})\right)^2}{2\sigma_\mathrm{Z}^2}} \left|\frac{\partial g(z_\mathrm{p})}{\partial z_\mathrm{p}}\right| \tag{5.10}$$

Equation (5.10) depends on the four statistics $\mu_\mathrm{Z}, \sigma_\mathrm{Z}^2, \gamma_3, \gamma_4$ characterising the non-Gaussian process $Z(t)$. It converges to a Rayleigh distribution when $\gamma_3 = 0$ and $\gamma_4 = 3$ (Gaussian process).

A comparison of the Gaussian and the non-Gaussian (transformed) distribution is sketched in Figure 5.2(b). It refers to $\mu_\mathrm{Z} = 0$, $\sigma_\mathrm{Z}^2 = 1$, $\gamma_3 = 0.5$ and $\gamma_4 = 6$. The wider tail in the non-Gaussian distribution provides higher levels of probability towards larger peak values.

Similarly to the expected damage per half-cycle $E[d]$ in Chapter 3, the expected value of the damage $E\left[d_0^{\mathrm{nG}}\right]$ and its square $E\left[\left(d_0^{\mathrm{nG}}\right)^2\right]$ are nothing more than the moments of order k and $2k$, respectively, of the probability distribution $f_{\mathrm{P}_0}^{\mathrm{nG}}(z_\mathrm{p})$ just introduced. On substituting the non-Gaussian distribution in Eq. (5.10) into $E[d]$ in Chapter 3, the general expression that gives both expected damage values are:

$$E\left[\left(d_0^{\mathrm{nG}}\right)^{\mathrm{q}}\right] = \frac{1}{(2A)^{\mathrm{q}}} \int_0^\infty z_\mathrm{p}^{\mathrm{q\cdot k}}\, \frac{g(z_\mathrm{p})}{\sigma_\mathrm{Z}^2}\, e^{-\frac{\left(g(z_\mathrm{p})\right)^2}{2\sigma_\mathrm{Z}^2}} \left|\frac{\partial g(z_\mathrm{p})}{\partial z_\mathrm{p}}\right| \mathrm{d}z_\mathrm{p} \tag{5.11}$$

where the exponent q is 1 or 2. Note that this expression is only a function of $\mu_\mathrm{Z}, \sigma_\mathrm{Z}^2, \gamma_3, \gamma_4$.

The variance of the fatigue damage for the non-Gaussian process is finally obtained through σ_{D}^2 in Chapter 4, in which the quantities $E\left[d_0^{\mathrm{nG}} d_{\mathrm{l}}^{\mathrm{nG}}\right]$, $E[(d_0^2)^{\mathrm{nG}}]$ and $E\left[d_0^{\mathrm{nG}}\right]$ calculated so far for the non-Gaussian process have to be used:

$$(\sigma_{\mathrm{D}}^2)_{\mathrm{Low}}^{\mathrm{nG}} = n\left(E[(d_0^2)^{\mathrm{nG}}] - E\left[d_0^{\mathrm{nG}}\right]^2\right) + 2\sum_{\mathrm{l}=1}^{\mathrm{n}-1}(n-l)\left(E\left[d_0^{\mathrm{nG}} d_{\mathrm{l}}^{\mathrm{nG}}\right] - E\left[d_0^{\mathrm{nG}}\right]^2\right) \tag{5.12}$$

This expression extends the Low's method to the non-Gaussian case. Note that $E[(d_0^2)^{\mathrm{nG}}]$ means "expected value of the damage squared", whereas $E\left[d_0^{\mathrm{nG}}\right]^2$ means "expected damage squared".

The corresponding expression of the CoV for the non-Gaussian process becomes:

$$(C_{\mathrm{D}})_{\mathrm{Low}}^{\mathrm{nG}} = \frac{1}{n}\sqrt{n\left(\frac{E[(d_0^2)^{\mathrm{nG}}]}{E\left[d_0^{\mathrm{nG}}\right]^2} - 1\right) + \frac{2\sum_{\mathrm{l}=1}^{\mathrm{n}-1}(n-l)\left(E\left[d_0^{\mathrm{nG}} d_{\mathrm{l}}^{\mathrm{nG}}\right] - E\left[d_0^{\mathrm{nG}}\right]^2\right)}{E\left[d_0^{\mathrm{nG}}\right]^2}} \tag{5.13}$$

5.4 SOLUTION BASED ON MADSEN ET AL.'S METHOD

For the Gaussian case, the Madsen et al.'s solution basically relies on the damage autocorrelation coefficient $\rho_{\mathrm{d_0,d_l}}^{\mathrm{G}}(l)$ in Chapter 4. Extension to the non-Gaussian case is straightforward. It is based on the property, already discussed in previous section, that the transformation $G(-)$ has of keeping unaltered the position in time of each value of the Gaussian and non-Gaussian process. This property also ensures that both processes cross

their mean values at the same instant of time. Taken together, both properties suggest that the Gaussian and non-Gaussian processes have in common the autocorrelation coefficient, $\rho_{\mathrm{Z}}(l) \cong \rho_{\mathrm{X}}(l)$, and the same frequency of upward crossings, $\nu_0^{\mathrm{nG}} = \nu_0^{\mathrm{G}}$.

Consequently, for the non-Gaussian process and any value of k, the autocorrelation coefficient of the damage is:

$$\rho_{\mathrm{d_0,d_l}}^{\mathrm{nG}}(l) \cong \frac{\Gamma^2\left(1+\frac{k}{2}\right)\left[{}_2F_1\left(-\frac{k}{2},-\frac{k}{2};1;\rho_{\mathrm{Z}}^2(l)+\left(\frac{\rho_{\mathrm{Z}}'(l)}{2\pi\nu_0^{\mathrm{nG}}}\right)^2\right)-1\right]}{\left[\Gamma(1+k)-\Gamma^2\left(1+\frac{k}{2}\right)\right]} \tag{5.14}$$

where symbols $\rho_{\mathrm{Z}}(l)$ and ν_0^{nG} have been used only to emphasize that the formula holds for the non-Gaussian case. Compared to the non-Gaussian Low's method, the coefficient $\rho_{\mathrm{d_0,d_l}}^{\mathrm{nG}}(l)$ can be obtained with no difficulty, since the transformed JPDF $f_{\mathrm{P_0,P_l}}^{\mathrm{nG}}(x_{\mathrm{p}}, x_{\mathrm{v}})$ in Eq. (5.8) is not involved.

The coefficient $\rho_{\mathrm{d_0,d_l}}^{\mathrm{nG}}(l)$ in Eq. (5.14) enters directly into the variance expression σ_{D}^2 in Chapter 4. The other two damage values, $E[d_0^2]$ and $E[d_0]^2$, are determined exactly as for the Low's method for the non-Gaussian case; the fourth property iv) from the list in previous section remains indeed unchanged. Therefore, the distribution of peaks for non-Gaussian $f_{\mathrm{P_0}}^{\mathrm{nG}}(z_{\mathrm{p}})$ follows from a variable transformation of the Rayleigh distribution, see Eq. (5.10). The terms $E\left[d_0^{\mathrm{nG}}\right]$ and $E\left[\left(d_0^{\mathrm{nG}}\right)^2\right]$ are calculated with Eq. (5.11).

If all previous results are put together, the variance of the fatigue damage according to Madsen et al. turns out to be:

$$(\sigma_{\mathrm{D}}^2)_{\mathrm{Mad}}^{\mathrm{nG}} = \left[n + 2\sum_{\mathrm{l}=1}^{\mathrm{n}-1}(n-l)\,\rho_{\mathrm{d_0,d_l}}^{\mathrm{nG}}(l)\right]\left(E[(d_0^2)^{\mathrm{nG}}] - E\left[d_0^{\mathrm{nG}}\right]^2\right) \tag{5.15}$$

The corresponding expression of the CoV is:

$$(C_{\mathrm{D}})_{\mathrm{Mad}}^{\mathrm{nG}} = \frac{1}{n}\sqrt{\left[n + 2\sum_{l=1}^{n-1}(n-l)\rho_{\mathrm{d_0,d_l}}^{\mathrm{nG}}(l)\right]\left(\frac{E[(d_0^2)^{\mathrm{nG}}]}{E\left[d_0^{\mathrm{nG}}\right]^2} - 1\right)} \tag{5.16}$$

In both equations, the autocorrelation coefficient of the damage $\rho_{\mathrm{d_0,d_l}}^{\mathrm{nG}}(l)$ is identical for both the Gaussian and the non-Gaussian process, as clarified above. The non-Gaussian effect enters, through the transformation $g(-)$, into the last two terms $E[(d_0^2)^{\mathrm{nG}}]$ and $E\left[d_0^{\mathrm{nG}}\right]$.

5.5 NUMERICAL EXAMPLE

Numerical simulations are used to verify the correctness of the two non-Gaussian models described previously. The two models are compared with time-domain results obtained via Monte Carlo method. This study is also used to investigate how the variance and the coefficient of variation vary as a function of the skewness, kurtosis and the S-N inverse slope.

Simulations consider the linear oscillator response spectrum $S_{\mathrm{X}}(f)$ from Chapter 4. A brief description of main parameters is reproduced in this chapter since they play a significant role in the spectrum $S_{\mathrm{X}}(f)$. Indeed, the system considered has a natural frequency of 10 Hz and a light damping $\zeta = 0.005$. It is subjected to a band-limited random base acceleration, $W(t)$, with a frequency content from 0 to 20 Hz. Analytical expressions are derived for the mass absolute displacement, $U(t)$, and the relative displacement, $X(t) = U(t) - W(t)$. The relative displacement response spectrum $S_{\mathrm{X}}(f)$ turns out to be a narrow-band random Gaussian process, with bandwidth parameters $\alpha_1 = 0.998$ and $\alpha_2 = 0.994$. The power spectrum is normalised to unit variance, $\lambda_0 = 1$.

A total of $N = 2 \times 10^5$ Gaussian random time-histories $x_\mathrm{i}(t)$, $i = 1,2,3, \dots N$ of time length T are simulated from $S_\mathrm{X}(f)$. Three different lengths T are chosen so that time-histories have approximately 10^3, 10^4 and 10^5 fatigue cycles.

Winterstein's model is then used to transform each $x_\mathrm{i}(t)$ into a non-Gaussian time-history $z_\mathrm{i}(t)$ with prescribed values of skewness γ_3 and kurtosis γ_4. Simulations scrutinise the ranges $0 < \gamma_3^2 < 0.5$ and $2 < \gamma_4 < 8$, which cover most of the cases of practical interest. It has, however, to be noticed that Winterstein's model imposes some restrictions on the values of γ_3 and γ_4 that can be paired [WIN94].

For each time-history, $x_\mathrm{i}(t)$ and $z_\mathrm{i}(t)$, the fatigue damage values $D_\mathrm{i}^\mathrm{G}(T)$ and $D_\mathrm{i}^\mathrm{nG}(T)$ are calculated in time-domain by the rainflow counting and Palmgren-Miner rule. Damage calculation considers a S-N curve with strength coefficient $A = 1$ and several values of the inverse slope $k = 3, 6, 9$, which cover typical values from notched to smooth components.

The sample mean $\overline{D} = N^{-1} \sum_{\mathrm{i}=1}^{\mathrm{N}} D_\mathrm{i}$, sample variance $\hat{\sigma}_\mathrm{D}^2 = (N-1)^{-1} \sum_{\mathrm{i}=1}^{\mathrm{N}} (D_\mathrm{i} - \overline{D})^2$ and sample coefficient of variation $\hat{C}_\mathrm{D} = \hat{\sigma}_\mathrm{D} / \overline{D}$ are computed from the set of damage values for both the Gaussian and the non-Gaussian case. The expected damage, instead, was computed through analytical solutions: the Gaussian expected damage $E[D^\mathrm{G}(T)]_\mathrm{NB}$ from Chapter 3, the non-Gaussian expected damage $E[D^\mathrm{nG}(T)] = 2\nu_0^\mathrm{nG} T \cdot E[d^\mathrm{nG}]$ by taking $q = 1$ in Eq. (5.11).

Figure 5.3 displays the trend of the sample mean $\overline{D}$ and the standard deviation of damage $\hat{\sigma}_\mathrm{D}$ (normalised to the expected damage) for both the Gaussian and non-Gaussian case, as a function of the number of counted cycles. The figure refers to an inverse slope $k = 3$ and a non-Gaussian process with $\gamma_3 = 0.5$ and $\gamma_4 = 6$. In either case, the greater is the number of counted cycles, the lower is the dispersion of the damage around its mean value. For any number of cycles, the non-Gaussian damage always has a variance higher than the Gaussian damage. A similar result, not shown here, is observed for other values $\gamma_4 > 3$. This increase in the variance of damage highlights the importance of considering the non-Gaussian effect.

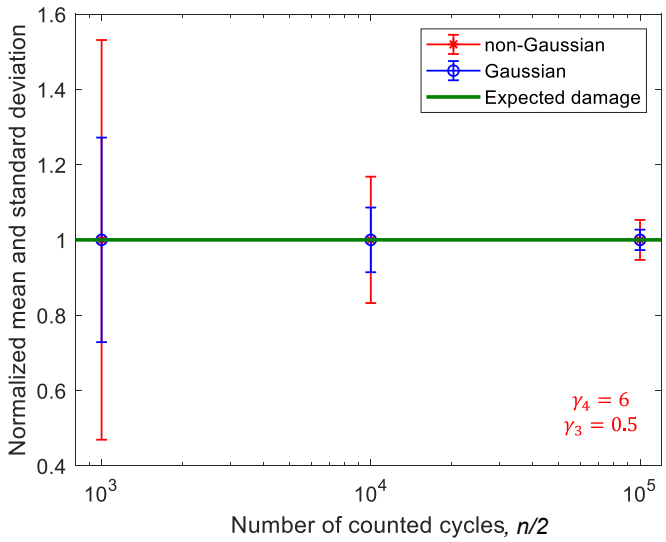

Figure 5.3. Standard deviation normalized to the expected damage as a function of the number of counted cycles.

The trend in Figure 5.3 is further clarified in Figure 5.4, which shows the change of the CoV versus the number of counted cycles for both methods of Low and Madsen et al. Figure 5.4 refers to an inverse slope $k = 3$ and two different non-Gaussian cases: $\gamma_3 = 0.5$, $\gamma_4 = 2$ (platykurtic) and $\gamma_3 = 0.5$, $\gamma_4 = 6$ (leptokurtic).

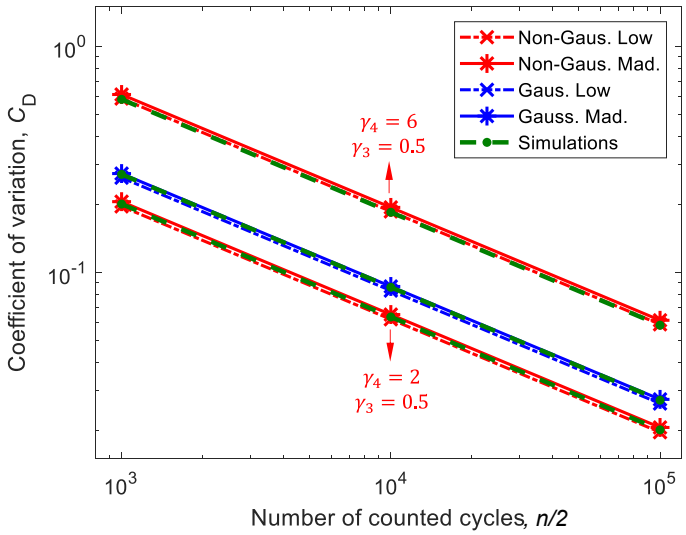

Figure 5.4. Coefficient of variation of damage as a function of the number of counted cycles.

A perfect matching is observed between time-domain results and theoretical estimations, either Gaussian or non-Gaussian. The agreement in the Gaussian case is somehow predictable [MAR19b]. Of more interest here is the correct estimation provided by the non-Gaussian models, whose exactness is thus verified. Furthermore, the figure also shows that the non-Gaussian models by Low and Madsen et al. are almost equivalent.

The very small, if not almost negligible, discrepancy between theoretical and simulation results in Figure 5.4 has to be attributed to numerical approximations. This approximation tends to occur for kurtosis values $\gamma_4 > 6$ or even greater. One approximation comes from the Winterstein's model, in which there are some best-fitting coefficients. Another approximation source comes from the numerical solution of the double-integral used to compute $E\left[d_0^{\mathrm{nG}} d_{\mathrm{l}}^{\mathrm{nG}}\right]$ through the JPDF $f_{\mathrm{P}_0,\mathrm{P}_{\mathrm{l}}}^{\mathrm{nG}}\left(z_{\mathrm{p}}, z_{\mathrm{v}}\right)$ in the Low's model; for very high γ_4 values, the tails of the joint probability distribution tend to be represented not exactly.

In any case, the largest difference between theory and simulation is 3%, which is perfectly acceptable. In summary, the previous results confirm that the two non-Gaussian models are practically equivalent, and they are not only exact but also cover combinations of skewness and kurtosis over a wide range of values of practical interest, that is within the limits of Winterstein's model $0 < \gamma_3^2 < 2(\gamma_4 - 3)/3$ and $1 < \gamma_4 < 15$.

An overall picture is finally given on the effect of skewness γ_3, kurtosis γ_4 and inverse slope k on the relative variation of the non-Gaussian CoV with respect to the Gaussian case. In particular, Figure 5.5 shows the trend of the ratio $r = (C_{\mathrm{D}})_{\mathrm{Mad}}^{\mathrm{nG}} / (C_{\mathrm{D}})_{\mathrm{Mad}}^{\mathrm{G}}$ of the coefficient of variation computed by Madsen et al.'s method in either its Gaussian or non-Gaussian version. The Gaussian CoV, $(C_{\mathrm{D}})_{\mathrm{Mad}}^{\mathrm{G}}$, follows from Chapter 4, the non-Gaussian one, $(C_{\mathrm{D}})_{\mathrm{Mad}}^{\mathrm{nG}}$, from Eq. (5.16). As said above, the estimations $(C_{\mathrm{D}})_{\mathrm{Low}}^{\mathrm{G}}$ and $(C_{\mathrm{D}})_{\mathrm{Low}}^{\mathrm{nG}}$ of the Low's model are identical and are thus not shown.

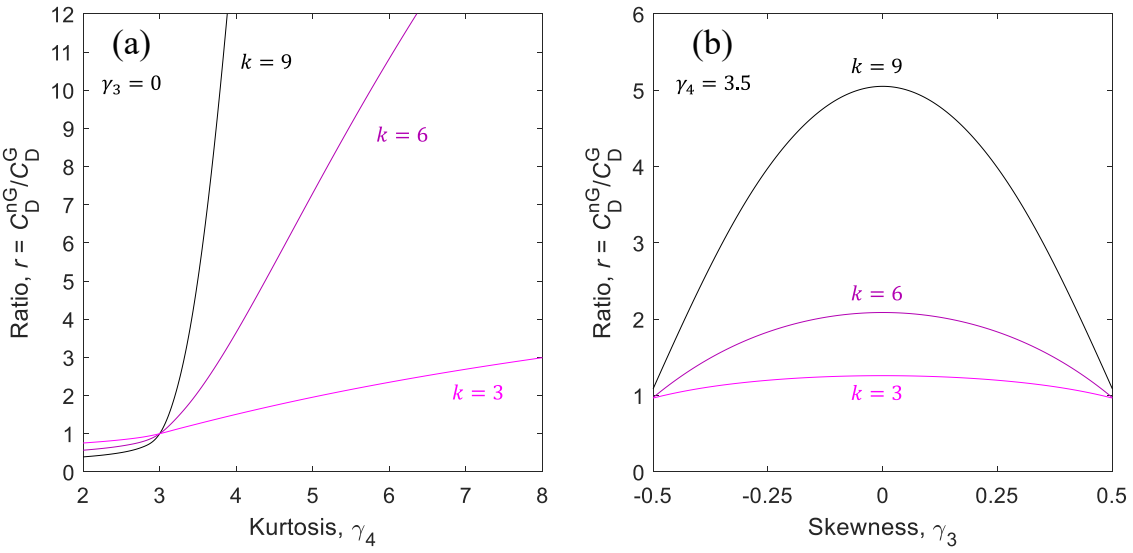

Figure 5.5. Ratio of coefficient of variation of damage $r = (C_D)^{nG}_{Mad}/(C_D)^{G}_{Mad}$ versus (a) kurtosis coefficient and (b) skewness coefficient, for several values of the inverse slope k of the S-N curve.

Figure 5.5(a) considers a set of non-Gaussian processes with same skewness $\gamma_3 = 0$, but different values of kurtosis γ_4 and inverse slope k. Compared to the Gaussian case, the CoV of a non-Gaussian process is shown always to decrease ($r < 1$) or increase ($r > 1$) depending on whether the process is platykurtic ($\gamma_4 < 3$) or leptokurtic ($\gamma_4 > 3$). For a given γ_4, the variation depends on k.

In the region $\gamma_4 < 3$, the decrease of CoV becomes larger for high k values. For $\gamma_4 = 2$, the CoV diminishes up to 60% for $k = 9$. In the region $\gamma_4 > 3$ the CoV has an opposite trend, but k has a more pronounced effect, especially when $k > 3$. For example, for $k = 6$ the increase arrives at 120% for $\gamma_4 = 6.3$, whereas for $k = 9$ the same increase is attained already for γ_4 slightly below 4.

Figure 5.5(b) shows, instead, the effect of skewness γ_3 on the CoV of damage of "asymmetric" random processes. The kurtosis is set to $\gamma_4 = 3.5$; it is indeed not possible to choose a lower value if, in the Winterstein's model, the skewness has to reach the limits -0.5 to +0.5. Similar trends are obtained for other γ_4 values.

For any given k, the curves in Figure 5.5(b) are symmetric, which is yet not surprising. In fact, in the Winterstein's model, the transformation $G(-)$ corresponding to equal and opposite values $+\gamma_3$ and $-\gamma_3$ turns out to be "mirrored" with respect to the straight line of the Gaussian case. In symbols: $G_{\gamma_3>0}(X) = -G_{\gamma_3<0}(-X)$. Skewness values other than zero only make the mean stress of each non-Gaussian cycle, $(z_\mathrm{p} + z_\mathrm{v})/2$, be different from zero, whereas stress amplitudes remain unchanged and follow the same probability distribution in both cases $+\gamma_3$ and $-\gamma_3$.

The results in Figure 5.5(b) reveals that for a given γ_4, the largest increment of CoV occurs for $\gamma_3 = 0$; lower increments are observed for either positive or negative skewness values. As before, the higher the inverse slope k, the higher the increment, although now the effect is less marked than what observed for the kurtosis. In any case, these results confirm once more the importance of considering non-Gaussian effects in the evaluation of the variance of damage.

Chapter 6

TEST OF STATIONARITY OF RANDOM LOADING

6.1 INTRODUCTION

Chapter 5 presented two theoretical models for assessing the variance of fatigue damage in stationary non-Gaussian random processes. The non-Gaussian models extend two methods existing in the literature (Madsen et al., Low) that are valid for narrow-band Gaussian processes. Monte Carlo numerical simulations in the time-domain approach were used to verify the correctness of the two models proposed and to identify typical trends. The statistics (e.g. coefficient of variation) characterizing the sample of damage values were compared to theoretical estimations. A perfect match was observed.

A common situation is, however, the uncertainty of damage computed from a few measured time-histories of finite time length T. In this situation, all theoretical approaches in Chapter 4 and 5 cannot be applied because they require the knowledge of the exact autocorrelation function or PSD, where "exact" stands for the value averaged from an infinite ensemble of stationary time-histories. It would be much easier to construct a confidence interval enclosing the expected damage. This approach based on a direct analysis of stationary time-history would impose no restrictions on the specific type of PSD, as required by theoretical approaches in Chapter 4 and 5. However, not only the analytical methods in Chapter 4 and 5 but also the confidence interval for the expected

damage — which will be addressed in Chapter 7 — are only applicable to stationary random loading.

Structures and mechanical components under stationary loading have statistical properties (e.g. variance, mean value and frequency content) that do not change over time. Since this hypothesis is not valid for all structures and mechanical components, a non-parametric statistic method should be used to verify the stationarity of measured random time-histories. For example, measured stress responses may be non-stationary, as those resulting from different wind conditions, various sea states, as well as road sequences with different surface profile characteristics. To identify the non-stationarity of an excitation, Rouillard [ROU14] adopted the non-parametric run test method to obtain the non-stationarity level of a vehicle's vibrations. Rouillard's approach considers root-mean-squared (RMS) values as the statistical parameter, which can detect change only in the variance and mean value of random time-history $x(t)$. It would be more effective to consider the damage computed for each block as the statistical parameter, which takes into account change in the variance, mean value, and frequency content of a random time-history $x(t)$.

This chapter introduces a run test approach to verify the stationarity of time-histories $x(t)$ with duration T. As an alternative to Rouillard's approach that takes into account RMS values, the proposed run test considers the damage values computed for each independent block as the statistical parameters. The proposed damage-based run test is then compared with Rouillard's using stationary and non-stationary simulation time-histories $x(t)$.

6.2 THE RUN TEST METHOD

The Wald–Wolfowitz run test or simple run test is a non-parametric method to verify the stationarity of a random loading [WAL40,BRO65,BEN86]. This method is based on the idea of dividing a time-history $x(t)$ into N_B blocks. The run test considers a sequence of non-overlapping blocks. For each block, a value is calculated for the statistical parameter under investigation. This sequence of observations or observed block values define a run r that is followed and preceded by a different observation or no observation at all [BEN86]. One simple example would be a sequence of observed block values H and T, which are measured randomly one at a time. The sequence of H and T might be:

HH TTT HHH (6.1)

providing $r = 3$ runs, i.e. the sequence of two H and one T, represented by $N_\mathrm{B} = 8$ blocks. The run test considers that the probability of H or T does not change from one observation to the other. Precisely, the sequence of observations consists in independent observations of the same random variable [BEN86].

The sampling distribution of runs is a random variable r with a mean μ_r and variance σ_r^2, as follows [BEN86]:

$$\mu_\mathrm{r} = 1 + \frac{2n_\mathrm{H}n_\mathrm{T}}{n_\mathrm{H} + n_\mathrm{T}}, \qquad \sigma_\mathrm{r}^2 = \frac{2n_\mathrm{H}n_\mathrm{T}\,(2n_\mathrm{H}n_\mathrm{T} - n_\mathrm{H} - n_\mathrm{T})}{(n_\mathrm{H}+n_\mathrm{T})^2\,(n_\mathrm{H} + n_\mathrm{T} - 1)} \tag{6.2}$$

where n_H and n_T are the number of observed blocks H and T, respectively.

Eq. (6.2) can be adapted by the classification of observations as being above n_a or below n_b the sample median [BRO65,BEN86]. If the number of observations N_B is odd, the method ignores the observation value that falls into the median. In this case, the number of observations above the median n_a equals the number of observations below the median n_b; so $n_\mathrm{a} = n_\mathrm{b}$. Eq. (6.2) can then be simplified as [BRO65,BEN86]:

$$\mu_\mathrm{r} = 1 + n_\mathrm{a}, \qquad \sigma_\mathrm{r}^2 = \frac{n_\mathrm{a}(n_\mathrm{a} - 1)}{2n_\mathrm{a} - 1} \tag{6.3}$$

In statistics, the number of runs r is also a parameter of a particular random time-history $x(t)$ that might be tested by a hypothesis testing. In fact, it refers to a statistical procedure used to accept or reject hypothesis.

Based on the hypothesis that the observed blocks are independent and identically distributed from any continuous distribution [BRO65,BEN86], the acceptance interval for this hypothesis is:

$$r_{\mathrm{n_a},1-\beta/2} < r \leq r_{\mathrm{n_a},\beta/2} \tag{6.4}$$

where $100(1-\beta)\%$ is the level of significance, and $r_{\mathrm{n_a},1-\beta/2}$ is the lower and $r_{\mathrm{n_a},\beta/2}$ the upper limit of the run test. These limit values are determined by μ_r and σ_r^2 in Eq. (6.3) or using a tabulation of run distribution [BEN86]. The number of runs r counted in a time-history $x(t)$ plays an important role to verify the stationarity. Indeed, if the number of runs r falls into the acceptance interval, the random time-history $x(t)$ is presumably stationary. Otherwise, $x(t)$ is classified as non-stationary.

Furthermore, this hypothesis test based on a sequence observed blocks is very powerful for detecting fluctuating trends [BEN86], for instance, increases and decreases in variance, mean and frequency content of a random time-history $x(t)$ over time. These non-stationary random loadings often encountered in many applications are characterized as a sequence of stationary load states. Examples of non-stationary loadings with changes

in the mean value are the stresses in trucks switching between loaded and unloaded service conditions and loadings observed on aircraft wings during ground–air–ground maneuvers [JOH95,JOH98,BUC97]. An example of non-stationary loadings with different variance levels is the vertical front suspension loads of a vehicle moving on different road surface conditions (e.g. asphalt, gravel, cobblestone) [NIK01]. Last, but not least, a mountain-bike traveling on a track by means of various speeds is an example of non-stationary loadings with changes in the frequency content [BEN05a,BEN07].

Rouillard studied the run test using the RMS computed for each block as the statistical parameter [ROU14]. Rouillard's approach classifies the observed block values $RMS_{\mathrm{B,i}}(T_{\mathrm{B}}), i = 1,2, \dots N_{\mathrm{B}}$ based on their mean. Depending upon the vibrations generated by road vehicles, Rouillard assumed that the frequency content of measured time-histories $x(t)$ remains constant over time. A run ratio or run test index is provided to indicate the non-stationary level of a time-history. Rouillard also addressed the effect of the block length T_{B}. A short block length increases the sensitivity of the analysis to local variations, while a wider length could not perceive the non-stationarity. As a final point, Rouillard highlighted a notable effect in quantifying stationarity in overlapping and non-overlapping consecutive blocks, i.e. not only independent but also dependent observed block values.

One possible limitation of the Rouillard's approach is using RMS as the statistical parameter, which detects change only in the variance and mean value of random time-history $x(t)$. It would be more effective if the damage $D_{\mathrm{B,i}}(T_{\mathrm{B}}), i = 1,2, \dots N_{\mathrm{B}}$ computed for each block is considered as the statistical parameter, since this allows taking into account change in the variance, mean value, and frequency content of random time-history $x(t)$. This argument will be investigated in the next section.

6.3 PROPOSED APPROACH: A DAMAGE-BASED RUN TEST

This section addresses the run test method by means of a different procedure than Rouillard's one [ROU14]. Rather than using his usual statistical parameters—e.g. $RMS_{\mathrm{B,i}}(T_{\mathrm{B}})$, $i = 1,2,\dots N_{\mathrm{B}}$ values—as the output calculated in each block, the damage $D_{\mathrm{B,i}}(T_{\mathrm{B}})$, $i = 1,2,\dots N_{\mathrm{B}}$ is computed for each independent block (without overlapping) (see Figure 1.1). For a random time-history $x(t)$ with a fixed time length T, the number of observed blocks N_{B} and the block length T_{B} are inversely proportional, $T_B = T/N_B$.

By analogy with the damage $D(T)$ of the entire time-history $x(t)$, the damage $D_{\mathrm{B}}(T_{\mathrm{B}})$ is calculated by summing up the damage of each half cycle during time T_{B}:

$$D_{\mathrm{B}}(T_{\mathrm{B}}) = \sum_{\mathrm{i}=0}^{\mathrm{n(T_B)}-1} d_{\mathrm{i}} = \sum_{\mathrm{i}=0}^{\mathrm{n(T_B)}-1} \frac{s_{\mathrm{i}}^{\mathrm{k}}}{2A} \tag{6.5}$$

where $n(T_{\mathrm{B}})$ is the number of half cycles in time interval T_B. The damage $D_{\mathrm{B}}(T_{\mathrm{B}})$ in Eq. (6.5) is computed in time domain by means of the rainflow counting method and the Palmgren-Miner rule. Note that $D_{\mathrm{B}}(T_{\mathrm{B}})$ of the proposed approach is used as a statistical parameter only, and not used for a fatigue damage assessment. In contrast to Rouillard's approach [ROU14], the damage-based run test here applied can detect not only changes in variance and mean value, but also changes in frequency content of the random time-history $x(t)$. The proposed approach classifies the observed block values $D_{\mathrm{B,i}}(T_{\mathrm{B}})$, $i = 1,2,\dots N_{\mathrm{B}}$ as being above n_{a} or below n_{b} the sample median. As a consequence of classifying above or below median, the damage-based run test (non-parametric method) assumes continuity in the distribution but makes no assumptions about the form of the distribution [BRO65,BEN86].

For the number of blocks N_{B} and block length T_{B} of the proposed run test, parameters from a similar technique of dividing a time-history, i.e. Short-Time Fourier Transform (STFT), are considered. This technique is widely used to analyze how the frequency content of a time-history $x(t)$ changes over time. The procedure for computing

STFT is to divide the time-history $x(t)$ into N_B blocks of equal length T_B and then compute the Fourier transform of each one. The number of blocks N_B and their duration T_B have an indispensable influence on the time and the frequency resolution. Unfortunately, high resolutions cannot be achieved in both domains because they are inversely proportional for a time-history $x(t)$ with a fixed time length T. These resolutions can be controlled using two parameters such as statistical (or random) error $\varepsilon_\mathrm{r} = 1/\sqrt{N_\mathrm{B}}$ and frequency resolution $\Delta f = 1/T_\mathrm{B}$, see [BEN10c,WIR95]. The combination with the threshold of $\varepsilon_\mathrm{r} \geq 0.2$ and $\Delta f \geq 0.1$ is recommended here towards the best compromise among time- and frequency-domain resolution. Finally, the number of blocks N_B and block length T_B of the proposed damage-based run test are then established following such threshold parameters.

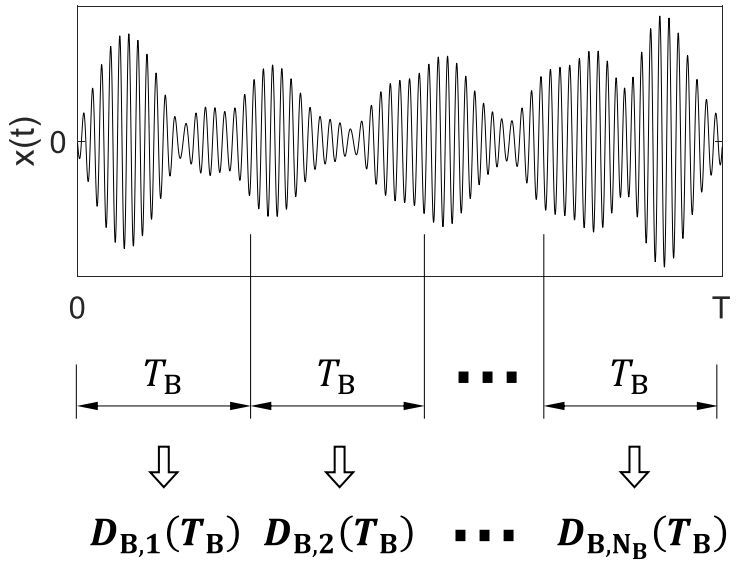

Figure 6.1. A random time-history $x(t)$ divided into N_B independent blocks of equal length T_B. The damage values $D_{\mathrm{B,i}}(T_\mathrm{B})$, $i = 1,2, \ldots N_\mathrm{B}$ of each block are highlighted in bold.

6.4 NUMERICAL SIMULATIONS

This section explores the proposed damage-based run test and the Rouillard's one through the use of simulated random time-histories. As a first numerical example, two stationary adjacent segments were simulated separately using the same idealized narrow-band rectangular spectrum $S_{\mathrm{X}}(f)$ centered at $f_{\mathrm{c}} = 10$ Hz, with half spectral width $b = 1$ Hz, and normalized to $\lambda_0 = 1$ (see Chapter 4). The variance ratio between the second and the first segment was alternated in the values $\sigma_{\mathrm{x},2}^2/\sigma_{\mathrm{x},1}^2 = 1, 1.25, 1.5, 1.75, 2$. By increasing $\sigma_{\mathrm{x},2}^2/\sigma_{\mathrm{x},1}^2$, the entire random time-history $x(t)$ changes from stationary with $\sigma_{\mathrm{x},2}^2/\sigma_{\mathrm{x},1}^2 = 1$ to non-stationary with $\sigma_{\mathrm{x},2}^2/\sigma_{\mathrm{x},1}^2 > 1$ since all other properties were kept constant over time (e.g. mean and frequency content). To form each random time-history $x(t)$, the first and second segments with same relative time length were combined together, for example, Figure 6.3(a). A total of $N = 100$ Gaussian random time-histories $x_{\mathrm{i}}(t)$, $i = 1,2,3, \ldots N$ with time length T are obtained for each variance ratio $\sigma_{\mathrm{x},2}^2/\sigma_{\mathrm{x},1}^2$.

The run test using proposed and Rouillard's approach were applied to stationary and non-stationary time-histories with fixed total time length $T = 300$ s, statistical error $\varepsilon_{\mathrm{r}} = 0.183$ and frequency resolution $\Delta f = 0.1$. As a consequence, each simulated time-history $x_{\mathrm{i}}(t)$ were divided into $N_{\mathrm{B}} = 30$ blocks with same block length $T_{\mathrm{B}} = 10$ s. In all subsequent studies examined, the proposed and Rouillard's run test assume time-histories with $T = 300$ s, $N_{\mathrm{B}} = 30$ and $T_{\mathrm{B}} = 10$ s. Also, the damage $D_{\mathrm{B,i}}(T_{\mathrm{B}})$, $i = 1,2, \ldots N_{\mathrm{B}}$ of the proposed run test was computed for each block using $k = 1$ and $C = 1$.

The first numerical example allows the sensibility of proposed and Rouillard's approach in detecting stationary and non-stationary time-histories to be verified. This sensibility analysis is demonstrated in Figure 6.2 by means of number of runs r counted in each time-history, as a function of variance ratio $\sigma_{\mathrm{x},2}^2/\sigma_{\mathrm{x},1}^2$. As mentioned in the Section 6.2, a time-history is classified as stationary if the number of runs r falls into the acceptance interval. Otherwise, the time-history is non-stationary. The acceptance interval of the first numerical example is highlighted on the right side of Figure 6.2. The

lower $r_{15,0.975} = 10$ and upper $r_{15,0.025} = 21$ limit values of the acceptance interval were obtained in the tabulation in [BEN86]. They are identical for both run test methods and all ratio $\sigma_{x,2}^2/\sigma_{x,1}^2$ caused by same observations above or below the median or mean and 95% level of significance.

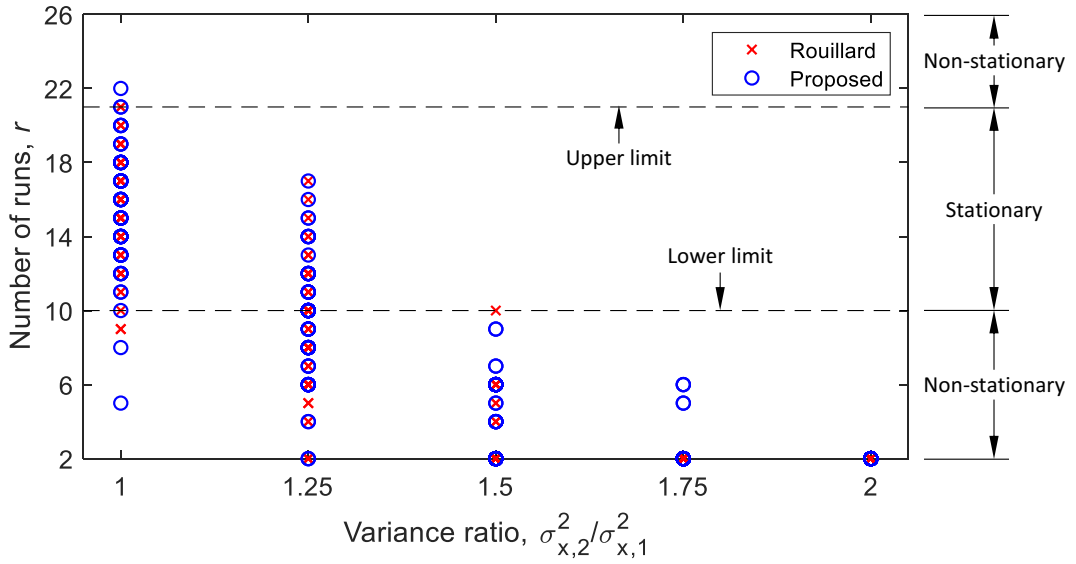

Figure 6.2. Sensibility analysis of proposed and Rouillard's approach by varying the ratio $\sigma_{x,2}^2/\sigma_{x,1}^2$.

It may be observed that few numbers of runs r counted in each simulated time-history with $\sigma_{x,2}^2/\sigma_{x,1}^2 = 1$ fall outside (non-stationary) acceptance interval, while the others inside (stationary). It is acceptable because the interpretation of a 95% level of significance is that 5 out of 100 simulations would be classified as non-stationary. Of more interest here is the sensibility of both run test methods in detecting non-stationary time-histories. In such cases, most numbers of runs r counted in each simulation should fall outside the acceptance interval and consequently time-histories would be classified as non-stationary. However, approximately 50 up to 100 numbers of runs r of time-histories with $\sigma_{x,2}^2/\sigma_{x,1}^2 = 1.25$ fall inside the interval for both methods, which highlights

the sensibility of proposed and Rouillard's run test applied to time-histories carrying small changes of variance.

In this example, the variance between first and second segment $\sigma_{x,2}^2/\sigma_{x,1}^2$ was varied to check the correctness of proposed and Rouillard's run test applied to simulated stationary and non-stationary time-histories. In practice such hypotheses, i.e. stationary and non-stationary, are not known in advance. This suggests that the number of runs r of a measured time-history from a real application could fall inside (stationary) the acceptance interval if changes of the variance levels were small. However, assuming the hypothesis of stationary in this situation might be sufficient for an accurate damage assessment [BEN05a,BEN07].

Similar numerical examples also explores the proposed damage-based run test and the Rouillard's one by a stationary time-history (Case A) and non-stationary time-histories with different variance $\sigma_{x,2}^2/\sigma_{x,1}^2$ (Case B), mean $\mu_{x,2}/\mu_{x,1}$ (Case C) and frequency content ratio $f_{c,2}/f_{c,1}$ (Case D) during time T. The properties for each simulated time-history are:

- Case A with $\sigma_{x,2}^2/\sigma_{x,1}^2 = 1$, $\mu_{x,2}/\mu_{x,1} = 1$ and $f_{c,2}/f_{c,1} = 1$, see Figure 6.3(a);
- Case B with $\sigma_{x,2}^2/\sigma_{x,1}^2 = 3$, $\mu_{x,2}/\mu_{x,1} = 1$ and $f_{c,2}/f_{c,1} = 1$, see Figure 6.3(b);
- Case C with $\sigma_{x,2}^2/\sigma_{x,1}^2 = 1$, $\mu_{x,2}/\mu_{x,1} = 3$ and $f_{c,2}/f_{c,1} = 1$, see Figure 6.3(c);
- Case D with $\sigma_{x,2}^2/\sigma_{x,1}^2 = 1$, $\mu_{x,2}/\mu_{x,1} = 1$ and $f_{c,2}/f_{c,1} = 3$, see Figure 6.3(d);

The four random time-histories in Figure 6.3 were obtained using the previously procedure of simulating two stationary adjacent segments to define the properties listed above. The high ratio of variance in Case B, mean in Case C and frequency content in Case D were chosen as they properly characterize non-stationary random time-histories.

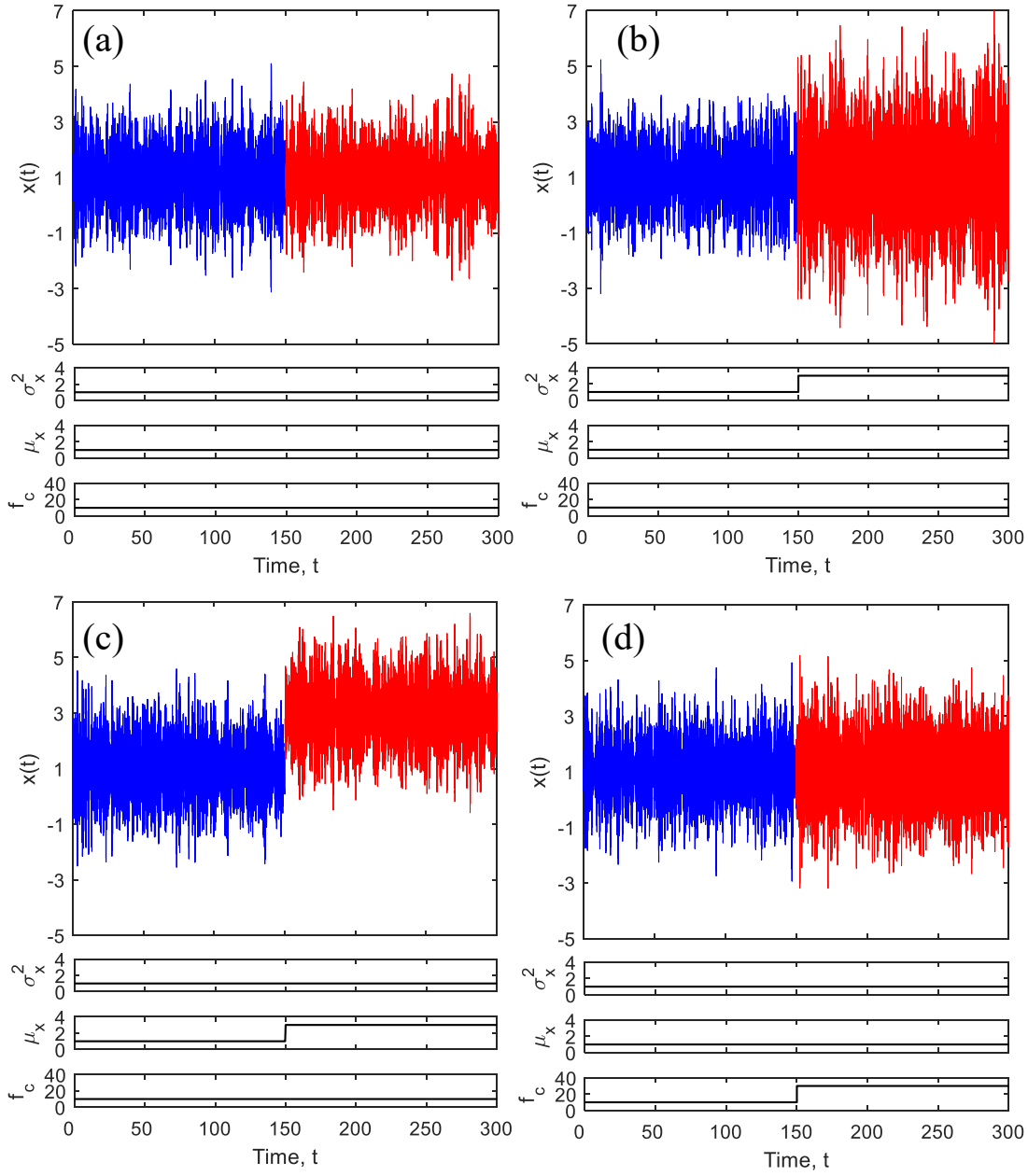

Figure 6.3. Simulated random time-histories $x(t)$: (a) stationary in Case A; (b) non-stationary in Case B; (c) non-stationary in Case C; (d) non-stationary in Case D.

6.4.1 Stationary time-history

The stationary time-history of Case A was first considered to evaluate the proposed damage-based run test and Rouillard's one. The proposed run test is presented in Figure 6.4(a) by damage values $D_{\mathrm{B,i}}(T_{\mathrm{B}})$ (normalized to the median) classified according to their median. Instead, Figure 6.4(b) displays Rouillard's approach using $RMS_{\mathrm{B,i}}(T_{\mathrm{B}})$ as the values calculated in each block. $RMS_{\mathrm{B,i}}(T_{\mathrm{B}})$ values are classified according to their mean.

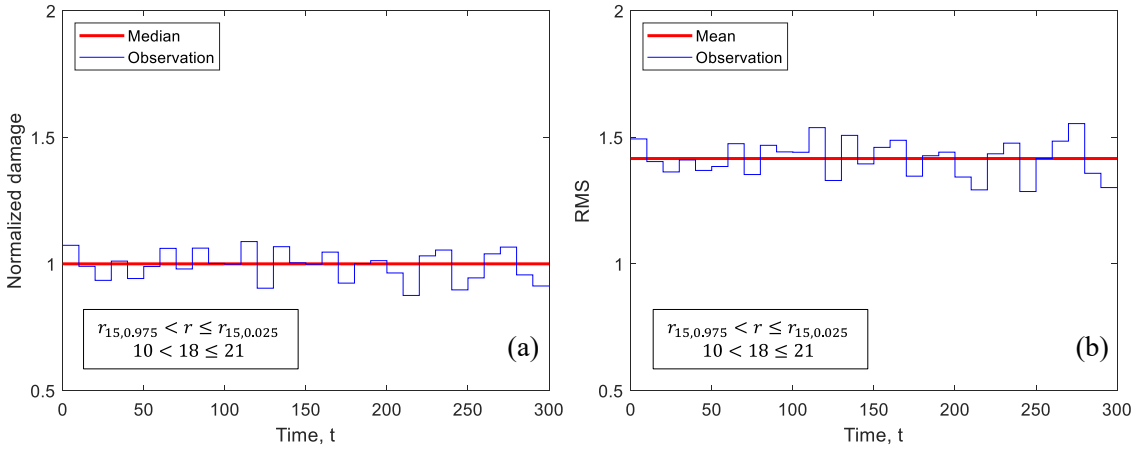

Figure 6.4. Run test method using the (a) proposed approach and (b) Rouillard's approach applied to a simulated stationary random time-history.

Figure 6.4(a) and Figure 6.4(b) provide $r = 18$ runs from a sequence of $N_{\mathrm{B}} = 30$ observations. Similar trends of block values $D_{\mathrm{B,i}}(T_{\mathrm{B}})$ and $RMS_{\mathrm{B,i}}(T_{\mathrm{B}})$ over time were obtained in the proposed approach and in Rouillard's one. However, the proposed run test in Figure 6.4(a) indicates a greater difference over time on observed block values compared to Rouillard's approach in Figure 6.4(b). In both methods, the lower $r_{15,0.975} = 10$ and upper $r_{15,0.025} = 21$ limit values of the acceptance interval were obtained in the tabulation in [BEN86] as well as all subsequent results. Accordingly, the proposed and Rouillard's run test resulted in $10 < 18 \leq 21$ considering a 95% level of significance.

The number of runs r falls inside the interval, attesting the correctness of both run test approaches at least when applied to the simulated stationary time-history of this study.

6.4.2 Non-stationary time-histories

The non-stationary time-histories of Case B, C and D are now examined by the proposed and Rouillard's run test. As a first result, Figure 6.5 displays both run test approaches applied to the time-history $x(t)$ of Case B. Note that the observed block values $D_{\mathrm{B,i}}(T_{\mathrm{B}})$ (normalized to the median) and $RMS_{\mathrm{B,i}}(T_{\mathrm{B}})$ underlined a significant difference between the second and the first segment. The proposed run test appears to be consistent with Rouillard's approach when applied to non-stationary time-history $x(t)$ of Case B with $\sigma_{\mathrm{x},2}^2/\sigma_{\mathrm{x},1}^2 = 3$. In fact, it was evidenced by the identical lower and upper limit values of the acceptance interval and the number of runs r. Those values are listed in the fifth, sixth and seventh columns of Table 4.1 in line with ratio $\sigma_{\mathrm{x},2}^2/\sigma_{\mathrm{x},1}^2 = 3$. Therefore, both methods tested a particular simulated time-history $x(t)$ of Case B as non-stationary.

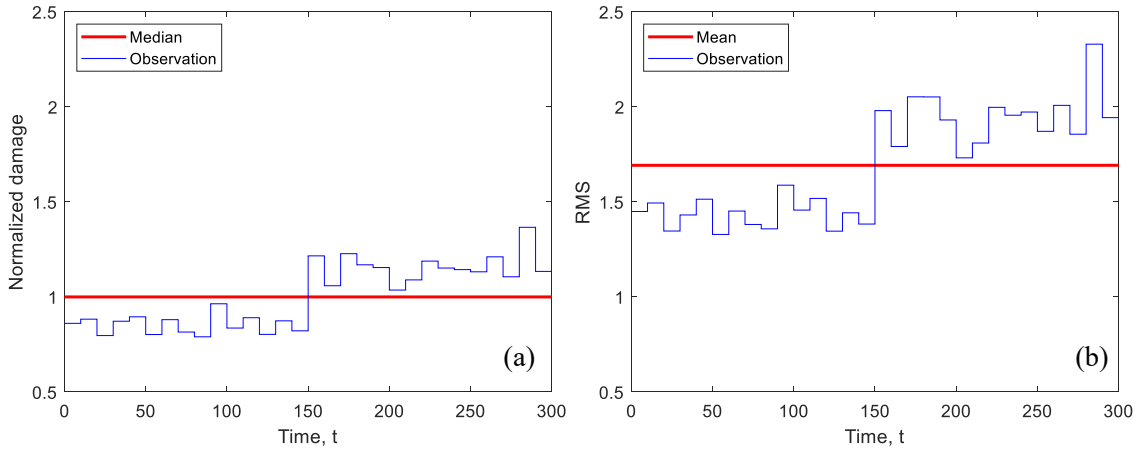

Figure 6.5. Run test method using the (a) proposed approach and (b) Rouillard's one applied to non-stationary time-history of Case B with ratio $\sigma_{\mathrm{x},2}^2/\sigma_{\mathrm{x},1}^2 = 3$.

Table 6.1. Results of the damage-based and Rouillard's run test according to each non-stationary case

Method	Case	$\sigma_{x,2}^2/\sigma_{x,1}^2$	$\mu_{x,2}/\mu_{x,1}$	$f_{c,2}/f_{c,1}$	$r_{15,0.975}$	r	$r_{15,0.025}$	Testing $r_{15,0.975} < r \leq r_{15,0.025}$
Damage-based run test	B	3	1	1	10	2	21	non-stationary
	C	1	3	1	10	2	21	non-stationary
	D	1	1	3	10	2	21	non-stationary
Rouillard's run test	B	3	1	1	10	2	21	non-stationary
	C	1	3	1	10	2	21	non-stationary
	D	1	1	3	10	14	21	stationary

The non-stationary time-history $x(t)$ of Case C was investigated by the proposed run test in Figure 6.6(a) and by Rouillard's one in Figure 6.6(b). Seeing such figures, $r = 2$ runs are easily counted along with time. Similar trends between both run test methods are observed by $D_{B,i}(T_B)$ and $RMS_{B,i}(T_B)$ values that cross their median or mean value only once. By limits $r_{15,0.975} = 10$ and $r_{15,0.025} = 21$, proposed and Rouillard's approach rejected the hypothesis testing and the specific simulated time-history $x(t)$ of Case C with ratio $\mu_{x,2}/\mu_{x,1} = 3$ is assumed to be non-stationary.

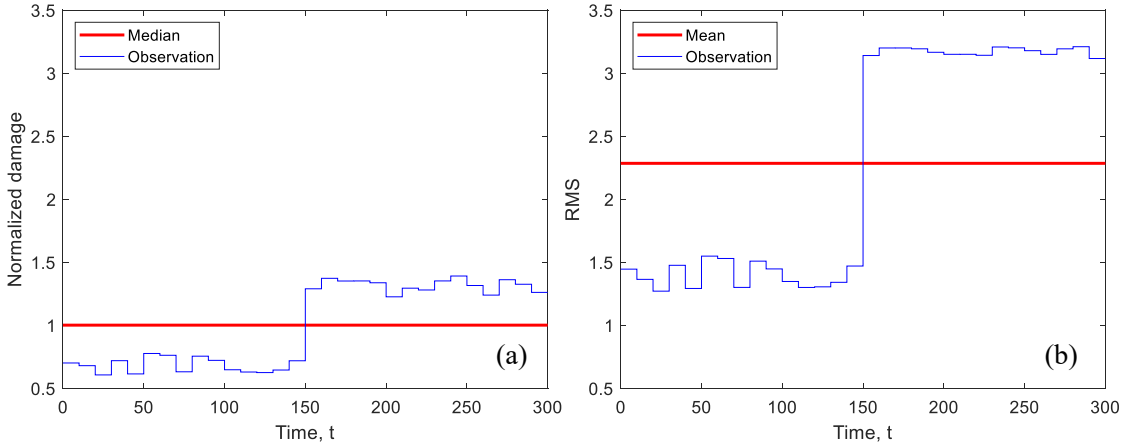

Figure 6.6. Run test method using the (a) proposed approach and (b) Rouillard's one applied to non-stationary time-history of Case C with ratio $\mu_{x,2}/\mu_{x,1} = 3$.

Figure 6.7 considers the two methods applied to non-stationary time-history $x(t)$ of Case D with ratio $f_{c,2}/f_{c,1} = 3$. Similarly to previous results, Figure 6.7(a) shows a pronounced change in the damage $D_{B,i}(T_B)$ values (normalized to the median) over time. By contrast, in Rouillard's approach, $RMS_{B,i}(T_B)$ values exhibited small variations (Figure 6.7(b)), which is not surprising: Rouillard considers only changes in the RMS values along with time [ROU14]. Therefore, the hypothesis of the proposed approach was rejected (non-stationary), given that $r = 2$ did not fall into the acceptance interval, and Rouillard's approach led to $r = 14$ runs, which is accepted (stationary). Table 4.1 summarized all results of both damage-based and Rouillard's run test applied to non-stationary time-histories.

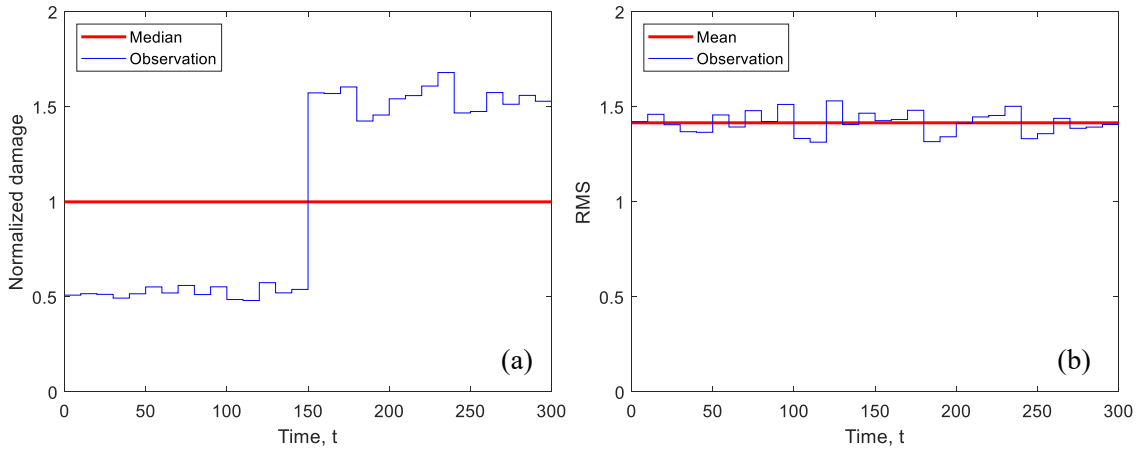

Figure 6.7. Run test method using the (a) proposed approach and (b) Rouillard's one applied to non-stationary time-history of Case D with the ratio $f_{c,2}/f_{c,1} = 3$.

Chapter 7

VARIABILITY OF FATIGUE DAMAGE: A REAL-WORLD SCENARIO

7.1 INTRODUCTION

Fatigue damage is often calculated by a time-domain approach (rainflow counting method and Palmgren-Miner rule). The time-domain damage may be calculated using one measured random time-history record, which must be considered one sample value out of an infinite ensemble. If it is computed based on another measured time-history with the same duration and statistical properties, the damage may change slightly. Damage values are usually not identical due to the sampling variability. As said in Chapter 6, all theoretical approaches in Chapter 4 and 5 cannot be applied in this situation as they require the knowledge of an infinite ensemble of stationary time-histories.

This chapter addresses the issue of estimating the statistical variability of fatigue damage when it is computed either using a few stationary time-histories (Case 1) or only one (Case 2). In each case, confidence interval expressions were derived to enclose the (unknown) expected fatigue damage. An example demonstrated the correctness of both confidence interval expressions. The example considered the stress power spectral density in an offshore platform, as proposed by [WIR76]. By replicating the analysis a large number of times and counting how many times the confidence interval encloses the expected damage, the analysis emphasized the validity of the proposed approach.

The confidence intervals for the expected damage were also investigated by measuring the random loads acting on a Mountain-bike. To calculate the confidence intervals and the expected damage, several time-histories were measured directly in the Mountain-bike in a typical north Italian off-road track. The stationarity hypothesis of all measured time-history records was also verified by quantitative approaches, i.e. comparison of loading (or cumulative) spectra and Short-Time Fourier Transform (STFT). Besides, the run test method using the proposed approach in Chapter 6 was considered to quantify the stationarity of all measured time-history records. The proposed run test considers the damage values computed for each independent block as the statistical parameters (see Chapter 6). This procedure can detect changes in the variance, mean, and frequency content of time-histories $x(t)$. A sort of calibrator damage was also used to estimate the unknown expected damage; it is the sample mean of several damage values, where each value was computed using a different measured time-history. The calibrator sample damage is needed to check whether the confidence intervals correctly encloses the expected damage.

7.2 CONFIDENCE INTERVAL OF FATIGUE DAMAGE WITH ONE OR MORE TIME-HISTORIES

The confidence interval will be obtained in this section for two different cases in accordance with the number of time-histories available (see Figure 1.1): “Case 1” refers to two or more time-histories $x_{\mathrm{i}}(t)$, $i = 1,2, \dots N$ $(N \geq 2)$ of same duration T, “Case 2” refers to only one time-history $(N = 1)$ with the same duration T like in Case 1. Symbol $D_{\mathrm{i}}(T)$, $i = 1,2, \dots N$ identifies the fatigue damage of each time-history, computed in the time-domain (rainflow counting and Palmgren-Miner rule). The approach proposed for Case 1 is particularly appropriate for a small sample size N, as it occurs in practice.

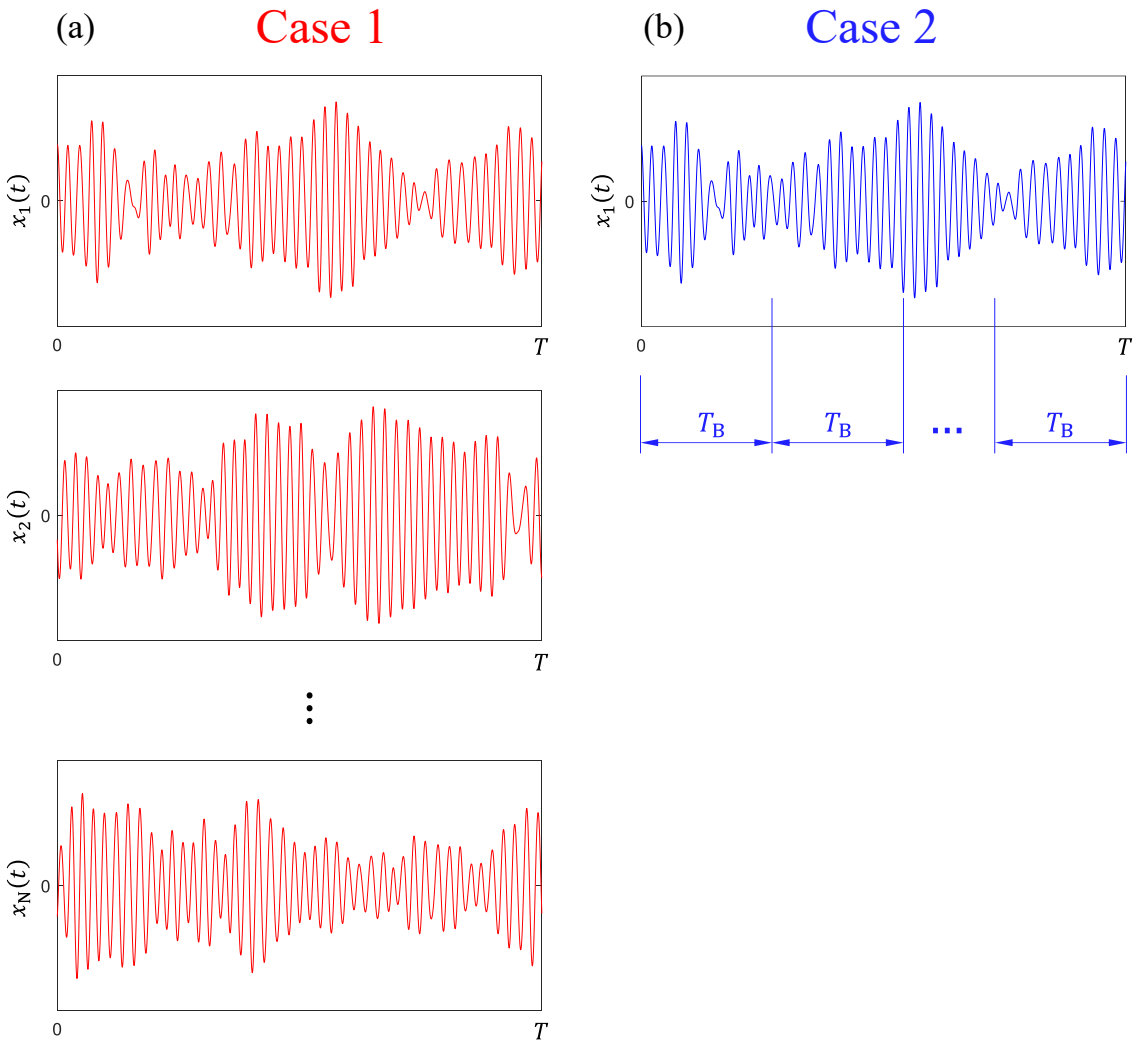

Figure 7.1. Two cases analyzed: (a) Case 1: two or more time-histories are available (the figure shows an example with N time-histories); (b) Case 1: only one time-history is available.

Case 1 is addressed first. Consider that N time-histories $x_i(t)$ are available; see Figure 1.1(a). The sample mean $\overline{D}(T)$ and the sample variance $\hat{\sigma}_D^2$ of the damage, whose values are the estimates of the exact (but unknown) quantities $E[D(T)]$ and σ_D^2, are both first computed from the set of N damage values $D_i(T)$. Following the definition of the confidence interval of a normally distributed random variable with unknown mean and

unknown variance, the $100(1-\beta)\%$ confidence interval for the expected damage is defined as [MON14]:

$$\overline{D}(T) - \frac{t_{\mathrm{dof},\beta/2} \cdot \hat{\sigma}_{\mathrm{D}}}{\sqrt{N}} \leq E[D(T)] \leq \overline{D}(T) + \frac{t_{\mathrm{dof},\beta/2} \cdot \hat{\sigma}_{\mathrm{D}}}{\sqrt{N}} \tag{7.1}$$

where $t_{\mathrm{dof},\beta/2}$ is the quantile of the Student's t-distribution with $dof = N - 1$ degrees of freedom. Equation (6.2) exploits the fact that $t_{\mathrm{dof},1-\beta/2} = -t_{\mathrm{dof},\beta/2}$. Therefore, for $dof = 9$ and $100(1-\beta)\% = 95\%$, for example, it is $t_{9,0.025} = 2.262$, showing that, as N increases, the confidence interval width becomes narrower. In this case, the Student's t-distribution approaches the standard normal distribution. In the hypothetical limit situation in which N tends to infinity, there is no statistical uncertainty, and the confidence interval converges towards $E[D(T)]$.

Case 2 is a particular case of Case 1 with $N = 1$. Since only one single time-history $x(t)$ is available, a slightly distinct procedure is proposed to construct the confidence interval, in which the sample mean and the sample variance of the damage cannot be computed as done before. The main principle is to divide the time-history into N_B separate blocks of equal length, a type of block subdivision also adopted, although for different purposes, in [COS18], $T_{\mathrm{B}} = T/N_{\mathrm{B}}$; see Figure 1.1(b). For a fixed total duration T, the quantities N_{B} and T_{B} are inversely proportional.

After the block subdivision, the damage of the entire time-history $x(t)$ can be calculated by summing up the damage of all blocks:

$$D(T) \cong \sum_{\mathrm{i}=1}^{\mathrm{N_B}} D_{\mathrm{B,i}}(T_\mathrm{B}) = N_\mathrm{B} \cdot \overline{D}_\mathrm{B}(T_\mathrm{B}) \tag{7.2}$$

where N_B is the number of blocks, $D_{\mathrm{B,i}}(T_\mathrm{B})$, $i = 1,2, \dots N_\mathrm{B}$ is the damage of each block and $\overline{D}_\mathrm{B}(T_\mathrm{B}) = N_\mathrm{B}^{-1} \sum_{\mathrm{i}=1}^{\mathrm{N_B}} D_{\mathrm{B,i}}(T_\mathrm{B})$ represents the sample mean of the damage values of all blocks. A minimum number of blocks $N_\mathrm{B} \geq 2$ is required.

It is worth paying particular attention that the first equality in Eq. (7.2) is not exact. Some fatigue cycles could be lost considering that the separation into blocks discontinues the time-history at those points connecting two adjacent blocks. The block subdivision eliminates all the cycles formed by those peaks and valleys in different blocks. It may be presumed that this effect is less noticeable in a narrow-band process in which fatigue cycles are formed by the two nearest peak and valley. Consequently, in theory, the sum of block damage values, as in Eq. (7.2), would be slightly smaller than the damage of the whole continuous time-history [COS18]. However, this difference is negligible if the number of cycles in each block is much greater than the number of blocks. For example, each block should have a minimum length T_B to contain approximately 10^3 cycles, which is about the lower bound of high-cycle fatigue applications. In other words, N_B cannot increase indefinitely. The block subdivision's negligible effect on the number of lost cycles will be confirmed by the simulation results presented in later figures.

The damage values $D_{\mathrm{B,i}}(T_\mathrm{B})$ have in common also the same variance. As the entire $x(t)$ is stationary, every time-history $x_\mathrm{i}(t)$ in each block has the same statistical properties of $x(t)$. Since all blocks also have the same length, the damages $D_{\mathrm{B,i}}(T_\mathrm{B})$ form a set of random variables that follow the same probability distribution, with expected value $E[D_\mathrm{B}(T_\mathrm{B})]$ and variance $\sigma^2_{\mathrm{D_B}}$. Furthermore, as the blocks are disjoint (not overlapped), the random variables $D_{\mathrm{B,i}}(T_\mathrm{B})$ are also independent.

Assuming that the damage values of each block, $D_{\mathrm{B,i}}(T_\mathrm{B})$, are independent and identically distributed, the variance σ_D^2 of the damage of the whole time-history $x(t)$ can be written as:

$$\sigma_\mathrm{D}^2 = \mathrm{Var}\left[\sum_{\mathrm{i}=1}^{\mathrm{N_B}} D_{\mathrm{B,i}}(T_\mathrm{B})\right] = N_\mathrm{B} \cdot \sigma_{\mathrm{D_B}}^2 \tag{7.3}$$

where $\sigma_{\mathrm{D_B}}^2 = \mathrm{Var}\big(D_{\mathrm{B,i}}(T_\mathrm{B})\big)$ is the variance common to all blocks. Moreover, given that the variance σ_D^2 must remain constant, the quantities $\sigma_{\mathrm{D_B}}^2$ and N_B are inversely proportional, i.e., the shorter is the block length T_B, the higher the variance of the damage in each block.

The relationship in Eq. (7.3) involves the "true" (but unknown) variances; it can, however, be approximated as $\sigma_\mathrm{D}^2 \cong N_\mathrm{B} \cdot \hat{\sigma}_{\mathrm{D_B}}^2$, in which the block variance is replaced by its sample estimate $\hat{\sigma}_{\mathrm{D_B}}^2 = (N_\mathrm{B} - 1)^{-1} \sum_{\mathrm{i}=1}^{\mathrm{N_B}} \big[D_{\mathrm{B,i}}(T_\mathrm{B}) - \overline{D}_\mathrm{B}(T_\mathrm{B})\big]^2$.

Separation into blocks then produces N_B damage values $D_{\mathrm{B,i}}(T_\mathrm{B})$ characterized by the sample mean $\overline{D}_\mathrm{B}(T_\mathrm{B})$ and the sample variance $\hat{\sigma}_{\mathrm{D_B}}^2$, the same situation as Case 1. Therefore, in the same way as Eq. (6.2), it is now possible to establish a confidence interval that encloses the expected damage of blocks, $E[D_\mathrm{B}(T_\mathrm{B})]$. By following the mathematical steps described in Appendix A, the final confidence interval expression for $E[D(T)]$ when considering only one time-history $x(t)$ is:

$$D(T) - t_{\mathrm{dof},\beta/2} \cdot \hat{\sigma}_\mathrm{D} \leq E[D(T)] \leq D(T) + t_{\mathrm{dof},\beta/2} \cdot \hat{\sigma}_\mathrm{D} \tag{7.4}$$

where $t_{\mathrm{dof},\beta/2}$ is the quantile of Student's t-distribution with $dof = N_\mathrm{B} - 1$ degrees of freedom, $D(T)$ is the fatigue damage of $x(t)$ and $\hat{\sigma}_\mathrm{D} \cong \sqrt{N_\mathrm{B}} \cdot \hat{\sigma}_{\mathrm{D_B}}$ the sample variance of the damage computed, respectively, from Eq. (7.2) and (7.3). Note that, although the

number of blocks does not appear directly in Eq. (7.4), it is used to compute $D(T)$ and $\hat{\sigma}_{\mathrm{D}}$.

For large dof, the Student's t-distribution approaches a standard normal distribution. Therefore, when the number of blocks becomes large (for example, >30), approximating $t_{\mathrm{dof},\beta/2}$ with $z_{\beta/2}$ introduces an error of only a few percent (more precisely, from 6% for $N_{\mathrm{B}} = 30$ down to 3% for $N_B = 30$), which is acceptable from an engineering standpoint.

The expression in Eq. (7.4) shows that, as N_{B} increases, the confidence interval width tends to become narrower because $t_{\mathrm{dof},\beta/2}$ diminishes towards the quantile $z_{\beta/2}$ of the standard normal variable. While for small N_{B} the difference is appreciable, for higher values (for example, for $N_{\mathrm{B}} = 25$), the two quantiles, as already said, only differ in a few percentage points. However, the number of blocks N_{B} cannot increase indefinitely, as it must ensure that the time-history in each block has a minimum number of fatigue cycles, as emphasized earlier.

However, there is a significant difference between Case 1 and Case 2. In Case 1, with many time-histories available, the statistical uncertainty reduces, although, given the challenge to collect a large number of time-histories; it may not always be practical. By contrast, the statistical uncertainty in Case 2 cannot be reduced by simply increasing the number of blocks; there is only one time-history available.

7.3 NUMERICAL EXAMPLE

This example aims to evaluate the correctness of the previous confidence interval expressions. It considers the Wirsching's formula of the output stress PSD in an offshore platform [WIR76] in simulations:

$$S_{\mathrm{X}}(f) = \frac{G H_{\mathrm{s}}^{\varphi} \exp\left[-\frac{1050}{(2\pi f T_{\mathrm{W}})^4}\right]}{T_{\mathrm{W}}^4 (2\pi f)^5 \left[\left(1 - \frac{f^2}{f_{\mathrm{n}}^2}\right)^2 + \left(\frac{2\zeta f}{f_{\mathrm{n}}}\right)^2\right]} \tag{7.5}$$

In this expression, G and φ are scaling factors, f_{n} = first resonance frequency (in Hz), H_{s} = significant wave height (in meters), and T_{W} = dominant wave period (in seconds). The shape of $S(f)$ changes from narrow-band to bimodal through a specific combination of H_{s} and T_{W}, characterizing each sea state. The parameter values φ, H_{s}, T_{W} depend on the sea state, whereas the others G, f_{n}, ζ do not. In this example, the following parameter values are chosen: $G = 5580$, $\varphi = 3.25$, $f_{\mathrm{n}} = 0.286$ Hz, $\zeta = 0.02$. Besides, two different combinations of H_{s}, T_{W} are considered: the first one ($H_{\mathrm{s}} = 0.76$ m, $T_{\mathrm{W}} = 3.36$ s) yields a narrow-band PSD characterized by $\alpha_1 = 0.998$, $\alpha_2 = 0.992$, the second one ($H_{\mathrm{s}} = 16.01$ m, $T_{\mathrm{W}} = 17.3$ s) yields a wide-band (bimodal) PSD with $\alpha_1 = 0.776$, $\alpha_2 = 0.506$. The two power spectra are compared in Figure 7.2; for simplicity, the zero-order moment is normalized to $\lambda_0 = 1$.

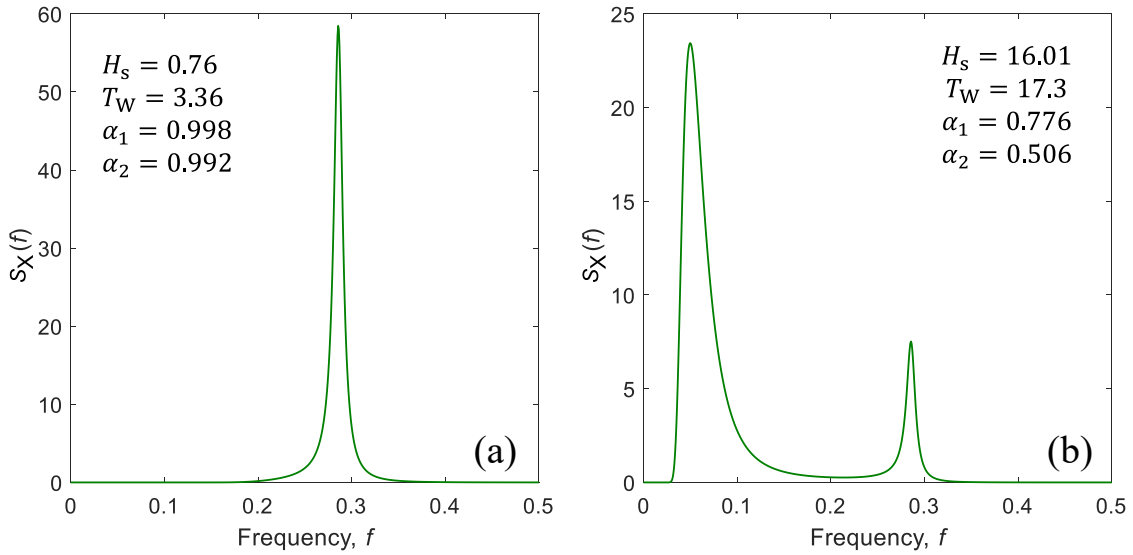

Figure 7.2. The two types of Wirsching's stress PSD used in numerical simulations: (a) narrow-band, (b) wide-band.

The formula in Eq. (7.5) is meant to represent an exact PSD, with no statistical variability. The corresponding expected damage $E[D(T)]$ can be computed by damage $E[D^{\mathrm{G}}(T)]_{\mathrm{NB}}$ for the narrow-band case, whereas for the wide-band case, the damage $E[D^{\mathrm{G}}(T)]_{\mathrm{TB}}$ from TB method is used. It represents a sort of "reference" damage value used to verify confidence interval expressions' correctness. Damage calculation assumes an S-N curve $s^{\mathrm{k}}N_{\mathrm{f}} = A$ with $A = 1$, $k = 3$. Like the expected damage, also the variance σ_{D}^2 computed from $S_{\mathrm{X}}(f)$ by the method of Madsen et al. $(\sigma_{\mathrm{D}}^2)_{\mathrm{Mad}}^{\mathrm{G}}$ represents a "reference" value for the narrow-band case. In the wide-band case, there is no mathematical formula to compute σ_{D}^2, therefore the "reference" value σ_{D}^2 was approximated by the results of Monte-Carlo simulations.

It is valuable to emphasize that the power spectral density $S_{\mathrm{X}}(f)$ in Eq. (7.5) has a double role. On the one hand, representative time-history realizations are simulated from the power spectrum, as described below. On the other hand, the power spectrum provides the expected damage $E[D(T)]$ and the variance σ_{D}^2, reference values that allow the correctness of the confidence intervals to be checked (such two "reference" values

represent unknown population parameters that are not required when, in practice, one applies the concept of confidence interval).

Random stationary Gaussian time-histories $x_i(t)$, $i = 1,2, \dots N$ of equal time-length T are simulated directly from $S_X(f)$, either narrow-band or wide-band. The length T is selected as to give approximately $2 \cdot 10^4$ cycles. As done before, the time-histories are generated by using the Discrete Fourier Transform approach, with deterministic spectral amplitudes and random phases [SMA93,WIR95].

A maximum of $N = 20$ is chosen. For each different value of N, a new different set of time-histories is simulated, for a total of $1 + 2 + 3 \dots + 19 + 20 = 210$ time-histories. The single time-history (for $N = 1$) is analyzed as per Case 1, and the multiple time-histories (for $N \geq 2$) are analyzed as per Case 2 described previously. The two confidence intervals behave as plotted in Figure 7.3 (narrow-band PSD) and Figure 7.4 (wide-band PSD). The damage values shown in all figures are normalized to the expected damage.

In order to better emphasize the accuracy of the confidence intervals in Eq. (6.2) and (7.4), a much broader set of time-histories should be analyzed. To this end, the time-history simulation procedure described was repeated a total of $2 \cdot 10^5$ times. Therefore, Figure 7.3 and Figure 7.4 only show one example out of a total of $2 \cdot 10^5$ similar results that form the entire dataset, in which it is impossible to show here all the results in their entirety.

More precisely, Figure 7.3(a) and Figure 7.4(a) compare the expected damage to the 95% confidence interval in Eq. (6.2), as a function of the number of time-histories, N. The confidence interval is drawn around the mean damage $\overline{D}(T)$ of each set of time-histories. For any N, the expected damage always falls within the confidence interval. However, this result cannot be generalized, as Figure 7.3 and Figure 7.4 only show one example, part from a much broader set. It is expected that the expected damage would fall outside the confidence interval only 5% of the time, which indeed corresponds to the definition of a 95% confidence interval.

Therefore, since the confidence interval becomes narrower as the number of time-history increases, as many time-histories as possible are needed. Obviously, the interval would be larger if the confidence level $100(1-\beta)$ were higher.

Figure 7.3(b) and Figure 7.4(b) compare, instead, the expected damage $E[D(T)]$ to the 95% confidence interval in Eq. (7.4), as a function of the number of blocks, N_{B}. In both figures, the damage $D(T)$ computed by Eq. (7.2) apparently shows no scatter and looks even constant. This negligible scatter with N_{B} (of less than 1%) actually confirms how insignificant is the number of cycles being lost after subdividing the whole time-history into blocks (this occurs even for the wide-band process). This result then confirms the validity of Eq. (7.2).

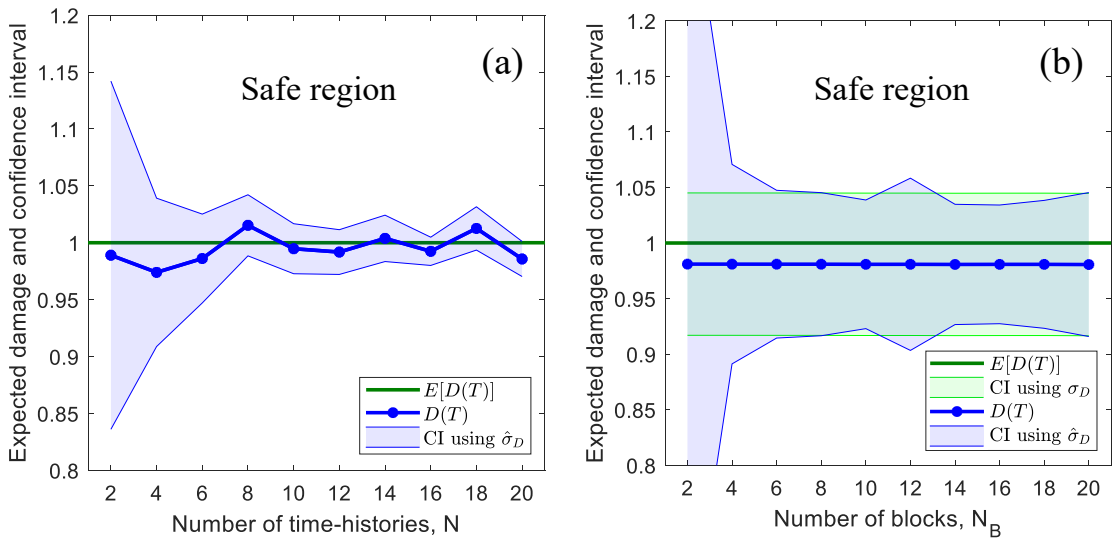

Figure 7.3. Confidence interval for Case 1 and Case 2 versus (a) the number of time-histories and (b) the number of blocks in one time-history. Results refer to the narrow-band PSD.

For this particular example, the confidence interval encloses the expected damage all over the number of blocks considered. The figure also displays the confidence interval analogous to Eq. (7.4), but constructed with the "true" standard deviation, σ_{D}, of the

damage of the random process, and computed by the Madsen et al. method directly from the "true" power spectrum $S(f)$.

It may be noticed that, as the number of blocks increases, the confidence interval constructed around the damage $D(T)$ converges to the confidence interval based on the "true" standard deviation. On the one hand, this result highlights the importance of considering as many blocks as possible to narrow the confidence interval, provided that each block is long enough to give a sufficient number of cycles. On the other hand, it also highlights that the confidence interval width does not converge to zero as the number of blocks increases. Still, it approaches the scatter of the damage that characterizes the random process.

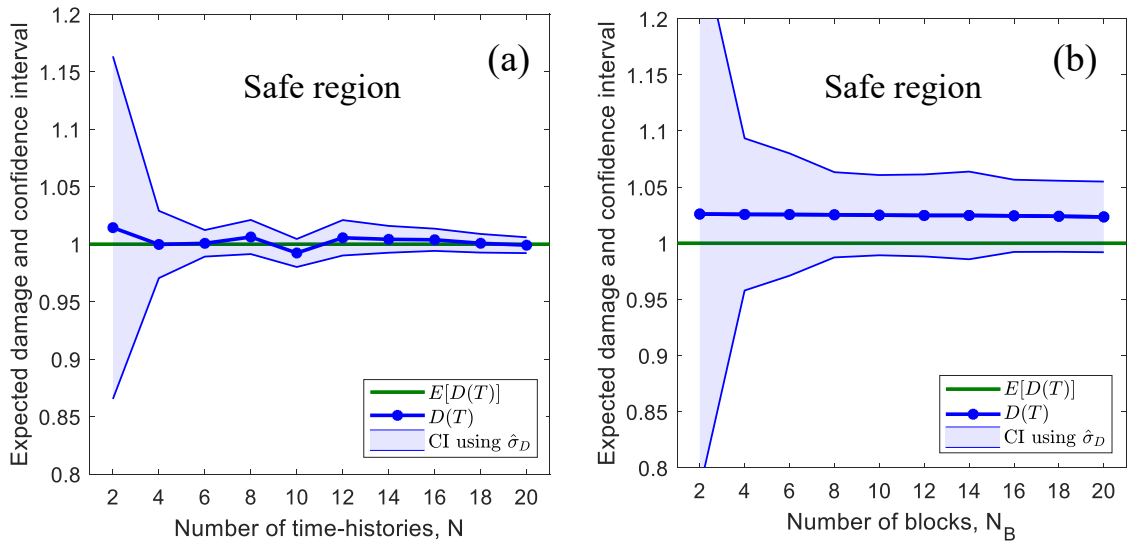

Figure 7.4. Confidence interval for Case 1 and Case 2 versus (a) the number of time-histories and (b) the number of blocks in one time-history. Results refer to the wide-band PSD.

In this example, the expected damage $E[D(T)]$ is known, and it was used to check the correctness of confidence interval expressions, but the expected damage is never known in practice. This implies that it is unknown whether the damage $D(T)$ from one time-history underestimates or overestimates the expected damage. Regard, however, that

a structure would be designed unsafely if the expected damage were minimized. The safe region is only that in which $D(T)$ is higher than $E[D(T)]$. Since $E[D(T)]$ is unknown, it is recommended to take the upper confidence limit as the lowest reference value in the structure design.

The examples in Figure 7.3 and Figure 7.4 show that the expected damage always falls within the confidence limits. However, it should be emphasized that both figures only refer to one single result out of a total of $2 \cdot 10^5$ similar ones. In other words, if another simulation were carried out, the expected damage could fall either inside or outside the confidence interval. The interpretation of a 95% confidence is that 5 out of 100 simulations would fall outside.

Therefore, a conclusion about the accuracy of the confidence interval expressions can only be made by analyzing the whole set of $2 \cdot 10^5$ replicated samples and counting for each of them how many times the confidence interval encloses the expected damage. Virtually, this number should be equal to 95%.

Figure 7.5(a) and Figure 7.6(a) show a subset of 20 confidence intervals, for the case of $N = 20$ time-histories with about $2 \cdot 10^4$ cycles each (for better clarity, not all confidence intervals are shown). Regard that some confidence intervals do not contain the expected damage, and some do. The ratio between the number of confidence interval containing the expected damage to the total number of intervals provides an estimated confidence $100\left(1 - \hat{\beta}\right)\% = 94.48\%$ for both the narrow-band and the wide-band PSD cases, which is almost coincident with the theoretical value.

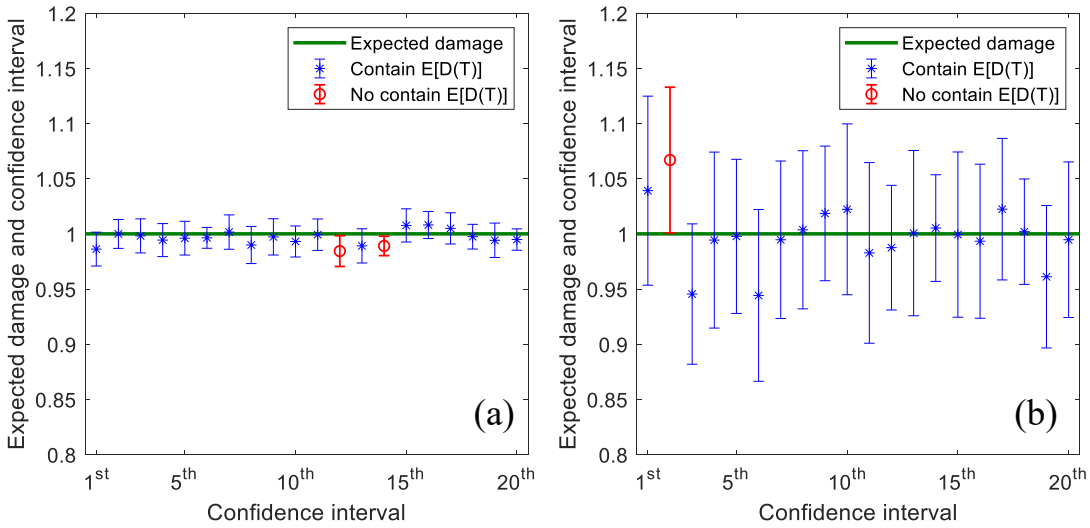

Figure 7.5. Check of confidence intervals using (a) $N = 20$ time-histories and (b) one time-history divided into $N_B = 20$ blocks. Results refer to the narrow-band PSD.

The same argument also applies to the case of only one time-history (details in Figure 7.5(b) and Figure 7.6(b)), for which the estimated confidence is $100(1 - \hat{\beta})\% = 94.49\%$ for the narrow-band PSD, whereas a value of 94.48% follows from the wide-band PSD.

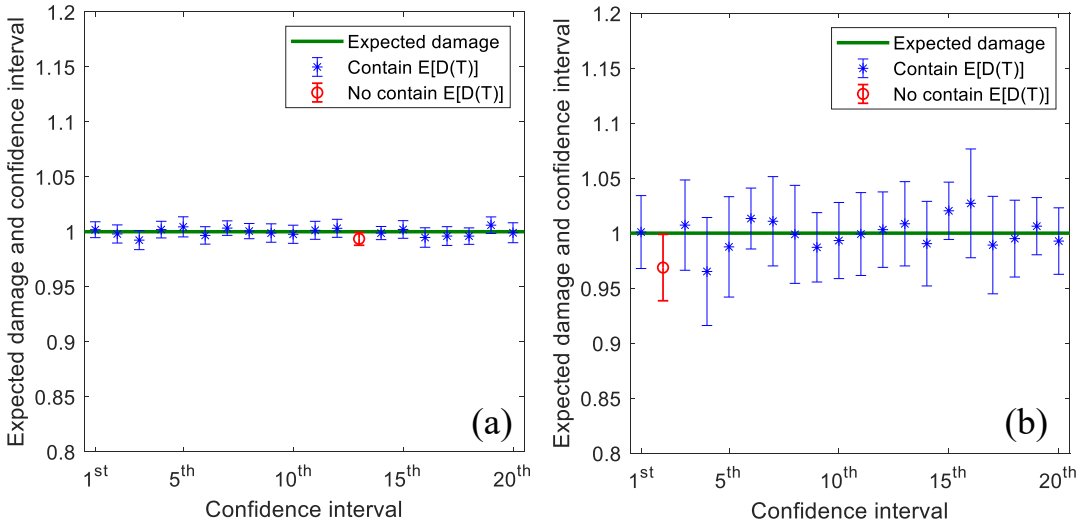

Figure 7.6. Check of confidence intervals using (a) $N = 20$ time-histories and (b) one time-history divided into $N_B = 20$ blocks. Results refer to the wide-band PSD.

7.4 MEASURED TIME-HISTORY RECORDS FROM A MOUNTAIN-BIKE

7.4.1 Methods and measurements

This study's primary purpose was to obtain real measurements to estimate the expected damage and calculate the confidence intervals. The present research did not intend to evaluate the safety of the Mountain-bike on an off-road track. By the apparatus described below, the Mountain-bike was, however, well-equipped to record time-histories in a typical north Italian off-road track and to use them to verify the methods described above.

The Mountain-bike is a 2010 Scott Sportster P6 (Figure 7.7(a)), its frame is made of an aluminum 6061 alloy, and the rigid front fork is a Unicrown made of carbon steel. Two Rigida Cyber 10 size 700C wheels are coupled with 700 x 37c S207 semi-slick tires. The handlebar and the saddle are made by Scott Sports, while the transmission, chain, and crankset are made by Shimano, Inc.

The bicycle front fork was instrumented with a Strain Gauge Bridge calibrated during static laboratory tests. A bending half-bridge was applied close to the middle of the front fork in the longitudinal plane, Figure 7.7(b), to monitor the loads acting on the Mountain-bike. Two strain gauges were placed symmetrically on the left tube. They were manufactured by HBM, and the model was LY Linear Strain Gauges with 1 Measuring Grid (only one direction).

Measured time-histories were collected through a Dewesoft data acquisition system, a Minitaurs Dewe-101 with 8 channels model, a model which contains an industrial power computer built directly in the unit. A filter was set with a cut-off frequency of 300 Hz, which was above the maximum frequency of interest [LOR99]. A sampling frequency was fixed at 1000 Hz. The main “triangle” of the bicycle frame was utilized to fix the data acquisition on the inclined tube, and the rechargeable supply battery was allocated behind the seat by a welded support.

Also, a speedometer containing a sensor and magnet fixed on a spoke was used for monitoring the Mountain-bike speed. It was made by Marwi Group, and the model was a Union 8 Cycling Computer. The fully equipped Mountain-bike weighed about 12.2 kg.

Figure 7.7. Mountain-bike: (a) overall view of the bicycle and components; (b) two strain gauges applied to the front fork.

The cycling conditions were set to obtain stationary random time-histories. The short off-road track of 0.5 kilometers length was plane (or almost plane) with a gravel surface, a typically north Italian track (left side of Figure 7.8) located at the Ippodromo Comunale in Ferrara city. A rider of 59 kg mass guided the bicycle in a seated condition. The speed was kept practically constant at 15 km/h. Based on these requirements, it is expected that each time-history represents a stationary (or almost stationary) random loading. These cycling conditions may not represent a critical situation in which a Mountain-bike on an off-road track is subject to. In fact, service loadings experienced by off-road bicycles are usually rather irregular and also non-stationary (e.g. different tracks with various speeds). However, the same cycling conditions over time were needed to investigate the confidence intervals applied to only stationary random loadings.

Figure 7.8. Part of a typically north Italian off-road track (left side of the picture)

During 9 consecutive days, 41 measured time-histories were obtained under the same cycling conditions. On Days 1-2, measurements were performed to collect 10 time-histories used for the confidence interval in Case 1. On the other hand, Case 2 required only one time-history recorded on Day 3. The remaining 30 time-histories were measured on Days 4-9, and they are intended to be used for approximating the expected damage by the sample mean of 30 damage values. Note that the estimated expected damage was needed to verify the proposed confidence intervals' accuracy in the present work. However, the confidence intervals do not require knowing the expected damage when applied in real cases. Consequently, those mentioned above 30 measured time-histories are not needed in reality and used only for verification purposes. The minimum values of measured random time-history are $N = 2$ for Case 1 and $N = 1$ for Case 2.

All measured time-histories in this study were fixed at a time length $T = 300\ s$ and were normalized to have a zero mean $\mu_x = 0$ value and a variance equal to unity $\sigma_x^2 = 1$. An example is reported in Figure 7.9 for the first measured time-history $x_1(t)$ from the bicycle front fork. In this particular time-history $x_1(t)$ it is possible to appreciate how there is no significant change in the mean and variance levels over time. Although

the actual time-history values cannot be precisely predicted, which is a characteristic of the randomness of the loading, at least two well-separated frequencies are observed in the zoomed view of $x_1(t)$, see the right side of Figure 7.9.

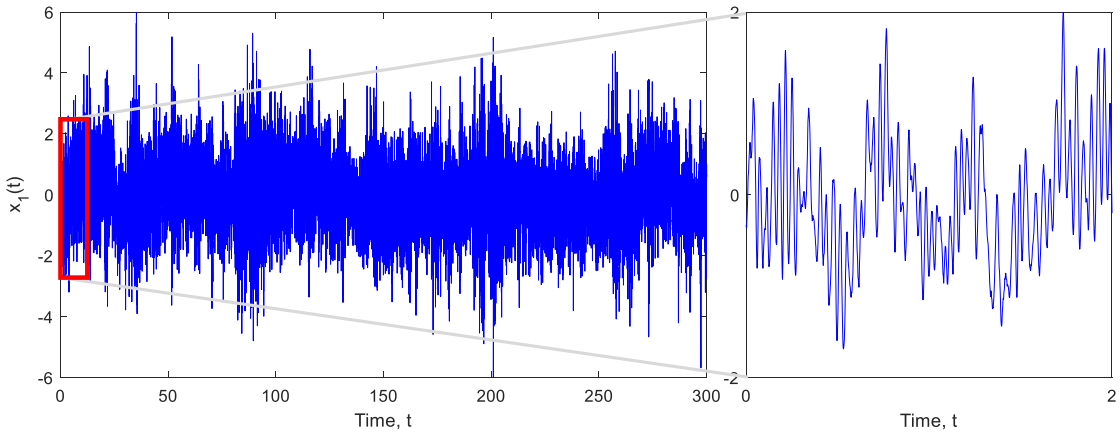

Figure 7.9. First measured time-history record $x_1(t)$ from the Mountain-bike front fork: global and zoomed view.

7.4.1.1 Stationary random loadings

The confidence interval formulae in Eq. (6.2) and (7.4) are only applicable to stationary random loadings, which have properties (e.g., frequency content, mean and standard deviation) that do not change over time. Different approaches (qualitative or quantitative) can identify the stationarity [BEN07,BEN10]. Among them, the comparison of the loading (or cumulative) spectrum can be used to compare the statistical distribution of rainflow cycles when several measured time-histories are available. A comparison of loading spectra is demonstrated in Figure 7.10 by using five measured time-histories.

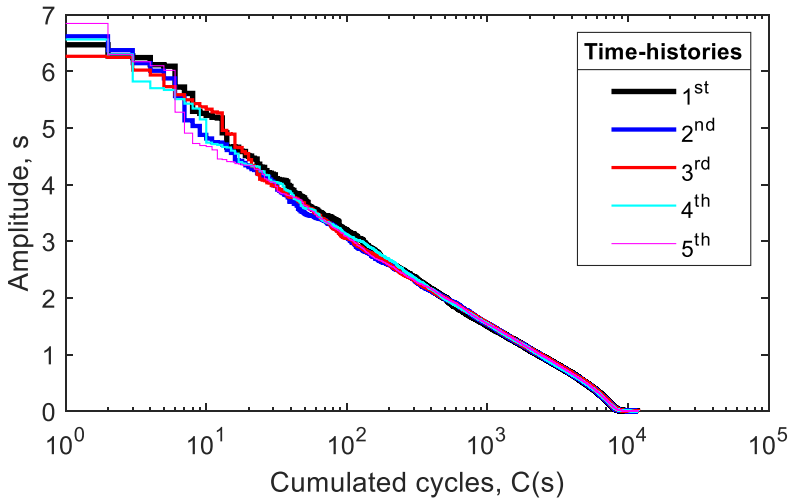

Figure 7.10. Comparison of loading spectra using five measured time-histories.

Figure 7.10 delivers a helpful description of the cycle events for each measured time-history considered. The comparison between the five time-history loading spectra shows that the lower is the amplitude s, the better is the agreement over cumulated cycles $C(s)$. Anyhow, the loading spectra are generally well overlapped, confirming that the measured time-histories are stationary.

The Short-Time Fourier Transform (STFT) is also used to analyze how the frequency content of a time-history $x(t)$ changes over time. The procedure for computing STFT is to divide the time-history $x(t)$ into N_B blocks of equal length T_B and then compute the Fourier transform of each one. The duration of the block T_B has an indispensable influence on the time and the frequency resolution. Unfortunately, high resolutions cannot be achieved in both domains because they are inversely proportional. These resolutions can be controlled using the threshold of $\varepsilon_\mathrm{r} \geq 0.2$ and $\Delta f \geq 0.1$, see Chapter 6. The value of $\varepsilon_\mathrm{r} = 0.10$ and $\Delta f = 0.10$ are here chosen regarding the best compromise among time- and frequency-domain resolution. Overlaps between consecutive blocks are normally expected to reach a high number of blocks N_B, which results in a better time resolution. Consequently, each time-history was divided so to have $T_\mathrm{B} = 10\ s$ and 75% of overlap fraction. The frequency resolution is artificially increased

by adding zero values at the end of blocks (zero paddings). The application of the STFT on the first measured time-history $x_1(t)$ from the bicycle is exhibited in Figure 7.11(a). Alike results are obtained for the other time-histories.

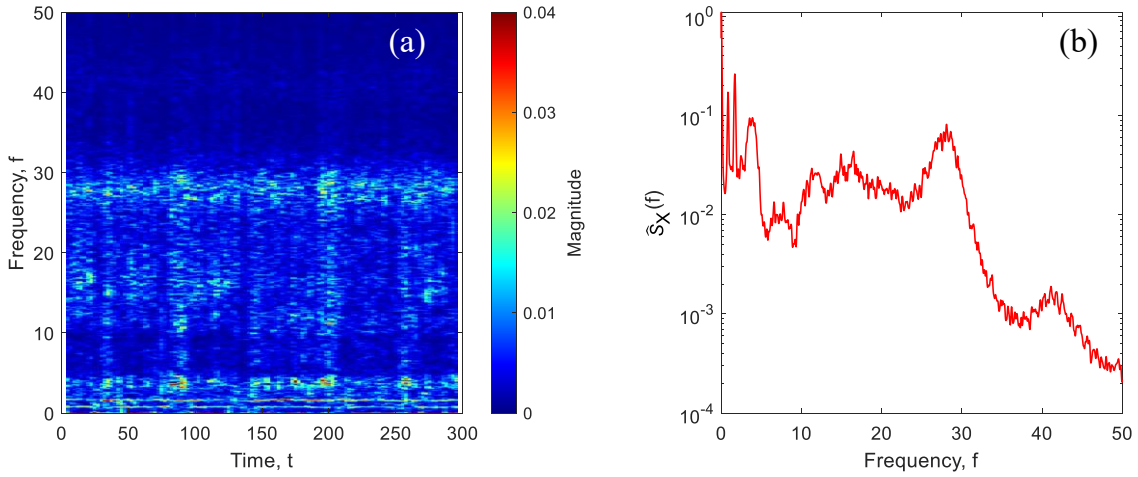

Figure 7.11. Measured time-histories: (a) Short-Time Fourier Transform; (b) Power Spectral Density.

The STFT displays no noticeable change in the frequency content (range from 0 to 50 Hz) over time, as well as the amplitude of the STFT (intensity indicated in the color bar in Figure 7.11(a)). These qualitative results were somehow expected due to the predisposed cycling conditions.

As the frequency content is shown not to vary over time, it is possible to characterize the random loading in the frequency-domain by a one-sided Power Spectral Density (PSD). It also allows the differences in the distribution of power over frequencies to be appreciated best. To analyze the first measured time-history $x_1(t)$, the estimated PSD $\hat{S}_x(f)$ in Figure 7.11(b) is computed by Welch's method [LAL14,WIR95,BEN86]: Hanning block (or window), 75% overlapping and $T_B = 10\ s$. It is interesting to note that the estimated PSD extends over a wide range of frequencies, which characterizes a so-called wide-band random loading. A few low frequency components are also observed in $\hat{S}_x(f)$ from 0 to 5 Hz and a high frequency component is perceived at about 28 Hz. In

fact, low frequencies are usually detected in random time-histories by numerous small cycles while high frequency gives large cycles. Following the previously statement, at least two well-separated frequencies have the first measured time-history, small and large cycles in Figure 7.9 are emphasized by low and high frequencies in Figure 7.11.

The run test method using the proposed approach (see Chapter 6) is applied here to quantify the stationarity of the first measured time-history $x_1(t)$. It considers the damage $D_{\mathrm{B,i}}(T_{\mathrm{B}})$ computed in time-domain (rainflow counting and Palmgren-Miner rule) for each block rather than using the usual statistical parameters, e.g., the $RMS_{\mathrm{B,i}}(T_{\mathrm{B}})$ value, as the output calculated in each block. By this proposed approach, in contrast to the Rouillard's one [ROU14], the run test applied here can detect the changes in the variance of measured time-histories and the changes in the mean and frequency; for more details, see Chapter 6.

The same block length $T_{\mathrm{B}} = 10\ s$ used for the STFT is exploited as a first attempt. The statistical error and frequency resolution results in $\varepsilon_{\mathrm{r}} = 0.183$ and $\Delta f = 0.1$, respectively. The proposed run test applied to first measured time-history $x_1(t)$ using damage $D_{\mathrm{B,i}}(T_{\mathrm{B}})$ values (normalized to the median) is demonstrated in Figure 7.12. Damage calculation assumes an S-N curve $s^{\mathrm{k}}N_{\mathrm{f}} = A$ with $A = 1,\ k = 3$. Note that damage $D_{\mathrm{B,i}}(T_{\mathrm{B}})$ values is used as statistical parameter only, and not used for a damage accumulation assessment, see Chapter 6.

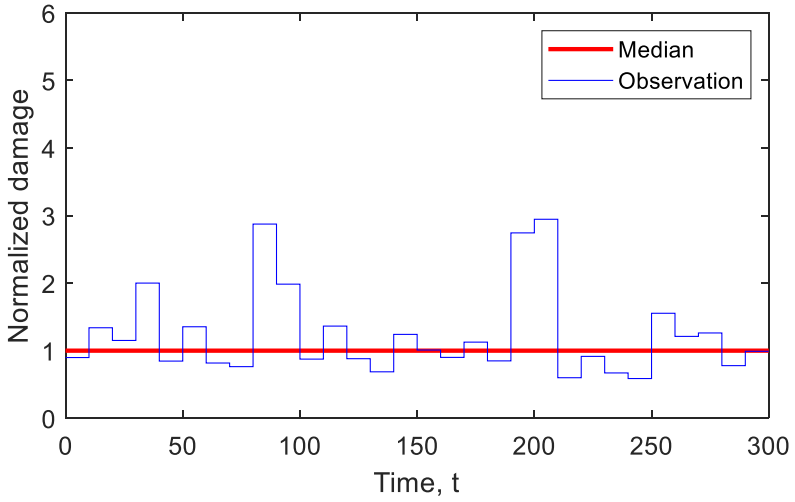

Figure 7.12. Proposed run test using the damage $D_{\mathrm{B,i}}(T_{\mathrm{B}})$ values applied to first measured time-history $x_1(t)$.

There are $r = 17$ runs (number of damage $D_{\mathrm{B}}(T_{\mathrm{B}})$ reversals relative to median) represented by the sequence of $N_{\mathrm{B}} = 30$ observed block values. The upper and lower values are obtained by the tabulation in [BEN86]. So, the acceptance region of run test results in $10 < 17 \leq 21$ for 95% level of significance. The first measured time-history $x_1(t)$ is then quantified as stationary since $r = 17$ falls within $r_{15,0.975} = 10$ and $r_{15,0.025} = 21$. The proposed run test is conducted for all the measured time-history records considered. Although not shown here, the results quantified all measured time-histories as stationary random loadings.

7.4.2 Confidence intervals and expected damage using measurements

The confidence intervals for the expected damage in Eq. (6.2) and (7.4) are constructed from the damage values computed from the measurements in the Mountain-bike front fork, as those usually gathered in other similar engineering applications, see Figure 7.13(a).

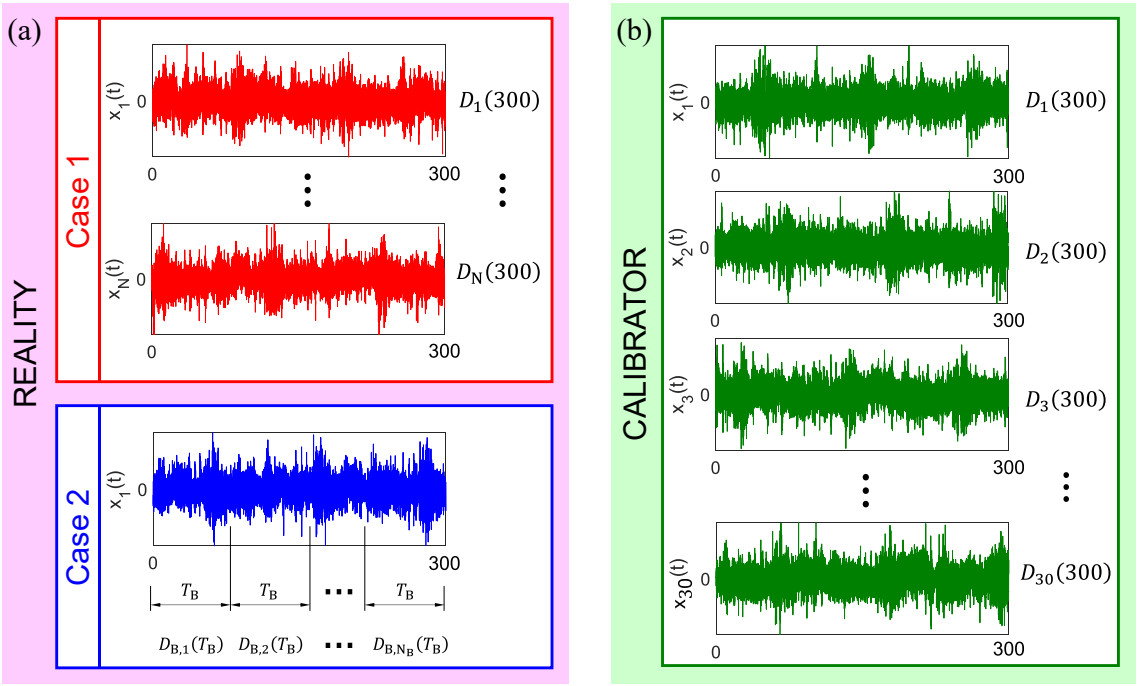

Figure 7.13. Measured time-history records used for: (a) confidence intervals; (b) approximating the expected damage.

The intervals are constructed with a 95% confidence level by considering the values $D_i(T)$ and $D_{B,i}(T_B)$ used in Case 1 and Case 2, respectively. All time-histories $x(t)$ from which the damage is computed were measured with an equal time-length $T = 300$ s, which guarantees at least $1 \cdot 10^4$ counted cycles. In Case 1, the confidence interval was computed for various amount of time-histories $N = 2,3, \ldots 10$. For all N values, the same set was considered. In Case 2, another measured time-history was considered along with multiple blocks $N_B = 2,3, \ldots 10$ to estimate the confidence interval.

In practice, the entire ensemble of measured time-histories is not available and, consequently, the expected damage is never known. Nonetheless, a reasonable approximation to the expected damage is required to evaluate the proposed confidence intervals in Eq. (6.2) and (7.4) using real measurements. The expected damage was then estimated by considering a different set of stationary measured time-histories (see Figure 7.13(b)) from the Mountain-bike. This means that the damage $D_i(T)$ were different values

from those used for the confidence intervals. The sample mean of several damage values $\overline{D}(T) = N^{-1} \sum_{\mathrm{i}=1}^{\mathrm{N}} D_{\mathrm{i}}(T)$ was calculated by the damage in time-domain (rainflow counting method and the Palmgren-Miner rule). To approximate the expected damage $E[D(T)]$ with the sample mean damage $\overline{D}(T)$, a large finite set of $N = 30$ damage values was chosen. This sample mean damage value $\overline{D}(T)$ computed by $N = 30$ was assumed in this study to be the expected damage $E[D(T)]$. It is a sort of calibrator sample damage to which all other damage values from measurements are compared.

7.4.3 Results and discussions

The principal values used for the confidence interval in Case 1 and Case 2 and the calibrator sample damage with its standard deviation are presented in Table 4.1. Leftward, Table 4.1 delivers the sample mean $\overline{D}(T)$ and sample standard deviation $\hat{\sigma}_{\mathrm{D}}$ of Case 1 over the number of measured time-histories N. Centrally located, it presents the damage $D(T)$ calculated by Eq. (7.2) and the standard deviation $\hat{\sigma}_{\mathrm{D}}$ in Eq. (7.3) along with the different number of blocks N_{B}. Rightward, Table 4.1 exhibits the sample mean $\overline{D}(T)$ and sample standard deviation $\hat{\sigma}_{\mathrm{D}}$ of the damage calibrator.

Table 7.1. The sample mean $\overline{D}(T)$ and standard deviation $\hat{\sigma}_{\mathrm{D}}$ of Case 1 on the left side, $D(T)$ calculated by Eq. (7.2) and $\hat{\sigma}_{\mathrm{D}}$ Eq. (7.3) on the middle, and calibrator sample damage $\overline{D}(T)$ with its $\hat{\sigma}_{\mathrm{D}}$ on the right.

Case 1			Case 2			Calibrator		
N	$\overline{D}(T)$	$\hat{\sigma}_{\mathrm{D}}$	N_{B}	$D(T)$	$\hat{\sigma}_{\mathrm{D}}$	N	$\overline{D}(T)$	$\hat{\sigma}_{\mathrm{D}}$
2	124608	9592	2	124737	7450	30	136671	9149
3	132845	15796	3	124573	10961			
4	133955	13087	4	124554	12278			
5	134387	11375	5	124559	12378			
6	133485	10411	6	124222	12098			
7	135022	10338	7	124216	9689			
8	135511	9671	8	124387	15661			
9	134326	9720	9	124290	12288			
10	134180	9176	10	124365	14472			

In Case 1, the highest number of time-histories $N = 10$ gives the lowest standard deviation $\hat{\sigma}_{\mathrm{D}}$. In Case 2, the damage $D(T)$ is almost constant (maximum difference of 0.5%) by varying N_{B} and the standard deviation $\hat{\sigma}_{\mathrm{D}}$ results in a greater scatter (about 50%) than Case 1. The calibrator sample damage and its standard deviation (on the right of Table 4.1) may be compared with the results from Case 1 (on the left of Table 4.1) since the same procedure lead to $\overline{D}(T)$ and $\hat{\sigma}_{\mathrm{D}}$. The standard deviation $\hat{\sigma}_{\mathrm{D}}$ presents a small decrease of about 0.3% between the calibrator and Case 1 for $N = 10$. It emphasizes the importance of the sample size N with respect to the variability of damage. In other words, by increasing the number of measured time-histories N, the standard deviation $\hat{\sigma}_{\mathrm{D}}$ decreases and the $\overline{D}(T)$ approaches the "true" $E[D(T)]$, although, in practice, the standard deviation $\hat{\sigma}_{\mathrm{D}}$ will never equal zero as well as the $\overline{D}(T)$ will never coincide with the "true" $E[D(T)]$.

The confidence interval in Case 1 versus the number of measured time-histories N is verified using the expected damage $E[D(T)]$ (approximated here with the calibrator sample damage), see Figure 7.14(a). The confidence interval encloses $[D(T)]$ over all N, confirming the correctness of the proposed approach at least when applied to the stationary measured time-histories of this study. The sample damage $\overline{D}(T)$ in Case 1 approaches the $E[D(T)]$ as the number of measured time-histories increases. Furthermore, the greater the number of time-histories, the narrower is the confidence interval of damage. This follows the same direction as observed when the proposed approach was applied to simulated time-histories [MAR20a], suggesting the need to use as many measured time-histories as possible to get a narrow confidence interval [MAR20a,MAR21c].

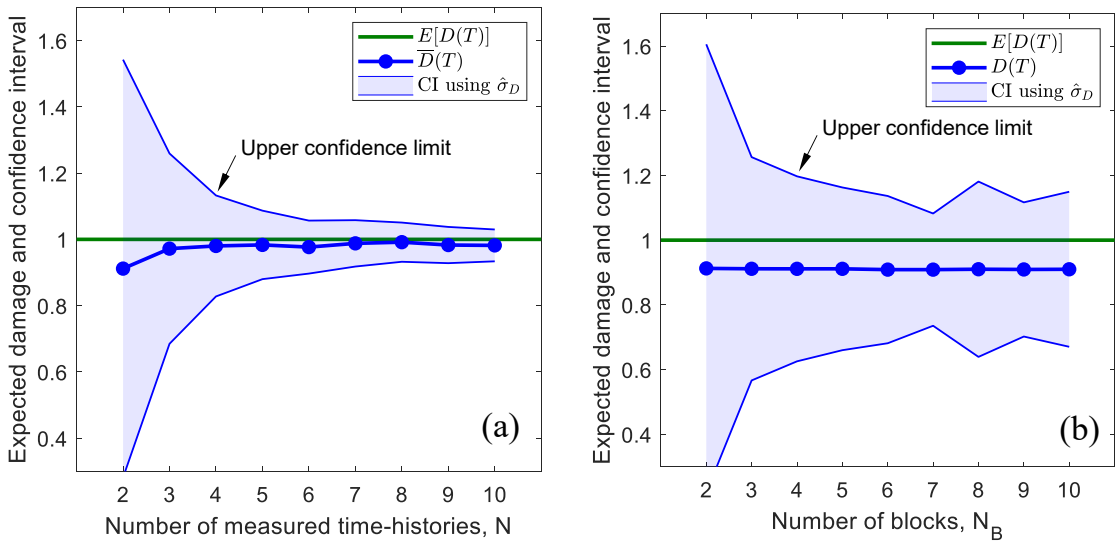

Figure 7.14. The confidence interval for Case 1 and Case 2, versus (a) the number of measured time-histories and (b) the number of blocks in one measured time-history.

Figure 7.14(b) compares the expected damage $E[D(T)]$ to the confidence interval in Case 2 as a function of the number of blocks N_B. The confidence interval containing the $E[D(T)]$ reveals to be very similar to its result using simulated time-histories [MAR20a]. This result confirms once more the correctness of the proposed confidence interval using real measurements.

Observe that if the expected damage $E[D(T)]$ were underestimated, a structure would not be designed safely. The safe region is only that in which $\overline{D}(T)$, in Case1, or $D(T)$, in Case 2, is greater than $E[D(T)]$. It is then recommended to take the upper confidence limit (Figure 7.14(a) and (b)) as the reference damage value to be used in the structure design [MAR20a,MAR21c].

Chapter 8

MULTIAXIAL RANDOM LOADING: APPLICATION TO THE CSV CRITERION

8.1 INTRODUCTION

Chapter 4 presented the variance of fatigue damage caused by the randomness of a stationary Gaussian random loading. Best-fitting expressions were derived to relate the variance of damage directly to bandwidth parameters of a PSD. Chapter 5 presented two theoretical models to assess the variance of fatigue damage in stationary narrow-band non-Gaussian random processes. These models extended two solutions existing in the literature and restricted to Gaussian processes. Chapter 6 introduced a run test approach to verify the stationarity of time-histories. The proposed approach considers the damage values computed for each independent block as the statistical parameters. This procedure can detect changes in the variance, mean, and frequency content of time-histories. Chapter 7 analyzed the variability of damage based on one or a few time-histories. In both cases, confidence intervals were constructed to bound the expected damage. Although Chapters 4-7 present original contributions in structural durability analysis, they are restricted to uniaxial random loadings. However, this hypothesis is not always satisfied by the random loadings action on real engineering structures. Consequently, multiaxial random loadings need to be considered in such situations.

Multiaxial spectral methods are increasingly used in the structural durability analysis under multiaxial random loading. They adopt a frequency-domain approach in which the multiaxial random loading is characterized by a PSD matrix (see Chapter 2). In this way, multiaxial spectral methods can be considered frequency-domain re-formulations of classical multiaxial fatigue criteria in time-domain [BEN16,CAR17].

Like time-domain criteria, also spectral methods are classified based on the concepts of critical plane, stress invariants, or equivalent stress [BEN16,CAR17,BEL07, BEN08]. A common feature of critical plane methods is to compute a certain quantity (e.g. stress PSD, shear amplitude, or fatigue damage) for all planes passing through a point and then to identify the plane where the calculated quantity is most critical. An example is the spectral method using the Carpinteri-Spagnoli-Vantadori (CSV) criterion. It employs a sequence of five rotations to identify the critical plane, within which an equivalent stress and its power spectrum are defined [CAR14,CAR16,VAN18,VAN19]. This method requires that the stress PSD matrix be determined in every plane. In a numerical analysis where angular intervals are digitalized into discrete values, the number of planes to be scanned matches the number of combinations of digitalized angular values. Scanning such combinations can only be accomplished by setting up a sequence of "for/end" loops, which considerably increases the computation time. Furthermore, the algorithm requests the computation of all auto- and cross-power spectral densities of the PSD matrix in every iteration, although not all these power spectra are necessary to decide if the rotated plane is indeed the critical one.

The computational time may further grow if the algorithm has to be applied not just once but many times, as many as the number of nodes in a finite element model. In most cases, the analysis of all nodal results in a finite element model is not needed, since it may be restricted to small subsets of nodes from the most stressed regions (e.g. surfaces), although it is not always possible to predict *a priori* which regions (especially if of complex geometry) will be the most critical.

This chapter proposes a new algorithm for implementing the CSV criterion and to shorten the computation time when all the finite element model nodes are considered. This goal was achieved in two phases. The first one consisted in computing the analytical expressions of only those spectral moments used for determining the largest variance and expected largest peak of normal/shear stress in any rotated reference frame at a given point. The second one was to employ those analytical expressions into a numerical routine that, dismissing "for/end" loops, is much faster than the standard algorithm.

This new approach applied to the CSV criterion has indeed a general validity. As a matter of fact, it can be adapted to other multiaxial spectral methods that make use of angular rotations or direction cosines to seek the critical plane, or that look for the maximum variance of an equivalent stress in a rotated reference frame [GRZ91,BĘD92, PIT01].

8.2 THE SPECTRAL METHOD BY CARPINTERI-SPAGNOLI-VANTADORI (CSV)

8.2.1 Summary of the computation steps

This section summarizes the necessary steps to apply the CSV spectral method. The description requires to find the critical plane by five rotations, which is followed by [VAN19]. A slightly different notation is adopted by alternative articles [CAR14,CAR16, VAN18]. They provide more details, here omitted, on the conceptual framework of the criterion that explains the multiaxial fatigue damage.

The CSV criterion defines a reference frame P_{XYZ} with origin at a material point and right-hand orthogonal axes, see Figure 8.1(a). This reference frame is fixed in space. Further steps in Figure 8.1(b) and (c) introduce other two reference frames in rotated positions, but with the same origin.

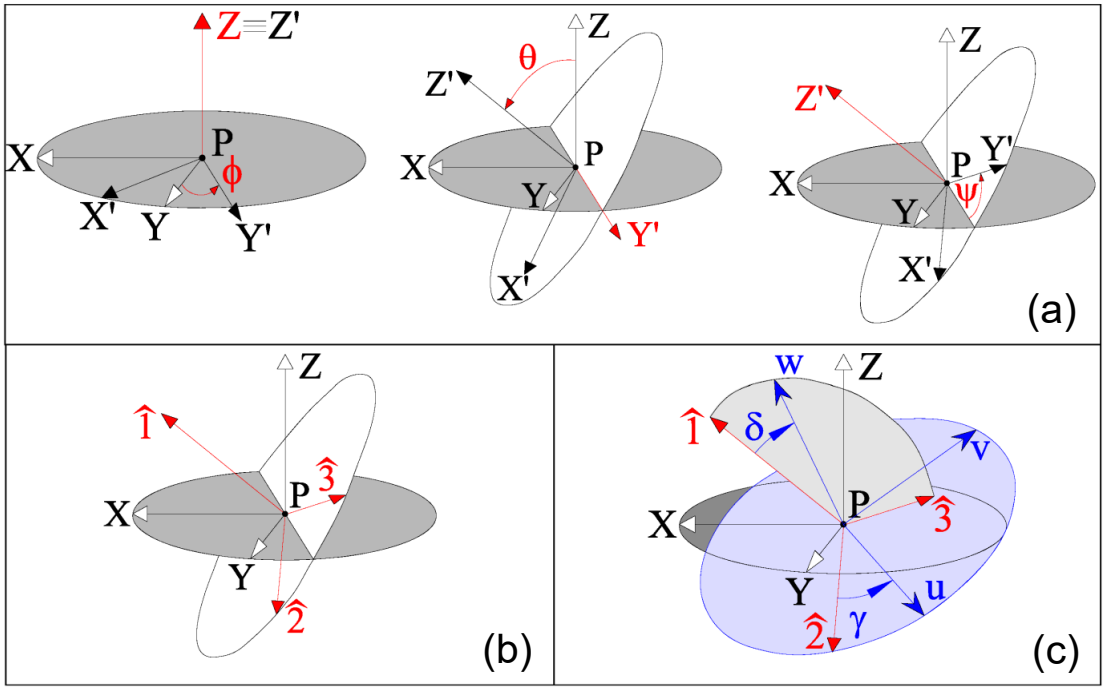

Figure 8.1. (a) The five rotations in CSV criterion. (a) initial reference frame P_{XYZ} and first rotated frame $P_{X'Y'Z'}$ after three rotations (ϕ, θ, ψ); (b) frame $P_{\hat{1}\hat{2}\hat{3}}$ of average principal directions; (c) frame P_{uvw} attached to the critical plane, obtained after two rotations (δ, γ) (Reprinted from [VAN19], with permission from Elsevier).

In frame P_{XYZ}, the stress vector is $\boldsymbol{\sigma}_{XYZ}(t)$ and its PSD matrix $\mathbf{S}_{XYZ}(f)$. A first rotated reference frame $P_{X'Y'Z'}$ is introduced with origin at a given point. Its orientation in the space is defined by a sequence of three Euler angles (ϕ, θ, ψ). In frame $P_{X'Y'Z'}$, the stress vector is $\boldsymbol{\sigma}_{X'Y'Z'}(t) = \left[\sigma_{x'x'}(t), \sigma_{y'y'}(t), \sigma_{z'z'}(t), \tau_{y'z'}(t), \tau_{x'z'}(t), \tau_{x'y'}(t)\right]^{T}$ and its PSD matrix is:

$$\mathbf{S}_{X'Y'Z'}(f) = \mathbf{R}(\phi, \theta, \psi)\, \mathbf{S}_{XYZ}(f)\, \mathbf{R}(\phi, \theta, \psi)^{T} \tag{8.1}$$

The rotation matrix $\mathbf{R}(\phi, \theta, \psi) = \mathbf{R}_{\psi}\mathbf{R}_{\theta}\mathbf{R}_{\phi}$ is the product of three matrices that represent three successive rotations ϕ, θ, ψ – applied in this order – by which $P_{X'Y'Z'}$ is oriented with respect to P_{XYZ}. Matrix $\mathbf{R}(\phi, \theta, \psi)$ is provided by expression [VAN19]:

$$\mathbf{R}(\phi,\theta,\psi)=\begin{bmatrix} c_\psi^2 & s_\psi^2 & 0 & 0 & 0 & 2c_\psi s_\psi \\ s_\psi^2 & c_\psi^2 & 0 & 0 & 0 & -2c_\psi s_\psi \\ 0 & 0 & 1 & 0 & 0 & 0 \\ 0 & 0 & 0 & c_\psi & s_\psi & 0 \\ 0 & 0 & 0 & -s_\psi & c_\psi & 0 \\ -c_\psi s_\psi & c_\psi s_\psi & 0 & 0 & 0 & c_\psi^2 - s_\psi^2 \end{bmatrix}$$

$$\begin{bmatrix} c_\theta^2 & 0 & s_\theta^2 & 0 & 2c_\theta s_\theta & 0 \\ 0 & 1 & 0 & 0 & 0 & 0 \\ s_\theta^2 & 0 & c_\theta^2 & 0 & -2c_\theta s_\theta & 0 \\ 0 & 0 & 0 & c_\theta & 0 & -s_\theta \\ -c_\theta s_\theta & 0 & c_\theta s_\theta & 0 & c_\theta^2 - s_\theta^2 & 0 \\ 0 & 0 & 0 & s_\theta & 0 & c_\theta \end{bmatrix} \tag{8.2}$$

$$\begin{bmatrix} c_\phi^2 & s_\phi^2 & 0 & 0 & 0 & 2c_\phi s_\phi \\ s_\phi^2 & c_\phi^2 & 0 & 0 & 0 & -2c_\phi s_\phi \\ 0 & 0 & 1 & 0 & 0 & 0 \\ 0 & 0 & 0 & c_\phi & s_\phi & 0 \\ 0 & 0 & 0 & -s_\phi & c_\phi & 0 \\ -c_\phi s_\phi & c_\phi s_\phi & 0 & 0 & 0 & c_\phi^2 - s_\phi^2 \end{bmatrix}$$

in which $c_{\mathrm{x}} = \cos x$ and $s_{\mathrm{x}} = \sin x$ are trigonometric functions used throughout the text.

The first step in the CSV criterion is to scan the angles ϕ and θ (in intervals $0 \leq \phi \leq 2\pi$ and $0 \leq \theta \leq \pi$), with the aim to find that particular direction Z' (defined by the values ϕ^*, θ^*) along which the expected largest peak of normal stress $\sigma_{\mathrm{z'z'}}(t)$ in time duration T is maximum (Davenport formula [DAN64]):

$$E\left[\max_{0\leq \mathrm{t}\leq \mathrm{T}} \sigma_{\mathrm{z'z'}}(t)\right] \cong \sqrt{\lambda_{0,3'3'}}\left(\sqrt{2\ln\left(N_{0,3'3'}\right)} + \frac{0.5772}{\sqrt{2\ln\left(N_{0,3'3'}\right)}}\right) \tag{8.3}$$

Note that an asterisk specifies a particular value of a variable within the text: for example, ϕ denotes a variable that spans an interval $0 \leq \phi \leq 2\pi$, whereas the symbol ϕ^* indicates one value (with periodicities) within that interval.

Eq. (8.3) only depends on the variance, $\lambda_{0,3'3'}$, and the number of mean upcrossings (in time T), $N_{0,3'3'} = \nu_0 T = T\sqrt{\lambda_{2,3'3'}/\lambda_{0,3'3'}}/2\pi$, of the normal stress $\sigma_{\mathrm{Z'Z'}}(t)$. The angles ϕ^* and θ^* do not depend on the actual value of T in Eq. (8.3) and, therefore, a dummy length of $T = 1$ s can be taken in the calculations. Further, the value of ψ is irrelevant for localizing Z'.

Spectral moments $\lambda_{0,3'3'}$ and $\lambda_{2,3'3'}$ derive from the power spectrum $S_{3'3'}(f)$ in position 33 in the rotated PSD matrix $\mathbf{S}_{\mathrm{X'Y'Z'}}(f)$ (index 33 derives from the position 3 of stress $\sigma_{\mathrm{Z'Z'}}(t)$ in vector $\boldsymbol{\sigma}_{\mathrm{XYZ}}(t)$). A sequence of steps should be followed to compute $E[\max \sigma_{\mathrm{Z'Z'}}(t)]$ for a given pair of angles (ϕ, θ). First, compute the rotated matrix $\mathbf{S}_{\mathrm{X'Y'Z'}}(f)$ for those angles (ϕ, θ), then calculate the two spectral moments of $S_{3'3'}(f)$ that are used to compute the quantity $N_{0,3'3'}$ and, finally, apply Eq. (8.3) to determine $E[\max \sigma_{\mathrm{Z'Z'}}(t)]$. This sequence should be repeated for any pair (ϕ, θ) to find the solutions of maximum. Various solutions (ϕ^*, θ^*) may also exist because of periodicity of trigonometric functions in matrix $\mathbf{R}(\phi, \theta, \psi)$. The pair (ϕ^*, θ^*) implies one solution among those periodic ones.

The next step is to scan the angle ψ (in interval $0 \leq \psi \leq 2\pi$) since angles ϕ^* and θ^* identified the Z'-axis. The particular direction Y' (located by angle ψ^*) maximizes the variance $\lambda_{0,4'4'} = \mathrm{Var}[\tau_{\mathrm{Y'Z'}}(t)]$ of the shear stress $\tau_{\mathrm{Y'Z'}}(t)$ [VAN19]:

$$\max_{0\leq\psi\leq 2\pi}[\lambda_{0,4'4'}] = \max_{0\leq\psi\leq 2\pi}\int_0^\infty S_{4'4'}(f)\,\mathrm{d}f \tag{8.4}$$

In order to find the angle ψ^* of maximum variance, the rotated PSD matrix in Eq. (8.1) and its spectral moment $\lambda_{0,4'4'}$ should be computed for each value of ψ. Also, in this instance, the solution ψ^* may be periodic.

At this stage, the procedure provides the values of the three angles $(\phi^*, \theta^*, \psi^*)$, which permit the rotated reference frame $P_{\mathrm{X'Y'Z'}}$ to be placed, see Figure 8.2. Note that Eq. (8.1) determines the PSD matrix in the rotated frame, $\mathbf{S}^*_{\mathrm{X'Y'Z'}}(f) = \mathbf{R}(\phi^*, \theta^*, \psi^*)\, \mathbf{S}_{\mathrm{XYZ}}(f)\, \mathbf{R}(\phi^*, \theta^*, \psi^*)^{\mathrm{T}}$ by computing the rotation matrix $\mathbf{R}$ at the angle values obtained in previous steps. The asterisk means that the rotated PSD matrix $\mathbf{S}^*_{\mathrm{X'Y'Z'}}(f)$ no longer depends on the Euler angles, but only on frequency.

The axes of the reference frame $P_{\mathrm{X'Y'Z'}}$ characterize the so-called 'average principal directions' at a given point [VAN19]. For this reason, $P_{\mathrm{X'Y'Z'}}$ is also renamed as $P_{\hat{1}\hat{2}\hat{3}}$, see Figure 8.1(b).

Finally, the procedure identifies two other angles, δ and γ, by which a new reference frame P_{uvw} (attached to the critical plane) is positioned with respect to $P_{\mathrm{X'Y'Z'}}$.

Consistently with the previous notation in which an apex is used to differentiate $P_{\mathrm{X'Y'Z'}}$ from P_{XYZ}, the frame P_{uvw} may also be indicated as $P_{\mathrm{X''Y''Z''}}$, such a frame being rotated with respect to $P_{\mathrm{X'Y'Z'}}$. Consequently, the stress vector in P_{uvw} can be written as $\boldsymbol{\sigma}_{\mathrm{X''Y''Z''}}(t) = \left[\sigma_{\mathrm{x''x''}}(t), \sigma_{\mathrm{y''y''}}(t), \sigma_{\mathrm{z''z''}}(t), \tau_{\mathrm{y''z''}}(t), \tau_{\mathrm{x''z''}}(t), \tau_{\mathrm{x''y''}}(t)\right]^{\mathrm{T}}$, at the same time its PSD matrix is $\mathbf{S}_{\mathrm{uvw}}(f) = \mathbf{S}_{\mathrm{X''Y''Z''}}(f)$:

$$\mathbf{S}_{\mathrm{uvw}}(f) = \widetilde{\mathbf{R}}(\delta, \gamma)\, \mathbf{S}^*_{\mathrm{X'Y'Z'}}(f)\, \widetilde{\mathbf{R}}(\delta, \gamma)^{\mathrm{T}} \tag{8.5}$$

The power spectral matrix $\mathbf{S}^*_{\mathrm{X'Y'Z'}}(f)$ has been determined at previous steps, and the new rotation matrix is given by (see [VAN19]):

$$\widetilde{\mathbf{R}}(\delta,\gamma)=\begin{bmatrix}1&0&0&0&0&0\\0&1&0&0&0&0\\0&0&1&0&0&0\\0&0&0&1&0&0\\0&0&0&0&1&0\\0&0&0&0&0&1\end{bmatrix}$$

$$\begin{bmatrix}c_\gamma^2&s_\gamma^2&0&0&0&2c_\gamma s_\gamma\\s_\gamma^2&c_\gamma^2&0&0&0&-2c_\gamma s_\gamma\\0&0&1&0&0&0\\0&0&0&c_\gamma&s_\gamma&0\\0&0&0&-s_\gamma&c_\gamma&0\\-c_\gamma s_\gamma&c_\gamma s_\gamma&0&0&0&c_\gamma^2-s_\gamma^2\end{bmatrix} \tag{8.6}$$

$$\begin{bmatrix}1&0&0&0&0&0\\0&c_\delta^2&s_\delta^2&-2c_\delta s_\delta&0&0\\0&s_\delta^2&c_\delta^2&2c_\delta s_\delta&0&0\\0&c_\delta s_\delta&-c_\delta s_\delta&c_\delta^2-s_\delta^2&0&0\\0&0&0&0&c_\delta&s_\delta\\0&0&0&0&-s_\delta&c_\delta\end{bmatrix}$$

Matrix $\widetilde{\mathbf{R}}(\delta,\gamma)=\mathbf{I}_6\mathbf{R}_\delta\mathbf{R}_\gamma$ implies a sequence of two rotations δ and γ, specified by the product of matrices $\mathbf{R}_\delta$ and $\mathbf{R}_\gamma$. The identity matrix $\mathbf{I}_6$, becomes the two equations (8.1) and (8.5) somehow 'symmetrical' and does not produce any actual rotation.

The off-angle δ measures a clockwise rotation about the $\hat{2}$-axis (see Figure 8.2). Its actual value $\delta^*=(3\pi/8)\,[1-(\tau_{\mathrm{af}-1}/\sigma_{\mathrm{af}-1})^2\,]$ is only a function of the ratio of fully-reversed tension-compression and torsion fatigue limits, $\sigma_{\mathrm{af}-1}$ and $\tau_{\mathrm{af}-1}$ [VAN19].

The fifth angle γ is a counterclockwise rotation about the *w*-axis, see Figure 8.1(c). The method scans the interval $0 \leq \gamma \leq 2\pi$ to find that value γ^* maximizing the variance $\lambda_{0,4''4''} = \mathrm{Var}[\tau_{\mathrm{y}''\mathrm{z}''}(t)]$ of the shear stress $\tau_{\mathrm{y}''\mathrm{z}''}(t)$ [VAN19]:

$$\max_{0\leq\gamma\leq2\pi}\left[\lambda_{0,4''4''}\right] = \max_{0\leq\gamma\leq2\pi}\int_0^\infty S_{4''4''}(f)\,\mathrm{d}f \tag{8.7}$$

To search for the angle γ^* of maximum variance, the rotated PSD matrix in Eq. (8.5) and its spectral moment $\lambda_{0,4''4''}$ should be computed for each value of γ.

This final step identifies the last angle out of five angles $(\phi^*, \theta^*, \psi^*, \delta^*, \gamma^*)$, which exactly locate the reference frame $P_{\mathrm{uvw}} = P_{\mathrm{X}''\mathrm{Y}''\mathrm{Z}''}$, and the critical plane linked to it.

The stress vector is $\boldsymbol{\sigma}_{\mathrm{X}''\mathrm{Y}''\mathrm{Z}''}(t)$ and its PSD matrix is $\mathbf{S}^*_{\mathrm{X}''\mathrm{Y}''\mathrm{Z}''}(f)$ in frame P_{uvw}. Following a sequence of five successive rotations, this spectral matrix can be expressed by a relationship comparable with the Eq. (8.5):

$$\mathbf{S}^*_{\mathrm{X}''\mathrm{Y}''\mathrm{Z}''}(f) = \widetilde{\mathbf{R}}(\delta^*,\gamma^*)\,\mathbf{R}(\phi^*,\theta^*,\psi^*)\,\mathbf{S}_{\mathrm{XYZ}}(f)\,\mathbf{R}(\phi^*,\theta^*,\psi^*)^T\,\widetilde{\mathbf{R}}(\delta^*,\gamma^*)^{\mathrm{T}} \tag{8.8}$$

in which $\mathbf{S}^*_{\mathrm{X}'\mathrm{Y}'\mathrm{Z}'}(f)$ is written explicitly as in Eq. (8.1). Matrix $\mathbf{R}(\phi^*,\theta^*,\psi^*)$ merges the first three rotations, matrix $\widetilde{\mathbf{R}}(\delta^*,\gamma^*)$ the last two. Again, the asterisk identifies constant values and, more precisely, implies that $\mathbf{S}^*_{\mathrm{X}''\mathrm{Y}''\mathrm{Z}''}(f)$ no longer depends on rotation angles, but only on frequency f.

If the matrix product in Eq. (8.8) were computed, the resulting long expression would show that each element in $\mathbf{S}^*_{\mathrm{X}''\mathrm{Y}''\mathrm{Z}''}(f)$ is merely a linear summation of power spectral densities in $\mathbf{S}_{\mathrm{XYZ}}(f)$, multiplied by trigonometric functions of the five rotation angles.

In fact, the CSV criterion does not consider all the elements in $\mathbf{S}^*_{\mathrm{X}''\mathrm{Y}''\mathrm{Z}''}(f)$, but it linearly combines only two power spectra, $S_{3''3''}(f)$ and $S_{4''4''}(f)$, and postulates that the quantity $S_{\mathrm{eq}}(f) = S_{3''3''}(f) + (\sigma_{\mathrm{af}-1}/\tau_{\mathrm{af}-1})S_{4''4''}(f)$ represents the one-sided PSD

of an equivalent stationary Gaussian random stress $\sigma_{\mathrm{eq}}(t)$ linked to the critical plane [VAN19]. The equivalent power spectrum appears not to have an unambiguous definition, since alternative expressions that combine other elements of $\mathbf{S}^{*}_{\mathrm{X''Y''Z''}}(f)$ are given in other References [CAR14,CAR16,VAN18].

Conceived this way, the criterion transforms a 6×6 spectral matrix $\mathbf{S}_{\mathrm{XYZ}}(f)$ into one single power spectrum $S_{\mathrm{eq}}(f)$ in the frequency-domain. In the time-domain, it is equivalent to transform the multiaxial stress $\boldsymbol{\sigma}_{\mathrm{XYZ}}(t)$ into the equivalent uniaxial stress $\sigma_{\mathrm{eq}}(t)$.

The CSV criterion then assumes that the fatigue damage of $\boldsymbol{\sigma}_{\mathrm{XYZ}}(t)$ is equivalent to that of $\sigma_{\mathrm{eq}}(t)$. The expected damage of $\sigma_{\mathrm{eq}}(t)$ can be estimated directly from $S_{\mathrm{eq}}(f)$ by making use of uniaxial spectral methods (like Tovo-Benasciutti method, Dirlik, single-moment, etc.). For more details, see for example [BEN06,BEN18b].

8.2.2 The CSV method in numerical computations

The steps described previously have been deduced from [CAR14,CAR16,VAN18, VAN19]. After choosing a set of angles defining a rotated plane, the procedure first needs the rotated PSD matrix, from which it can compute those moments ($\lambda_{0,3'3'}$, $\lambda_{2,3'3'}$, $\lambda_{0,4'4'}$, $\lambda_{0,4''4''}$) necessary to calculate the maximum variance or expected largest peak for that particular set of angles previously selected. The maximum value (variance or peak) is stored. Then, calculation moves to the next set of angles, until all the material planes passing through a point are scanned. The largest value among all stored maxima identifies the direction or the critical plane.

In numerical calculations where angles take on discrete values, the above procedure should be repeated along with a high number of angular combinations. This task can only be achieved by using 'for/end' loops in which, at each iteration, a discrete value is assigned to every angle and the resulting maximum computed. The whole largest

maximum (variance or expected peak) can be identified over its corresponding angles, once all the digitalized angles have been scanned and the corresponding maximum stored.

Note that the use of 'for/end' loops is necessary because there is no possibility to get directly the closed-form expression of the power spectral density, whose spectral moments are used to compute the variance and the largest peak for a particular plane orientation. The whole PSD matrix and its moments should be computed before any of such calculations.

The structure of a possible numerical algorithm written in Matlab is sketched in Figure 8.2. It reflects the steps summarized above. Two nested 'for/end' loops are required to find the angles (ϕ^*, θ^*) in one go. A sequence of other two loops return first ψ^* and then γ^*, while δ^* is a one-line function of fatigue limits.

```
% read input PSD
S=...


% define vectors of angles
phi=linspace(0,2*pi,nphi);
theta=...
...


% Step 1: find theta* and phi*
for i=1:ntheta
  for j=1:nphi
    S1=R1*SXYZ*R1';
    % compute spectral moments
    ...
  end
end


% Step 2: find psi*
for i=1:npsi
    S1=R1*SXYZ*R1';
     % compute spectral moment
    ...
end


% Step3: find delta*
delta=3*pi/8*(1-(tau_af/sigma_af)^2);


% Step 4: find gamma*
for i=1:ngamma
     S2=R2*R1*SXYZ*R1'*R2';
    % compute spectral moment
    ...
end

Seq=... % compute equiv.PSD
```

Figure 8.2. Structure of Matlab routine of the standard algorithm.

Every loop has a number of iterations that depends on the number of subdivisions in each angular interval. In a single simulation run, the algorithm has a number of iterations equal to $n_\mathrm{p} = n_\phi \cdot n_\theta + n_\psi + n_\gamma$. This number also corresponds with the number of planes to be scanned. the value n_p turns out to be inversely proportional to Δ^2 (see Appendix B) if all angular intervals are subdivided with a common angular resolution Δ (which spaces two consecutive values apart). A narrow step improves the resolution in critical plane localization, but it also increases (even significantly) the number of iterations, and likewise the computation time. For example, $\Delta = 10°$ produces $n_\mathrm{p} = 777$, $\Delta = 5°$ returns $n_\mathrm{p} = 2847$, whereas $\Delta = 1°$ yields $n_\mathrm{p} = 66063$.

The algorithm requires a certain amount of memory to allocate all the scalars, vectors and matrices needed within the calculation (see the scheme in Figure 8.3). Some are computed once, other iteratively.

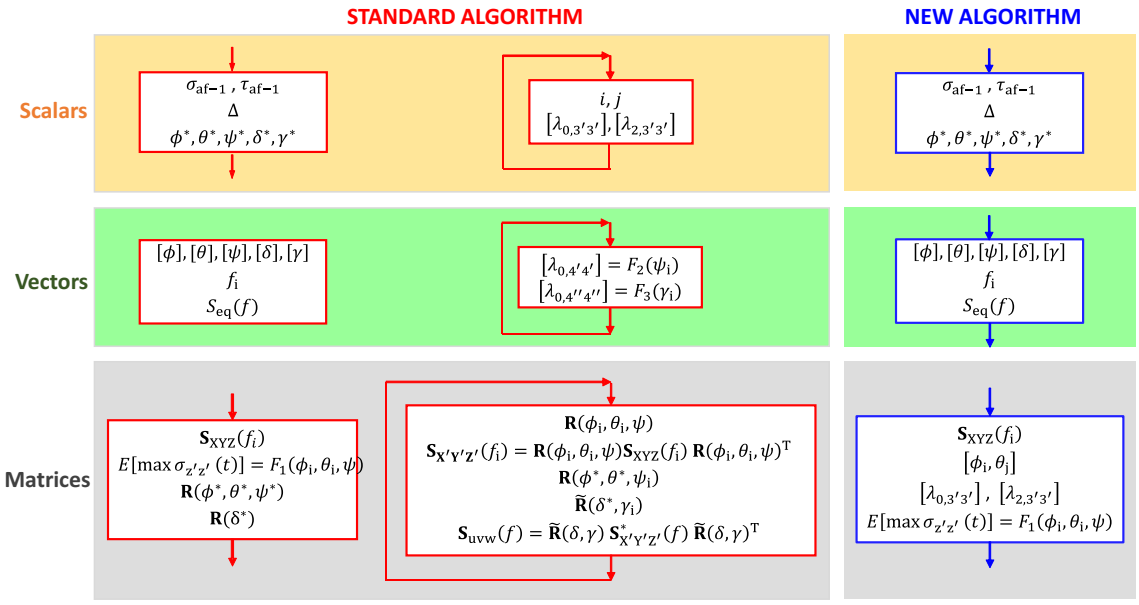

Figure 8.3. Comparison of scalars and arrays used in the two algorithms. The scheme emphasizes the difference between quantities computed once or iteratively.

In addition to the fatigue limits, discretized angular intervals and frequency axis, at the beginning the algorithm memorizes the 36 PSDs in $\mathbf{S}_{\mathrm{XYZ}}(f)$. Then, for each plane orientation defined by a pair of discretized angles ϕ_{i} $(i = 1,2,\dots,n_{\phi})$ and θ_{j} $(j = 1,2,\dots,n_{\theta})$, the algorithm should compute and memorize the three rotation matrices $\mathbf{R}_{\phi}$, $\mathbf{R}_{\theta}$, $\mathbf{R}_{\psi}$ in Eq. (8.2), all the 36 elements in the rotated PSD matrix $\mathbf{S}_{\mathrm{X'Y'Z'}}(f)$ and its corresponding set of spectral moments (one matrix for each order of spectral moment). A different $n_{\phi} \times n_{\theta}$ matrix is also needed to store the largest peak value calculated for any angle pair $[\phi_{\mathrm{i}}, \theta_{\mathrm{j}}]$. Also finding the third angle ψ^{*} requires some additional memory to allocate the matrices $\mathbf{R}_{\phi}$, $\mathbf{R}_{\theta}$, $\mathbf{R}_{\psi}$, the power spectral density $S_{4'4'}(f)$ and its zero-order moment for each discrete value ψ_{i} $(i = 1,2,\dots,n_{\psi})$. An additional matrix $\mathbf{R}_{\gamma}$ in Eq. (8.6), the power spectral matrix $\mathbf{S}_{\mathrm{X''Y''Z''}}(f)$ and the spectral moment $\lambda_{0,4''4''}$ have to be computed for each discrete value values γ_{i} $(i = 1,2,\dots,n_{\gamma})$ as a way to find the last angle γ^{*}. Despite this number of arrays, the overall memory requirement is rather small, it being only of the order of a couple of megabytes, i.e. a value tractable with no difficulty by any computer.

The algorithm in Figure 8.2 produces the critical plane only in one point. It should be repeated as many times as the points to be analyzed.

8.2.3 Critical analysis of the use of the Davenport's formula

The first two angles (ϕ^{*}, θ^{*}) of Z'-axis are determined by the Davenport's formula, Eq. (8.3), for the expected largest peak of $\sigma_{\mathrm{z'z'}}(t)$ in time T. Eq. (8.3) tends to overestimate the largest peak value in a narrow-band process, for more details see [PRE85]. This is a direct result of the assumption, upon which the formula is based, that successive peaks are independent of each other. This assumption is not verified in a narrow-band process, in which local peaks and valleys tend to 'cluster' together, because the process is somehow 'correlated'. Besides, the Davenport's formula is only a function of the central frequency ν_0 of process $\sigma_{\mathrm{z'z'}}(t)$, while it disregards its bandwidth.

However, a random process is not always narrow-band. It is then of interest to investigate whether, and how much, the angles (ϕ^*, θ^*) could be affected by the spectral bandwidth of a process $\sigma_{z'z'}(t)$ that is wide-band.

An empirical (approximate) expression was suggested in the paper of Preumont [PRE85] to correct the Davenport's formula. It presents two coefficients, κ_u and κ_α, that account for the PSD bandwidth through the Vanmarcke parameter ε.

Figure 8.4 compares the Davenport's and Preumont's equations over a range of bandwidths, for two values of T (i.e. different numbers of peaks). As is anticipated, the Davenport's equation is independent of bandwidth ε. Results from the two equations tend to overlap for $\varepsilon \geq 0.5$. At lower bandwidths, Preumont's results are lower than the Davenport's ones. For a very narrow-band process ($\varepsilon \to 0$) the difference is the largest, and reduces for higher T (note that, in this case, the time length T affects the results, and cannot be treated as a 'dummy' variable). However, the observed difference seems to be within acceptable limits. It can thus be concluded that using the Davenport formula to localize Z' results in acceptable approximations, even though the normal stress $\sigma_{z'z'}(t)$ is narrow-band.

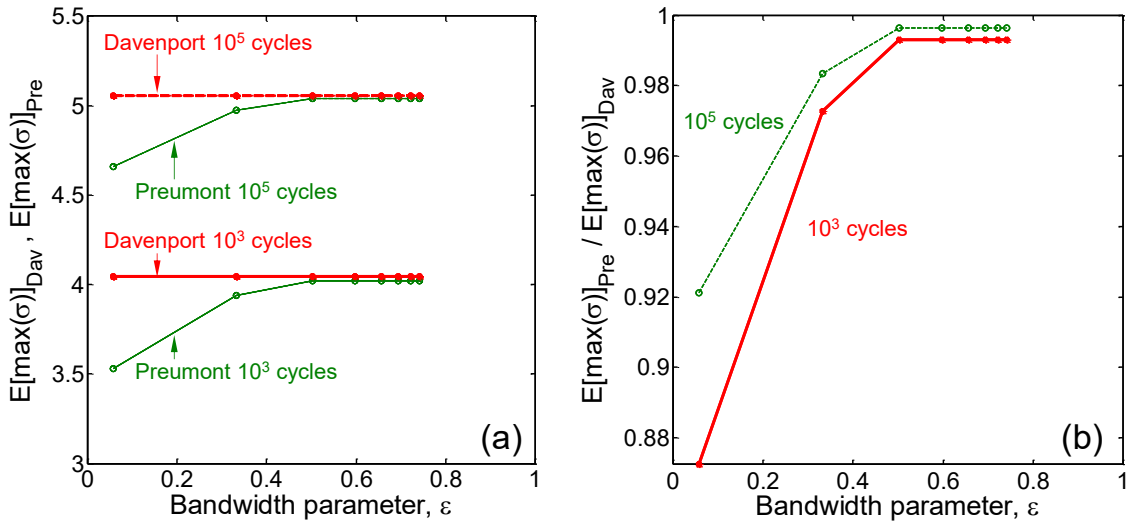

Figure 8.4. Expected largest peak in time T: comparison between the original and modified version of Davenport's formula.

8.3 THE PROPOSED ALGORITHM

In the algorithm of Figure 8.2, running the iterations in 'for/end' loops is quite time-consuming. If 'for/end' loops are replaced with the in-line functions, the algorithm can be made much faster. This task is settled by determining, first, the analytical expressions of only those spectral moments truly engaged by the CSV method, although some information on the stress signals examined is lost during such a new algorithm stage. Then, these expressions should be inserted into in-line functions to get the rotation angles for the planes with maximum variance or largest peak.

The approach is nearly trivial. It takes advantage of matrix algebra to determine the expressions of selected spectral moments in any rotated reference frame. For example, considering Eq. (8.3) used to determine the axis Z'. It only utilizes the spectral moments $\lambda_{0,3'3'}$ and $\lambda_{2,3'3'}$ at position 33 in matrix $\boldsymbol{\lambda}_{\mathrm{m,X'Y'Z'}}$ relating to the rotated reference frame $P_{\mathrm{X'Y'Z'}}$. The first step is to apply Eq. (8.1) to the spectral matrix $\mathbf{S}_{\mathrm{X'Y'Z'}}(f)$ in Eq. (8.2) to obtain the 6×6 spectral moment matrix:

$$\boldsymbol{\lambda}_{\mathrm{m,X'Y'Z'}} = \mathbf{R}(\phi,\theta,\psi)\,\boldsymbol{\lambda}_{\mathrm{m,XYZ}}\,\mathbf{R}(\phi,\theta,\psi)^{\mathrm{T}} \tag{8.9}$$

Then, to extract only the elements in position 33, an auxiliary vector $\mathbf{a_3} = [0 \quad 0 \quad 1 \quad 0 \quad 0 \quad 0]^{\mathrm{T}}$ is used for pre- and post-multiplies the matrix $\boldsymbol{\lambda}_{\mathrm{m,X'Y'Z'}}$:

$$\lambda_{\mathrm{m},3'3'} = \mathbf{a_3}\,\mathbf{R}(\phi,\theta,\psi)\,\boldsymbol{\lambda}_{\mathrm{m,XYZ}}\,\mathbf{R}(\phi,\theta,\psi)^{\mathrm{T}}\,\mathbf{a}_{\mathbf{3}}^{\mathrm{T}} \tag{8.10}$$

The subscript stipulates that $\mathbf{a_3}$ has a unit value in position 3 and zero value elsewhere.

Eq. (8.10) should be solved twice to find the zero and second order moments $\lambda_{0,3'3'}$, $\lambda_{2,3'3'}$. If performed by hand, this calculation is quite laborious, but it becomes much simpler and faster if performed with the aid of numerical software (as Matlab Symbolic [MAT18]). No surprise that very long expressions are obtained for both $\lambda_{0,3'3'}$ and $\lambda_{2,3'3'}$. As an example, the full-length expression of $\lambda_{0,3'3'}$ is described as:

$$\begin{aligned}
\lambda_{0,3'3'} &= c_\phi^4 s_\theta^4 \lambda_{0,11} + s_\phi^4 s_\theta^4 \lambda_{0,22} + c_\theta^4 \lambda_{0,33} + 4c_\theta^2 s_\phi^2 s_\theta^2 \lambda_{0,44} \\
&+4c_\phi^2 c_\theta^2 s_\theta^2 \lambda_{0,55} + 4c_\phi^2 s_\phi^2 s_\theta^4 \lambda_{0,66} + 2c_\phi^2 s_\phi^2 s_\theta^4 \lambda_{0,12} + 2c_\phi^2 c_\theta^2 s_\theta^2 \lambda_{0,13} \\
&+4c_\phi^2 c_\theta s_\phi s_\theta^3 \lambda_{0,14} - 4c_\phi^3 c_\theta s_\theta^3 \lambda_{0,15} + 4c_\phi^3 s_\phi s_\theta^4 \lambda_{0,16} + 2c_\phi^2 s_\phi^2 s_\theta^2 \lambda_{0,23} \\
&+4c_\theta s_\phi^3 s_\theta^3 \lambda_{0,24} - 4c_\phi c_\theta s_\phi^2 s_\theta^3 \lambda_{0,25} + 4c_\phi s_\phi^3 s_\theta^4 \lambda_{0,26} + 4c_\theta^3 s_\phi s_\theta \lambda_{0,34} \\
&-4c_\phi c_\theta^3 s_\theta \lambda_{0,35} + 4c_\phi c_\theta^2 s_\phi s_\theta^2 \lambda_{0,36} - 8c_\phi c_\theta^2 s_\phi s_\theta^2 \lambda_{0,45} + 8c_\phi c_\theta s_\phi^2 s_\theta^3 \lambda_{0,46} \\
&-8c_\phi^2 c_\theta s_\phi s_\theta^3 \lambda_{0,56}
\end{aligned} \tag{8.11}$$

where $\lambda_{0,\mathrm{ij}}$ represent the spectral moments of $\mathbf{S}_{\mathrm{XYZ}}(f)$, and c_x, s_x stand for sine and cosine of x. Note that there are 6 variances λ_(0,ii) and, due to the symmetry of the covariance matrix, 15 covariances λ_(0,ij) (i≠j).

The former expression seems very complicated, but it is simply a summation of all spectral moments $\lambda_{\mathrm{m,ij}}$, each one multiplied by a coefficient:

$$\lambda_{\mathrm{m},3'3'} = \sum_{\mathrm{i}=1}^{6} \left(q_{\mathrm{ii}}(\phi,\theta,\psi)\, \lambda_{\mathrm{m,ii}}\right) + 2\sum_{\mathrm{i}=2}^{6}\sum_{\mathrm{j}<\mathrm{i}} \left(q_{\mathrm{ij}}(\phi,\theta,\psi)\, \lambda_{\mathrm{m,ij}}\right) \tag{8.12}$$

Each coefficient q_{ii}, q_{ij} is a trigonometric function of (ϕ,θ,ψ). The summation (8.12) forms a total of 21 terms.

The formulae of $\lambda_{0,3'3'}$ and $\lambda_{2,3'3'}$ can be used to calculate, via numerical software, the expression of $N_{0,3'3'} = T\sqrt{\lambda_{2,3'3'}/\lambda_{0,3'3'}}/2\pi$. By this computational artifice, all preceding formulae can be gathered together to obtain the symbolic expression of $E[\max \sigma_{\mathrm{z'z'}}(t)] = F_1(\phi,\theta,\psi)$ in Eq. (8.3) as a function of angles (ϕ,θ,ψ). This expression can then be copy-pasted from a symbolic software tool into a script for double-precision computation.

If Matlab is used, some powerful functions can be exploited. When Eq. (8.3) is being solved to locate Z', only two values ϕ^*, θ^* should be found in the intervals $0 \leq \phi \leq 2\pi$, $0 \leq \theta \leq \pi$. Again, ψ does not need to be considered (therefore, it may be assumed to be equal to zero). If angles ϕ, θ are assigned by the evenly-spaced discrete values ϕ_{i} $(i = 1,2, \dots, n_{\phi})$ and θ_j $(j = 1,2, \dots, n_{\theta})$, Matlab command 'meshgrid' is used to create a two-dimensional grid of points $[\phi_{\mathrm{i}}, \theta_{\mathrm{j}}]$ at each of which $E[\max \sigma_{z'z'}(t)] = F_1(\phi, \theta, \psi)$ can be computed. This grid of points has dimension $n_{\phi} \times n_{\theta}$. The output of $F_1(\phi_{\mathrm{i}}, \theta_{\mathrm{j}}, \psi)$ is then stored in a two-dimensional $n_{\phi} \times n_{\theta}$ matrix. Searching the largest maximum (or the largest maxima in case of periodic solutions) – with the command 'find' – allows the indexes to be identified immediately, and thus the corresponding values, of the solution angles (ϕ^*, θ^*). The obtained indexes correspond to a specific element in matrix $[\phi_{\mathrm{i}}, \theta_{\mathrm{j}}]$. At this stage, the algorithm returns the first two angles (ϕ^*, θ^*).

Indeed, the algorithm in Figure 8.5 follows a more clever and efficient approach, which invokes the element-wise Hadamard multiplication in Matlab (see operator .*). First, the exact expressions of spectral moments $\lambda_{0,3'3'}$ and $\lambda_{2,3'3'}$, obtained by Eq. (8.12), are directly computed at the two-dimensional array $[\phi_{\mathrm{i}}, \theta_{\mathrm{j}}]$ created as before, and this transforms both spectral moments into two-dimensional arrays $[\lambda_{0,3'3'}]$, $[\lambda_{2,3'3'}]$. Following Eq. (8.3), these two arrays are organized and multiplied element-by-element to obtain directly the two-dimensional array $F_1(\phi_{\mathrm{i}}, \theta_{\mathrm{j}}, \psi)$. The maximum is found exactly as before.

```
% read input PSD
S=...


% define vectors of angles
phi=linspace(0,2*pi,nphi);
theta=...
...

% Step 1: find theta* and phi*
[PHIm,THETAm] = meshgrid(PHI,THETA);
m0zzRot=C_THETA.^4.*Vzz+C_PHI.^4.*S_THETA.^4.* Vxx+...
m2zzRot=C_THETA.^4.*m2zz+C_PHI.^4.*S_THETA.^4.*m2xx+...
N1=(sqrt(m2zzRot./mzzRot).*T)./(2.*pi);
ESzz=sqrt(mzzRot).*(sqrt(2.*log(N1))+0.5772./sqrt(2.*log(N1)));
[maxESzz,imaxZZ]=max(ESzz(:));% find maximum
...
...

% Step 2: find psi*
myzRot=C_PSI.^2.*C_phi.^2.*C_theta.^2.* Vyz+...
[maxVarYZ,imax3] = max(myzRot(:));



% Step3: find delta*
delta=3*pi/8*(1-(tau_af/sigma_af)^2);

% Step 4: find gamma*
MVW_Rot=C_GAMA.^2.*C_delta.^2.*C_theta.^4.*S_delta.^2.* Vzz+
C_GAMA.^2.*C_delta.^2.*C_psi.^4.*S_delta.^2.*S_phi.^4.* Vxx+...
gama_maxVarVW  = GAMA(imaxVW);


Seq=... % compute equiv.PSD
```

Figure 8.5. Structure of Matlab routine of the new algorithm.

In any case, the matrices created by the 'meshgrid' command are not so vast since their dimensions depend on the number of discrete points n_ϕ, n_θ defining each discretized angular interval. For example, a very fine discretization of 1° yields a grid $n_\phi \times n_\theta = 361 \times 361$ of evenly-spaced points, which Matlab can store without much effort or particular memory requirement.

Since the first two values (ϕ^*, θ^*) have been determined, the next step is to determine the angle ψ^* maximizing the zero-order moment $\lambda_{0,4'4'}$ in Eq. (7). This spectral moment is the position 44 in matrix $\boldsymbol{\lambda}_{\mathrm{m,X'Y'Z'}}$. A different auxiliary vector $\mathbf{a_4}$ (with unit value in position 4) in Eq. (8.10) determines the spectral moment $\lambda_{0,4'4'}$:

$$\lambda_{0,4'4'} = \mathbf{a_4}\, \mathbf{R}(\phi^*, \theta^*, \psi)\, \boldsymbol{\lambda}_{\mathrm{m,XYZ}}\, \mathbf{R}(\phi^*, \theta^*, \psi)^{\mathrm{T}}\, \mathbf{a_4^{\mathrm{T}}} \tag{8.13}$$

Without much effort, a software would return a pretty long analytical expression, quite similar to Eq. (8.11) apart from different trigonometric coefficients q_{ij}. Another small difference is that, now, two angles take on constant values (ϕ^*, θ^*), while only the third ψ is variable. In fact, ψ signifies a rotation around axis Z', whose position has already been defined by (ϕ^*, θ^*).

The expression of $\lambda_{0,4'4'} = F_2(\psi)$ is a function of one variable ψ. If the interval $0 \leq \psi \leq 2\pi$ is divided into evenly-spaced values ψ_{i} $(i = 1,2, \dots, n_{\psi})$ at which $F_2(\psi)$ is computed, an output vector $[F_2(\psi)]$ is obtained. This vector is formed by n_{ψ} discrete points. It is simple to find the value ψ^* (with proper periodicity) for which $\lambda_{0,4'4'}$ is maximum.

After this last step, the algorithm returns the angles $(\phi^*, \theta^*, \psi^*)$ that locate the rotated reference frame $P_{\mathrm{X'Y'Z'}}$ by the rotation matrix $\mathbf{R}(\phi^*, \theta^*, \psi^*)$.

The procedure, which is followed by the angles $(\phi^*, \theta^*, \psi^*)$**,** is now used to find the angles δ^*, γ^* defining P_{uvw}. As a preliminary step, it is convenient to insert Eq. (8.1) into Eq. (8.5), so that to relate the spectral matrix $\mathbf{S}_{\mathrm{uvw}}(f)$ directly to $\mathbf{S}_{\mathrm{XYZ}}(f)$ in the fixed reference frame P_{XYZ}:

$$\mathbf{S}_{\mathrm{uvw}}(f) = \widetilde{\mathbf{R}}(\delta^*, \gamma)\, \mathbf{R}(\phi^*, \theta^*, \psi^*)\, \mathbf{S}_{\mathrm{XYZ}}(f)\, \mathbf{R}(\phi^*, \theta^*, \psi^*)^{\mathrm{T}}\, \widetilde{\mathbf{R}}(\delta^*, \gamma)^{\mathrm{T}} \tag{8.14}$$

The PSD matrix in Eq. (8.14) denotes to that specific rotated frame which is positioned by the four angles $(\phi^*, \theta^*, \psi^*, \delta^*)$. The off-angle δ^* is also included, it being at once known from fatigue limits. Matrix $\mathbf{S}_{\mathrm{uvw}}(f)$ is merely a function of both angle γ and frequency f. The definition of $\boldsymbol{\lambda}_{\mathrm{m,XYZ}}$ (see Chapter 2) applied to Eq. (8.14) provides the matrix of m-th order spectral moments of $\mathbf{S}_{\mathrm{uvw}}(f)$:

$$\boldsymbol{\lambda}_{\mathrm{m,uvw}} = \widetilde{\mathbf{R}}(\delta^*, \gamma)\, \mathbf{R}(\phi^*, \theta^*, \psi^*)\, \boldsymbol{\lambda}_{\mathrm{m,XYZ}}\, \mathbf{R}(\phi^*, \theta^*, \psi^*)^{\mathrm{T}}\, \widetilde{\mathbf{R}}(\delta^*, \gamma)^{\mathrm{T}} \tag{8.15}$$

Remind that $\mathbf{S}_{\mathrm{uvw}}(f)$ and $\boldsymbol{\lambda}_{m,\mathrm{uvw}}$ are equivalently notated as $\mathbf{S}_{\mathrm{X''Y''Z''}}(f)$ and $\boldsymbol{\lambda}_{\mathrm{m,X''Y''Z''}}$.

Matrix $\boldsymbol{\lambda}_{\mathrm{m,uvw}}$ is a one-variable function of γ. The CSV method is only interested in the zero-order moment $\lambda_{0,4''4''}$, which lies in position 44. Once again, it is possible to extract the $\lambda_{0,4''4''}$ by multiplying $\boldsymbol{\lambda}_{\mathrm{m,uvw}}$ with the auxiliary vector $\mathbf{a_4}$ as $\lambda_{0,4''4''} = \mathbf{a_4}\,\widetilde{\mathbf{R}}(\gamma)\,\mathbf{R}\,\boldsymbol{\lambda}_{\mathrm{m,XYZ}}\mathbf{R}^{\mathrm{T}}\,\widetilde{\mathbf{R}}(\gamma)^{\mathrm{T}}\,\mathbf{a_4^{\mathrm{T}}}$ (for more clarity, only the explicit dependence on γ has been written).

A software for symbolic calculus would compute the (rather long) analytical expression of $\lambda_{0,4''4''} = F_3(\gamma)$ with no effort. It is not a short and easy-to-handle expression at all, although it is merely a summation very similar to that written in Eq. (8.12).

In the numerical algorithm, the interval $0 \leq \gamma \leq 2\pi$ is discretized into equally-spaced values γ_{i} $(i = 1,2, \dots, n_{\gamma})$ at which $F_3(\gamma)$ is computed – the output is stored into the vector $[F_3(\psi)]$, which is formed by n_{γ} points. It is then almost trivial to find the solution γ^* (with periodicity) that corresponds to the maximum $\max[F_3(\gamma)]$.

After this final step, the new algorithm provides the five angles $(\phi^*, \theta^*, \psi^*, \delta^*, \gamma^*)$ and stops. Such an algorithm, sketched in Figure 8.5, does not use 'for/end' loops.

Figure 8.3 compares the several types of scalars and arrays used in the two algorithms; some types appear in both versions. The new algorithm makes use of larger matrices than the standard one, especially those created by the ‘meshgrid’ command. For example, to find the angles (ϕ^*, θ^*) it requires a few $n_{\phi} \times n_{\theta}$ matrices for the spectral moments $\left[\lambda_{0,3'3'}\right]$ and $\left[\lambda_{2,3'3'}\right]$, and a matrix into which to save the calculated largest peak $F_1\left(\phi_{\mathrm{i}}, \theta_{\mathrm{j}}, \psi\right)$ for each angle pair $\left[\phi_{\mathrm{i}}, \theta_{\mathrm{j}}\right]$, before searching for the highest maximum. By contrast, to find the angles ψ^* and γ^* the new algorithm only needs two vectors into which allocate the variance computed for each angular value ψ_{i} and γ_{i}.

Big matrices leads to a larger memory requirement, which is almost doubled compared to that required by the standard algorithm, although it still remains pretty small and of the order of a few megabytes (just to provide some figures, 4.3 MB versus 2.2 MB).

After implementing Matlab routines, some tests have been conducted with different types of stress PSD matrices to confirm that the new algorithm returned the same output as the standard algorithm.

8.4 NUMERICAL SIMULATIONS

Two numerical examples are employed as benchmark to compare the computation time of the standard algorithm with that of the new algorithm. The first example applies the algorithm to only one stress PSD (one simulation run), whereas the second one applies the algorithm as many times as the number of nodal stress PSDs in a finite element model (multiple simulation runs). In both examples, a normal-to-shear ratio of fatigue limits $\sigma_{af-1}/\tau_{af-1} = \sqrt{3}$ is chosen (anyway, the choice of other ratios does not affect the computation time).

As said previously, that trigonometric functions in matrices $\mathbf{R}(\phi, \theta, \psi)$ and $\widetilde{\mathbf{R}}(\delta, \gamma)$ return periodic solutions at which the same maximum is achieved. An example is displayed in Figure 8.6. In numerical simulations, only one solution has been stored among those periodic.

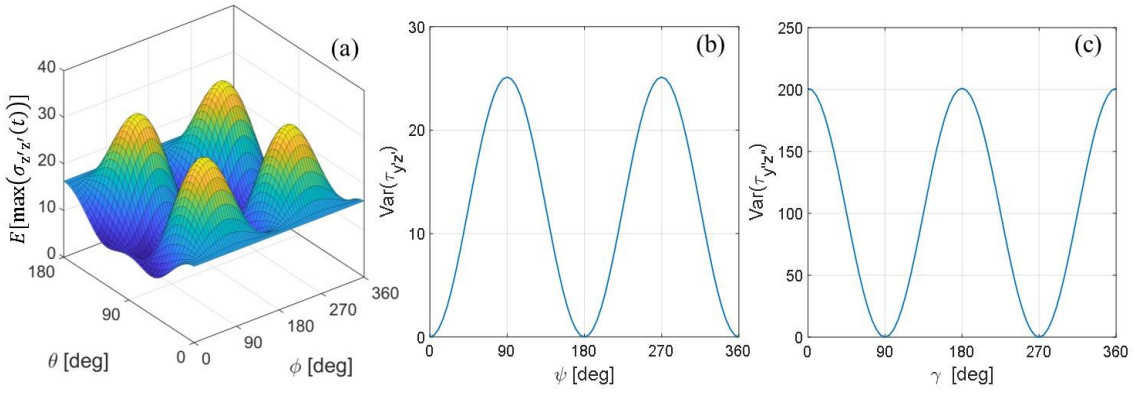

Figure 8.6. Periodicity of solutions: (a) expected largest peak of $\sigma_{z'z'}(t)$ against (ϕ, θ); (b) $\mathrm{Var}[\tau_{y'z'}(t)]$ as function of ψ; (c) $\mathrm{Var}[\tau_{y''z''}(t)]$ as function of γ.

8.4.1 Idealized power spectra (one single simulation run)

The idealized spectrum example denotes to uncorrelated normal and shear stresses, with narrow-band rectangular PSD centered at 30 Hz. The covariance matrix $\mathbf{C}_{\mathrm{XYZ}}$ has non-zero on the main diagonal $\lambda_{0,11} = 20$, $\lambda_{0,22} = 40$, $\lambda_{0,33} = 60$, $\lambda_{0,44} = 200$ (MPa^2 units), at the same time all the other elements are zero. The PSD matrix $\mathbf{S}_{\mathrm{XYZ}}(f)$ is diagonal, too. The frequency axis of all power spectra is discretized into 200 points.

Five angular resolutions (Δ=1°, 5°, 10°, 20°, 30°) are considered to measure how much Δ influences the computation time needed by each algorithm to search for the critical plane. The different resolutions investigate here whether – and how much – the equivalent spectrum $S_{\mathrm{eq}}(f)$ changes with Δ. Of course, the larger resolutions (Δ=10°, 20°, 30°) are very coarse for practical applications and have been included to make the analysis the most comprehensive.

The value of Δ make available the number of points and the size of the vectors defining each discretized angular interval (see Appendix B), which in turn determines the size of the matrices created by the 'meshgrid' command. Even for the smallest value Δ=1°, the dimension of such matrices (361×361 points) is stored by Matlab without any memory requirement.

For each value of Δ, both the standard and new algorithm are applied to the same matrix $\mathbf{S}_{\mathrm{XYZ}}(f)$ to compute the rotations angles $(\phi^*, \theta^*, \psi^*, \delta^*, \gamma^*)$ and the equivalent spectrum $S_{\mathrm{eq}}(f)$ for the critical plane in one simulation run. The algorithms obviously return the same output.

Each simulation registers the time required for each algorithm to find the critical plane. This elapsed time is exhibited in Figure 8.7(a) as a function of the number of planes n_{p} scanned by the standard algorithm (n_{p} is roughly proportional to $1/\Delta^2$). In the graph, the lines between adjacent markers are drawn only to better display the trends, and they do not stand for computed values.

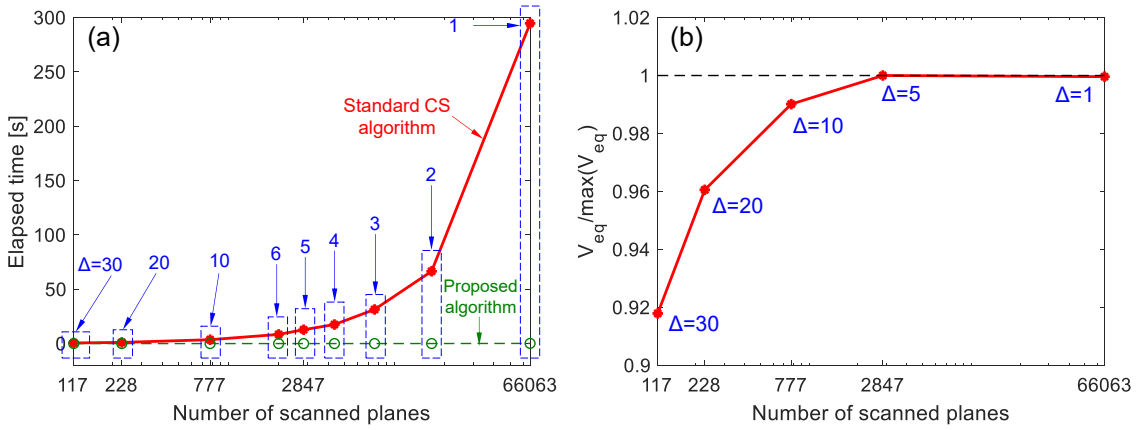

Figure 8.7. Trend of (a) computation time and (b) normalized variance $V_{eq}/V_{eq,max}$ as a function of the number of scanned planes (log scale) and angular resolution Δ.

If the resolution is narrowed from Δ=30° to Δ=1°, the computation time of the standard algorithm differs from about half a second to 300 seconds (5 minutes). The time doubles or, at most, triples for resolutions from Δ=30° down to 3°. Instead, it extends of about an order of magnitude (from 32 up to 300 seconds) if the resolution is reduced from 3° down to 1°. This large increase is easily explained by the fact that a decrease of one third in resolution makes the number of scanned planes increase of 9 times (from 7623 to 66063).

In contrast to the standard version, the new algorithm has a computation time that changes very little with the angular resolution (the green dashed line in Figure 8.7(a) is almost horizontal) and remains always very small (at most, few tenths of a second) even for the smallest resolution.

Figure 8.7(a) emphasizes how the new algorithm is faster than the standard one (especially at the smallest values of Δ) and allows a significant time saving for small values of Δ. However, the use of the smallest angular resolutions could be not necessary. As the resolution becomes smaller and smaller, the critical plane position is found with ever increasing precision. The critical plane tends to the exact position where the fatigue damage can be exact. At larger resolutions, the critical plane position – and the damage

accordingly – become increasingly more approximated. Examining how much the variance of the equivalent stress $V_{\mathrm{eq}} = \mathrm{Var}\left[S_{\mathrm{eq}}(f)\right]$ varies against Δ may ascertain the minimum angular resolution needed to obtain a good approximation of fatigue damage. This parameter has indeed a key role in spectral methods, as the expected fatigue damage $E[D(T)]$ (see Chapter 3) is proportional to the variance as $E[D(T)] \propto \left(\sqrt{V_{\mathrm{eq}}}\right)^{k}$.

Figure 8.7(b) presents the trend of V_{eq} versus Δ (the values are normalized to the largest maximum $V_{\mathrm{eq,max}}$ reached for 1°). The variance V_{eq} does not seem to change enormously with Δ, indeed, the difference is less than 10% throughout the angular resolutions explored. This implies that even a value Δ=5° would be sufficient to obtain a correct damage estimate. However, the results in Figure 8.7(b) cannot be generalized. If other types of stress PSD matrix were analyzed, other trends (not monotonic) would be observed. Obviously, the use of the smallest angular resolutions will always provide the minimum degree of approximation.

8.4.2 Finite element analysis (multiple simulation runs)

The previous example demonstrates a somehow hypothetical situation. Indeed, the standard algorithm is applied to only one stress PSD matrix, which is presumed to be the most critical point in a component or structure. However, the critical point is not always known in advance and, so, all the nodes of a finite element model used to idealize the structure have to be analyzed. This is exactly the situation in which the new algorithm works better than the standard one, while the advantages are insignificant in other cases.

As proposed by [PIT01], a finite element (FE) spectral analysis of an L-shaped structure is now discussed. Though very simple, this example could be a typical CAE durability analysis. The FE model in Figure 8.8(a) is constituted by the 4-node 'shell' elements (Mindlin-Reissner theory) organized in a free mesh.

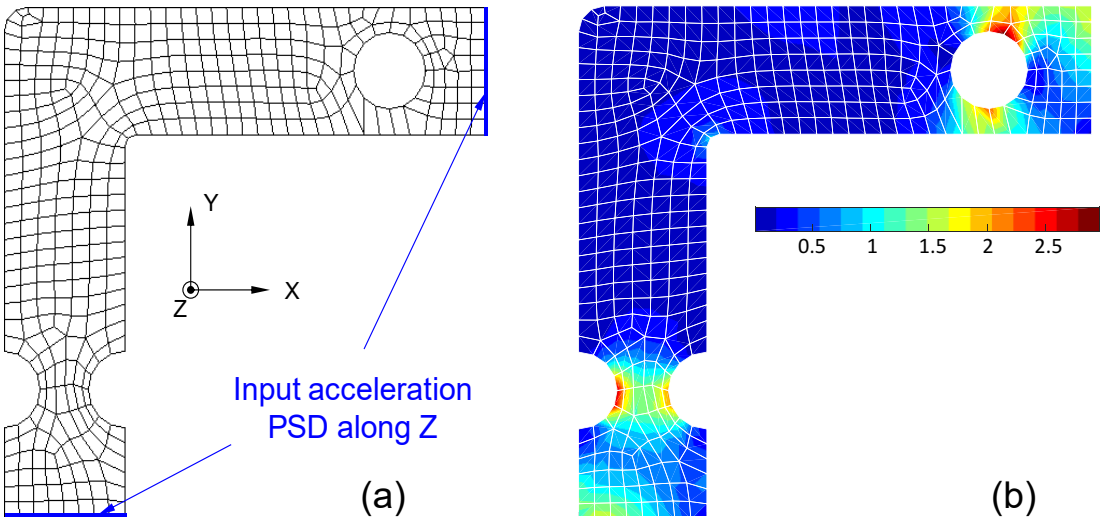

Figure 8.8. (a) Shell finite element model used in the numerical example; (b) Contour plot of the variance V_{eq} (log scale)

The typical element size of 6.5 mm provides a total of 394 elements and 469 nodes. Band-limited random accelerations are applied at both ends and perpendicular to the structure plane. The stress PSD matrix at each node is determined by a spectral

analysis. The analysis output is a set of nodal stress PSDs ($\mathbf{S}_{XYZ}^{(j)}(f)$, j=1, 2,…, 469). The frequency axis of every PSD is discretized into 1247 discrete points in the range $0 \leq f \leq$ 200 Hz, see [BEN18a,BEN19b] for more details.

Figure 8.8(b) presents the contour plot of the variance V_{eq} (in log scale) through Δ=1°. The critical nodes where the variance is maximum are located at the hole and notch. Figure 8.9 compares the computation time for various Δ values and different numbers of iterations, n_{runs}. Compared with the previous example, now the computation time of one simulation run is higher because of a larger number of points in the frequency axis (1247 vs 200).

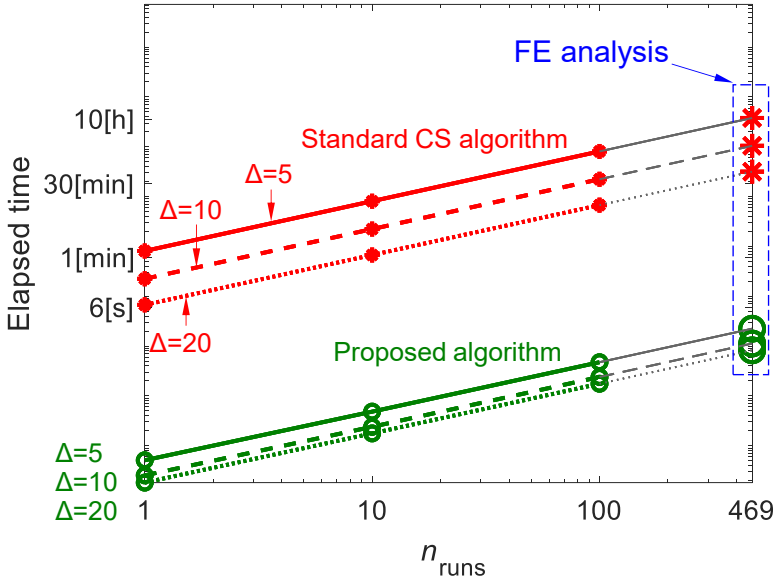

Figure 8.9. (a) Contour plot of the variance V_{eq} (log scale); (b) elapsed time for multiple simulation runs.

Indeed, only the results on the right side (n_{runs}=469 nodes) are consistent with the analysis of nodal PSD results of the model in Figure 8.8(a). The other results in center-left side of the figure (n_{runs}=1, 10, 100) correspond to Matlab simulations that iterated the algorithm a specific number of times. The aim is to mimic FE analyses with a number of nodes lower than 469. Moreover, using such a small number of nodes in the model of

Figure 8.8(a) would have produced a mesh too coarse to get meaningful stress results. In Matlab simulations, the stress PSD has the same frequency discretization as in FE analysis.

The relationship between the computation time and n_{runs} is a straight line (the figure uses a log-log scale only to enlarge the bottom-left region) for a given value of Δ. A change of Δ moves the line upward or downward.

A fitting expression is simple to derive. For the standard algorithm, the elapsed time can be approximated by the expression $T_{\mathrm{std}} \cong (A_{\mathrm{PC}}\, n_{\mathrm{f}}\, n_{\mathrm{runs}})/\Delta^2$, where n_{f} is the number of frequency points (n_{f}=1247 in this example). Constant A_{PC} depends on the specific computer characteristics. More details are provided in Appendix B. The highlighted reduction of computation time appears clearly in Figure 8.9(b) by the new algorithm. If all nodes of the finite element model are analyzed in the case of Δ=5°, the standard algorithm operates for 37900 seconds (10 hours), whereas the standard algorithm terminates in as little as 2.2 seconds.

Chapter 9

CONCLUSIONS

This thesis addresses structural durability analysis with random loadings, which are commonly observed in structure and mechanical components in service. Attention manly focuses on the variability of the fatigue damage in both Gaussian and non-Gaussian random loadings, statistical methods to verify the stationarity, confidence interval of damage with one or few time-histories and last, but not least a new algorithm to shorten the computation time of Carpinteri-Spagnoli-Vantadori (CSV) multiaxial spectral method.

An original contribution related to the variance of fatigue damage in Gaussian random loadings has been introduced in Chapter 4. Explicit formulas from the literature (Mark and Crandall, Bendat, Madsen et al. and Low) were reviewed and compared with Monte Carlo simulation results in the both time- and the frequency-domain. The sample statistics (mean, standard deviation, coefficient of variation) were determined for the fatigue damage in both time- and frequency domain, and then compared to the estimations provided by the explicit formulas. A perfect agreement resulted, at least for the specific power spectrum type for which each of the formulas applies. Results also showed that the scatter around the expected damage reduces as the time-history length increases. It was also observed how the coefficient of variation of damage (CoV) is a smooth monotonic

function of bandwidth parameter α_1, a feature that permitted a best-fitting expression to be proposed and then calibrated on the results of each power spectral density (PSD) considered individually, as well as on the results of all power spectra merged together. Not only are the proposed expressions simple and easy to be used in practice, but they also agree with time-domain simulation results.

These proposed expressions are the only ones to relate the variance of the fatigue damage directly to a bandwidth parameter α_1. Also, if performed by hand, the calculation of CoV using explicit formulas from the literature (e.g. Madsen et al., Low) is rather laborious, but it becomes much simpler and faster if performed with proposed best-fitting expressions. It is also important to emphasize the wide range of applicability of proposed formulas varying from narrow-band to wide-band processes. In fact, there was no solution to tackle the case of a wide-band process.

The thesis has also contributed with two theoretical models for assessing the variance of the fatigue damage in stationary non-Gaussian random processes (Chapter 5). The non-Gaussian models extend two methods existing in the literature (Madsen et al., Low's) that are valid for Gaussian narrow-band processes. The two models here developed apply to any non-Gaussian process for which its narrow-band power spectral density, skewness and kurtosis coefficients are known. They exploit the properties of a time-independent non-linear transformation that establishes a relationship between Gaussian and non-Gaussian domains.

Monte Carlo numerical simulations in time-domain approach were used to verify the correctness of the proposed two models and to identify typical trends. The statistics (mean value, standard deviation, coefficient of variation) characterizing the sample of computed damage values were compared to theoretical estimations. A perfect matching was observed. The results also demonstrated that, in the non-Gaussian case, the fatigue damage has a higher variance compared to the Gaussian case. This result is of particular importance as it confirms that the inappropriate use of Gaussian models with non-

Gaussian processes leads to unsafe predictions, as they neglect non-Gaussian effects. The use of the non-Gaussian models proposed is then recommended.

It is useful to underline that the methods to estimate the variance of the fatigue damage existing in the literature up till now are valid for Gaussian only. However, non-Gaussian random loadings acting on mechanical structures are usually encountered, for example, structures subject to wind or wave loadings, or an offshore platform combining structural nonlinearity with non-Gaussian input excitation. As a consequence, proposed theoretical models to estimate the variance of the fatigue damage in non-Gaussian case become fairly important in many engineering applications. In addition, the proposed non-Gaussian models have a quite accurate estimations and they are supported by a theoretical background.

As the previously proposed methods to assess the variance of the fatigue damage require that the random load is indeed stationary, attention focuses on the statistical methods to identify stationary and non-stationary loadings.

Another original contribution addressed in this thesis is the non-parametric statistical method (e.g. run test) to verify the stationarity of time-histories with finite time length. In summary, the non-parametric run test method takes a sequence of non-overlapping blocks. For each block, a value is calculated for the statistical parameter under investigation. The Rouillard's approach takes into account the root-mean-squared (RMS) values for each independent block as the statistical parameters, which can detect change only in the variance and mean value of random time-history. As an alternative to Rouillard's approach, the proposed run test considers the damage values computed for each block. The proposed damage-based run test can detect changes not only in the variance and mean value of random time-history but also in the frequency content, see Chapter 6.

Viewed from loadings action on many structures and mechanical components, measured time-histories may be non-stationary, as those resulting from different wind conditions, various sea states, as well as road sequences with different surface profile characteristics. A typical example of non-stationary loadings with changes in the frequency content is a mountain-bike traveling on a track by means of various speeds.

Besides being necessary to verify if measured random loadings are indeed stationary or non-stationary, a statistical method needs to consider changes in the frequency content at least for the specific type of loading. The proposed damage-based run test is the only one up to date that takes into account change in the variance, mean value, and frequency content of a random loading.

A real-world scenario has been considered in Chapter 7 in which an approach to estimate the statistical variability of damage computed from only one (Case 1) or few time-histories (Case 2) has been proposed. For each of the two cases, the thesis derived a confidence interval expression to enclose the (unknown) expected fatigue damage. An example confirmed the correctness of both confidence interval expressions. The example considered the stress power spectral density in an offshore platform. Sample statistics (mean and variance) of the damage from simulated time-histories were used to construct the confidence interval, which was then compared to the expected damage computed directly from the power spectrum (it represents the reference value needed by the analysis to check whether the confidence interval correctly encloses the expected damage, for a prescribed confidence). By replicating the analysis a large number of times and counting how many times the confidence interval encloses the expected damage, the analysis returned an estimated confidence of nearly 94.48% in either cases examined, a value almost coincident with the theoretical one 95% previously assumed. This confirmed the validity of the proposed approach.

It has to be pointed out that the theory of confidence intervals is well known in literature, but its specific application to the fatigue damage problems has never been proposed in the terms presented in this thesis. Furthermore, the proposed approach based on a direct analysis of time-history imposes no restriction on the specific type of random loading. They only require that the random loading be stationary.

Confidence intervals for the expected damage have also been verified by measured time-history records from a Mountain-bike. Several measured time-history records have been considered, from which the confidence intervals have been calculated

to enclose the expected damage. All measured time histories were qualified and quantified as being stationary random loadings when verified by different methods. The stationarity hypothesis of all measured time-history records was also verified by proposed damage-based run test of Chapter 6. The analysis results of one or more measured time-history records from the Mountain-bike confirm the correctness of confidence interval expressions. The confidence intervals were compared to the expected damage, which was approximated by the sample mean of several damage values (it represents a sort of calibrator sample value needed to check whether the confidence interval correctly encloses the expected damage). Results also showed that the damage computed from only one or few measured time-histories (thus ignoring its statistical variability) might lead to unsafe estimates of the expected damage. The use of the proposed approach is then recommended in this case.

It is also important to highlight that proposed confidence intervals for the expected damage and damage-based run test have been validated with real measurements. Consequently, they revealed to be not only in a good agreement with numerical simulations, but also a useful tool for engineers dealing with real engineering applications.

The last original contribution of this thesis is a new algorithm to implement the Carpinteri-Spagnoli-Vantadori (CSV) multiaxial fatigue criterion for random loading (Chapter 8). In most cases, the analysis of all nodal results in a finite element model is not needed since it may be restricted to small subsets of nodes from the most stressed regions; but, if it is not possible to predict a priori which regions are the most critical ones, such a new algorithm significantly shortens the computation time for the critical plane search.

The first phase of the work has been to write a Matlab routine to implement the method in its standard version, by obtaining a numerical code which is time-consuming despite the best efforts to improve the numerical aspects. The routine makes a systematic use of 'for/end' loops to scan, in the three-dimensional space, all the plane orientations in

a point, before the critical plane is exactly identified after five rotations. The presence of 'for/ends' loops leads the number of planes to be scanned to increase (and the time, accordingly) if the angular intervals are discretized into very closely spaced values. This situation is further enhanced when analyzing the nodal stress results in a finite element model, where the time required to complete just one critical plane search has to be multiplied by the number of nodes in the model, and that has motivated the proposal of a new algorithm able to shorten the computation time in such cases.

This goal has been achieved through a twofold strategy. The first aspect is calculating only those spectral parameters that the CSV method really needs to search for the critical plane. The second aspect is finding the analytical expressions of such a limited set of spectral parameters in any rotated reference frame, as a function both of the spectral parameters in the initial (un-rotated) frame and of the five rotation angles used to locate the critical plane.

In this way, the numerical routine does not compute unnecessary spectral parameters (e.g. the full PSD matrix and its spectral moments) in any rotated plane. The strategy leads to a routine completely free of 'for/end' loops, which are well-known to be the drawbacks of numerical computation.

As a consequence of free of 'for/end' loops, the new algorithm highlights a great advantage when analyzing the nodal stress results in an FE model, where the time required to complete just one critical plane search has to be multiplied by the number of nodes in the model. This advantage has been confirmed by means of two numerical examples.

It seems not superfluous to emphasize that the approach, herein applied to the spectral criterion by CSV, has in fact a general validity, as its theoretical framework may be applicable to any multiaxial spectral method in which the critical plane or the direction of maximum stress variance are identified through rotation angles or direction cosines.

BIBLIOGRAPHY

[AMZ94] Amzallag C, Gerey JP, Robert JL, Bahuaud J. Standardization of the rainflow counting method for fatigue analysis. Int. J. Fatigue 1994;16:287-293.

[AST85] ASTM Designation E 1049-85. Standard practices for cycle counting in fatigue analysis; 1985.

[BĘD92] Będkowski W, Macha E. Fatigue fracture plane under multiaxial random loadings – prediction by variance of equivalent stress based on the maximum shear and normal stress. Materialwiss. Werkstofftech. 1992;23:82–94.

[BEL07] Bel Knani K, Benasciutti D, Signorini A, Tovo R. Fatigue damage assessment of a car body-in-white using a frequency-domain approach. Int. J. Mater. Prod. Technol. 2007;30(1-3):172–198.

[BEN05a] Benasciutti D. Fatigue analysis of random loadings. Ph.D. thesis, Department of Engineering, University of Ferrara, Italy; 2005.

[BEN05b] Benasciutti D, Tovo R. Spectral methods for lifetime prediction under wide-band stationary random processes. Int. J. Fatigue 2005;27(8):867–77.

[BEN06] Benasciutti D, Tovo R. Comparison of spectral methods for fatigue analysis of broad-band Gaussian random processes. Probab. Eng. Mech. 2006;21(4):287–299.

[BEN07] Benasciutti D, Tovo R. Frequency-based fatigue analysis of non-stationary switching random loads. Fatigue Fract. Eng. Mater. Struct. 2007; 30(11) 1016-1029.

[BEN08] Benasciutti D, Cristofori A. A frequency-domain formulation of MCE method for multiaxal random loadings. Fatigue Fract. Eng. Mater. Struct. 2008;31(11): 937–948.

[BEN09a] Bengtsson A, Bogsjö K, Rychlik I. Uncertainty of estimated rainflow damage for random loads. Mar. Struct. 2009;22(2):261–274.

[BEN09b] Bengtsson A, Rychlik I. Uncertainty in fatigue life prediction of structures subject to Gaussian loads. Probab. Eng. Mech. 2009;24(2):224–235.

[BEN10a] Benasciutti D, Tovo R. On fatigue cycle distribution in non-stationary switching loadings with Markov chain structure. Probab. Eng. Mech. 2010; 25(4) 406–18.

[BEN10b] Benasciutti D, Tovo R. Frequency-based fatigue analysis of non-stationary switching random loads. Fatigue Fract. Eng. Mater. Struct. 2010;30(11):1016–1029.

[BEN10c] Bendat JS, Piersol AG. Random data: Analysis and measurement procedure. Hoboken: John Wiley & Sons, Inc.; 2010.

[BEN16a] Benasciutti D, Sherratt F, Cristofori A. Recent developments in frequency domain multi-axial fatigue analysis. Int. J. Fatigue 2016;91:397–413.

[BEN16b] Benasciutti D. Braccesi C, Cianetti F, Cristofori A, Tovo R. Fatigue damage assessment in wide-band uniaxial random loadings by PSD decomposition: outcomes from recent research. Int. J. Fatigue 2016;91(1):248–250.

[BEN18a] Benasciutti D, Carlet M, Zanellati D. A bandwidth correction to the Allegri-Zhang solution for accelerated random vibration testing. MATEC Web. Conf. 2018;165:07006.

[BEN18b] Benasciutti D, Tovo R. Frequency-based analysis of random fatigue loads: Models, hypotheses, reality. Materialwiss. Werkstofftech. 2018;49(3):345–367.

[BEN19a] Benasciutti D, Marques JME. An efficient procedure to speed up critical plane search in multiaxial fatigue: Application to the Carpinteri-Spagnoli spectral criterion. MATEC Web. Conf. 2019;300:16003.

[BEN19b] Benasciutti D, Zanellati D, Cristofori A. The "Projection-by-Projection" (PbP) criterion for multiaxial random fatigue loadings: Guidelines to practical implementation. Frattura Integr. Strutt. 2019;13(47):348–366.

[BEN64] Bendat JS. Probability functions for random responses: Prediction of peaks, fatigue damage, and catastrophic failures. NASA-CR-33; 1964.

[BEN86] Bendat JS, Piersol AG. Random data: analysis and measurement procedures. Wiley-Interscience, 1986.

[BER02] Berger C, Eulitz KG, Heuler P, Kotte KL, Naundorf H, Shuetz W, Sonsino CM, Wimmer A, Zener H. Betriebsfestigkeit in Germany – an overview. Int. J. Fatigue 2002;24:603-625.

[BRO00] Brodtkorb PA, Johannesson P, Lindgren G, Rychlik I, Rydén J, Sjö E. WAFO - a Matlab toolbox for the analysis of random waves and loads. Presented at 10th Int. Offshore and Polar Engineering Conference, Seattle, USA, May 27 - June 2, 2000, pp. 343–350

[BRO65] Brownlee KA. Statistical Theory and Methodology in Science and Engineering. 2nd ed., Wiley. New York, 1965

[BUC97] Buch A. Prediction of the comparative fatigue performance for realistic loading distributions. Prog. Aeosp. Sci. 1997;33:391–430.

[CAP20] Capponi L, Slavič J, Rossi G, Boltežar M. Thermoelasticity-based modal damage identification. Int. J. Fatigue 2020;137: 105661.

[CAR14] Carpinteri A, Spagnoli A, Vantadori S. Reformulation in the frequency domain of a critical plane-based multiaxial fatigue criterion. Int. J. Fatigue 2014;67:55–61.

[CAR16] Carpinteri A, Fortese G, Ronchei C, Scorza D, Vantadori S. Spectral fatigue life estimation for non-proportional multiaxial random loading. Theor. App. Fract. Mech. 2016;83:67–72.

[CAR17] Carpinteri A, Spagnoli A, Vantadori S. A review of multiaxial fatigue criteria for random variable amplitude loads. Fatigue Fract. Eng. Mater. Struct. 2017;40(7):1007–1036.

[CIA15] Cianetti F, Braccesi C, Lori G, Pioli D. Random multiaxial fatigue: A comparative analysis among selected frequency and time domain fatigue evaluation methods. Int. J. Fatigue 2015;74:107–118.

[COS18] Costa RC, Sagrilo LVS. Statistical uncertainty analysis in time-domain fatigue assessment of steel risers. J. Offshore Mech. Arct. Eng. 2018;140(3):031701-1–10.

[CRA62] Crandall SH, Mark WD, Khabbaz GR. The variance in Palmgren-Miner damage due to random vibration. In: Proceedings of the 4th US national congress of applied mechanics, vol. 1; 1962. p. 119–26.

[DAN64] Davenport AG. Note on the distribution of the largest value of a random function with application to gust loading. Proc. Inst. Civil. Eng. 1964;28:187–196.

[DIR85] Dirlik T. Application of computers in fatigue analysis. Ph.D. thesis. University of Warwick, UK; 1985.

[DOD73] Dodds CJ, Robson JD. The description of road surface roughness. J. Sound Vib. 1973;31(2):175–83.

[DOW72] Dowling NE. Fatigue failure predictions for complicated stress-strain histories. Journal of Materials JMLSA 1972;7(1):71-87.

[DOW88] Dowling NE. Estimation and correlation of fatigue lives for random loading. Int. J. Fatigue 1988;10(3):179-185.

[FAT98] Fatemi A, Yang L. Cumulative fatigue damage and life prediction theories: a survey of the state of the art for homogeneous materials. Int. J. Fatigue 1998;20(1):9–34.

[GAO08] Gao Z, Moan T. Frequency-domain fatigue analysis of wide-band stationary Gaussian processes using a trimodal spectral formulation. Int. J. Fatigue 2008;30(10–11):1944–55.

[GAO19] Gao DY, Yao WX, Wu T. A damage model based on the critical plane to estimate fatigue life under multi-axial random loading. Int. J. Fatigue 2019;129:104729.

[GRZ91] Grzelak J, Łagoda T, Macha E. Spectral analysis of the criteria for multiaxial random fatigue. Materialwiss. Werkstofftech. 1991;22:85–98.

[HAS73] Hasselmann K, Barnett TP, Bouws E, Carlson H, Cartwright DE, Enke K, Ewing JA, Gienapp H, Hasselmann DE, Kruseman P, Meerburg A, Müller P, Olbers DJ, Richter K, Sell W, Walden H. Measurements of wind-wave growth and swell decay during the joint North Sea wave project (JONSWAP). Deutsches Hydrographischen Zeitschrift 1973;A12:1–95.

[HOB16] Hobbacher A. Recommendations for fatigue design of welded joints and components. IIW document IIW-2259-15; 2016.

[HOL15] Holmes JD. Wind loading of structures. 3rd ed. Boca Raton: Taylor & Francis Group; 2015.

[ISO17] ISO/DIS 12107:2017 Metallic materials – Fatigue testing – Statistical planning and analysis of data.

[JOH95] Johannesson P, Lindgren G, Rychlik I. Rainflow modelling of random vehicle fatigue loads. ITM (Swedish Inst. Appl. Math.), Report 1995:5.

[JOH98] Johannesson P. Rainflow cycles for switching processes with Markov structure. Probab. Eng. Inform. Sci. 1998;12:143–75.

[JOH99] Johannesson P. Rainflow analysis of switching Markov loads. Ph.D. thesis, Mathematical Statistics, Centre for Mathematical Sciences, Lund Institute of Technology, Sweden; 1999.

[KIH95] Kihl DP, Sarkani S, Beach JE. Stochastic fatigue damage accumulation under broadband loadings. Int. J. Fatigue 1995;17(5):321–9.

[KRE83] Krenk S, Madsen PH. Stochastic response analysis. In: Thoft-Christensen P, editor. Reliability theory and its application in structural and soil mechanics. NATO Advanced Study Institute Series, Springer-Verlag; 1983, p. 103–172.

[LAL14] Lalanne C 2014. Random Vibrations Mechanical Vibration and Shock Analysis Random Vibration. 3rd ed. Vol. 3, John Wiley & Sons Inc, 2014.

[LAM10] Lambert S, Pagnacco E, Khalij L. A probabilistic model for the fatigue reliability of structures under random loadings with phase shift effects. Int. J. Fatigue 2010;32(2):463–474.

[LAR91] Larsen CE, Lutes LD. Predicting the fatigue life of offshore structures by the single-moment method. Probab. Eng. Mech. 1991;6(2):96–108.

[LIN87] Lindgren G, Rychlik I. Rain flow cycle distributions for fatigue life prediction under Gaussian load processes. Fatigue Fract. Eng. Mater. Struct. 1987;10(3):251-260

[LON84] Longuet-Higgins MS. Statistical properties of wave groups in a random sea state. Philos. Trans. R. Soc. Lond. Ser. A-Math. 1984;312(1521):219-250.

[LOR99] Lorenzo DS, Hull ML. Quantification of Structural Loading During Off-Road Cycling. J. Biomech. Eng. 1999; 121 399-405.

[LOW12] Low YM. Variance of the fatigue damage due to a Gaussian narrowband process. Struct. Saf. 2012;34(1):381–9.

[LOW14a] Low YM. Uncertainty of the fatigue damage arising from a stochastic process with multiple frequency modes. Probab. Eng. Mech. 2014;36:8–18.

[LOW14b] Low YM. A simple surrogate model for the rainflow fatigue damage arising from processes with bimodal spectra. Mar. Struct. 2014;38:72–88.

[LUT04] Lutes LD, Sarkani S. Random vibrations: analysis of structural and mechanical systems. 2nd ed. Burlington: Elsevier Butterworth–Heinemann; 2004.

[MAD86] Madsen HO, Krenk S, Lind NC. Methods of structural safety. Englewood Cliffs: Prentice-Hall; 1986.

[MAR19a] Marques JME, Benasciutti D, Tovo R. Uncertainties on fatigue damage under random loadings through spectral methods. In: Quaderni del DIEM - GMA - Atti di giornate di studio (12); 2019.

[MAR19b] Marques JME, Benasciutti D, Tovo R. Variance of fatigue damage in stationary random loadings: comparison between time- and frequency-domain results. Proc. Struct. Integrity 2019;24:398-07.

[MAR20a] Marques JME, Benasciutti D, Tovo R. Variability of the fatigue damage due to the randomness of a stationary vibration loading. Int. J. Fatigue 2020; 141 105891.

[MAR20b] Marques JME, Benasciutti D, Carpinteri A, Spagnoli A. An algorithm for fast critical plane search in computer-aided engineering durability analysis under multiaxial random loadings: Application to the Carpinteri-Spagnoli-Vantadori spectral method. Fatigue Fract. Eng. Mater. Struct. 2020;43(9):78–93.

[MAR20c] Marques JME, Benasciutti D. More on variance of fatigue damage in non-Gaussian random loadings – effect of skewness and kurtosis. Proc. Struct. Integrity 2020; 25: 101-111.

[MAR21a] Marques JME, Benasciutti D. A model to assess the variance of fatigue damage in high-kurtosis asymmetrical random loadings with narrow-band power spectrum. To be presented at FATIGUE 2021, Downing College, Cambridge, UK.

[MAR21b] Marques JME, Benasciutti D. Variance of the fatigue damage in non-Gaussian stochastic processes with narrow-band power spectrum. Manuscript under review in Struct. Saf. 2021.

[MAR21c] Marques JME. Confidence intervals for the expected damage in random loadings: Application to measured time-history records from a Mountain-bike. In press in IOP conf. ser., Mater. Sci. Eng. 2021.

[MAR61] Mark WD. The inherent variation in fatigue damage resulting from random vibration. Ph.D. thesis, Department of Mechanical Engineering, M.I.T., USA; 1961.

[MAT18] MATLAB. (2018). 9.7.0.1190202 (R2019b). Natick, Massachusetts: The MathWorks Inc.

[MAT68] Matsuishi M, Endo T. Fatigue of metals subjected to varying stress. Presented at Japan Society of Mechanical Engineers, Fukuoka, Japan; 1968.

[MCN10] McNeill SI. A method for determining the fatigue critical plane for biaxial random vibration in the frequency domain. Fatigue Fract. Eng. Mater. Struct. 2010;33(6):390–394.

[MIL54] Miles JW. On structural fatigue under random loading. J. Aeron. Sci. 1954;21(11):753–62.

[MIN45] Miner MA. Cumulative damage in fatigue. J. Applied Mechanics ASME 1945;67:A159-A164.

[MON14] Montgomery DC, Runger GC. Applied statistics and probability for engineers. 6th ed. Hoboken, NJ, USA: John Wiley & Sons; 2014.

[MRŠ13] Mršnik M, Slavič J, Boltežar M. Frequency-domain methods for a vibration-fatiguelife estimation–application to real data. Int. J. Fatigue 2013;47:8–17.

[MRŠ18] Mršnik M, Slavič J, Boltežar M. Vibration fatigue using modal decomposition. Mech. Syst. Signal Proc. 2018;98:548–556.

[NIE07] Niesłony A, Macha E. Spectral method in multiaxial random fatigue. Berlin: Springer; 2007.

[NIE16] Niesłony A, Böhm M. Frequency-domain fatigue life estimation with mean stress correction. Int. J. fatigue 2016;91(2):373–381.

[NIE20] Niesłony A, Böhm M, Owsiński R. Formulation of multiaxial fatigue failure criteria for spectral method. Int. J. fatigue 2020;135:105519.

[NIK01] Nikolaidis E, Wang H, Jha A, Ghiocel D. Fatigue reliability of cars under road-induced cyclostationary excitation. Int. J. Mater. Prod. Technol. 2001;16:404–416

[OCH94] Ochi MK, Ahn K. Probability distribution applicable to non-Gaussian random processes. Prob. Eng. Mech. 1994;9:255–64.

[PAR62] Parzen E. Stochastic processes. Oakland: Holden-Day; 1962.

[PET04] Petrucci G, Zuccarello B. Fatigue life prediction under wide band random loading. Fatigue Fract. Eng. Mater. Struct. 2004;27(12):1183–95.

[PIE64] Pierson Jr. WJ, Moskowitz L. A proposed spectral form for fully developed wind seas based on the similarity theory of S. A. Kitaigorodskii. J. Geophys. Res. 1964;69(24):5181–90.

[PIT01] Pitoiset X, Rychlik I, Preumont A. Spectral methods to estimate local multiaxial fatigue failure for structures undergoing random vibrations. Fatigue Fract. Eng. Mater. Struct. 2001;24:715–27.

[PRE85] Preumont A. On the peak factor of stationary Gaussian processes. J. Sound Vibr. 1985;100(1):15–34.

[RIC44] Rice SO. Mathematical analysis of random noise. Bell Syst Tech J 1944;23:282–32.

[ROU14] Rouillard V. Quantifying the Non-stationarity of vehicle vibrations with the run test. Packag. Technol. Sci. 2014; 27 203–19.

[RYC03] Rychlik I. Five lectures on reliability applications of Rice's formula for the intensity of level crossings. In: Jendo S, Dolinski K, editors. Course on Reliability-Based Design and Optimisation, Warsaw: Institute of Fundamental Technological Research; 2003, p. 241–323

[RYC87] Rychlik I. A new definition of the rain-flow cycle counting method. Int. J. Fatigue 1987;9(2):119-121.

[RYC93] Rychlik I. On the ‘narrow-band’ approximation for expected fatigue damage. Probab. Eng. Mech. 1993;8(1):1–4.

[SAR94] Sarkani S, Kihl DP, Beach JE. Fatigue of welded joints under narrowband non-Gaussian loadings. Probab. Eng. Mech. 1994;9:179–90.

[SCH96] Schütz W. A history of fatigue. Eng. Fract. Mech. 1996;54(2):263-300.

[SMA05] Smallwood DO. Generating non-Gaussian vibration for testing purposes. Sound and Vibration 2005;39(10):18–24.

[SMA93] Smallwood DO, Paez TL. A frequency domain method for the generation of partially coherent normal stationary time domain signals. Shock Vib. 1993;1(1):45-53.

[SON07a] Sonsino CM. Course of SN-curves especially in the high-cycle fatigue regime with regard to component design and safety. Int. J. Fatigue 2007;29(12):2246-2258.

[SON07b] Sonsino CM. Fatigue testing under variable amplitude loading. Int. J. Fatigue 2007;29(6):1080–9.

[SUS10] Susmel L. A simple and efficient numerical algorithm to determine the orientation of the critical plane in multiaxial fatigue problems. Int. J. Fatigue 2010;32(11):1875–1883.

[SVE97] Svensson T. Prediction uncertainties at variable amplitude fatigue. Int. J. Fatigue, 1997;19(Suppl.1):S295-S302.

[TOV01] Tovo R. On the fatigue reliability evaluation of structural components under service loading. Int. J. Fatigue 23:587-598.

[VAN18] Vantadori S, Haynes R, Fortese G, Habtour E, Ronchei C, Scorza D, Zanichelli A. Methodology for assessing embryonic cracks development in structures under high-cycle multiaxial random vibrations. Fatigue Fract. Eng. Mater. Struct. 2018;41(1):20–28.

[VAN19] Vantadori S, Fortese G, Carpinteri A. Shape of the power spectral density matrix components: Influence on fatigue damage. Fatigue Fract. Eng. Mater. Struct. 2019;42(7):972–987.

[VAN72] Vanmarcke EH. Properties of spectral moments with applications to random vibration. J. Eng. Mech. Div. - ASCE 1972;98(EM2):425-446.

[WAL40] Wald A, Wolfowitz J. On a test whether two samples are from the same population. Annals of Math. Stat. 1940; 11 147-62.

[WEB99] Weber B, Kenmeugne B, Clement JC, Robert JC. Improvements of multiaxial fatigue criteria computation for a strong reduction of calculation duration. Comput. Mater. Sci. 1999;15(4):381–399.

[WIN85] Winterstein SR. Non-normal responses and fatigue damage. J. Eng. Mech. ASCE 1985;111(10):1291-95.

[WIN88] Winterstein SR. Nonlinear vibration models for extremes and fatigue. J. Eng. Mech. ASCE 1988;114(10):1772–90.

[WIN94] Winterstein SR, Ude TC, Kleiven G. Springing and slow-drift responses: predicted extremes and fatigue vs. simulation. In: BOSS'94 Proceedings of the seventh international conference on the behaviour of offshore structures, M.I.T.; 1994.

[WIR76] Wirsching PH, Preasthofer PH. Preliminary dynamic assessment of deepwater platforms. J. Struct. Div. - ASCE 1976;102(7):1447-62.

[WIR80] Wirsching PH, Light MC. Fatigue under wide band random stresses. J. Struct. Division 1980;106(7):1593–607.

[WIR95] Wirsching PH, Paez TL, Ortiz K. Random Vibrations: Theory and Practice. New York: John Wiley & Sons; 1995.

[ZHA92] Zhao W, Baker MJ. On the probability density function of rainflow stress range for stationary Gaussian processes. Int. J. Fatigue 1992;14(2):121–35

Appendix A

CONFIDENCE INTERVAL EXPRESSION OF ONE TIME-HISTORY

The issue of statistical variability of the fatigue damage is addressed in Chapter 7 by confidence interval expressions to enclose the (unknown) expected fatigue damage. A common situation is that in which only one time-history $x(t)$ is available. For this situation, the confidence interval for $E[D(T)]$ is based on the idea of dividing a single time-history into N_B blocks without overlapping (see Chapter 7). By underlying values, which originate from the block subdivision, e.g. N_B, $\overline{D}_\mathrm{B}(T_\mathrm{B})$ and $\hat{\sigma}^2_{\mathrm{D_B}}$, it is convenient to rewrite a small number of formulae.

The damage of the entire time-history $x(t)$ sums up the damage of all blocks:

$$D(T) \cong \sum_{\mathrm{i}=1}^{\mathrm{N_B}} D_{\mathrm{B,i}}(T_\mathrm{B}) = N_\mathrm{B} \cdot \overline{D}_\mathrm{B}(T_\mathrm{B}) \tag{A.1}$$

The sample mean of the damage of all blocks in Eq. (A.1) is $\overline{D}_\mathrm{B}(T_\mathrm{B}) = N_\mathrm{B}^{-1} \sum_{\mathrm{i}=1}^{\mathrm{N_B}} D_{\mathrm{B,i}}(T_\mathrm{B})$. In its turns, the variance σ^2_D of the damage of the whole time-history $x(t)$ is:

$$\sigma_{\mathrm{D}}^2 = \mathrm{Var}\left[\sum_{\mathrm{i}=1}^{\mathrm{N_B}} D_{\mathrm{B,i}}(T_{\mathrm{B}})\right] \cong N_{\mathrm{B}} \cdot \hat{\sigma}_{\mathrm{D_B}}^2 \tag{A.2}$$

The variance σ_{D}^2 in Eq. (A.2) is approximated using the sample variance of all blocks $\hat{\sigma}_{\mathrm{D_B}}^2 = (N_{\mathrm{B}} - 1)^{-1} \sum_{\mathrm{i}=1}^{\mathrm{N_B}} \left[D_{\mathrm{B,i}}(T_{\mathrm{B}}) - \overline{D}_{\mathrm{B}}(T_{\mathrm{B}})\right]^2$.

This section aims to explain how the final confidence interval expression for $E[D(T)]$ when considering only one time-history $x(t)$ is derived. The starting point is the confidence interval for the expected damage of a single block, which follows the definition of a normally distributed random variable with unknown mean and unknown variance [MON14]. Accordingly, the confidence interval for $E[D_{\mathrm{B}}(T_{\mathrm{B}})]$ using N_{B} damage values, the sample mean $\overline{D}_{\mathrm{B}}(T_{\mathrm{B}})$ and the sample variance $\hat{\sigma}_{\mathrm{D_B}}^2$ is calculated as [MAR20a]:

$$\overline{D}_{\mathrm{B}}(T_{\mathrm{B}}) - \frac{t_{\mathrm{dof},\beta/2} \cdot \hat{\sigma}_{\mathrm{D_B}}}{\sqrt{N_{\mathrm{B}}}} \leq E[D_{\mathrm{B}}(T_{\mathrm{B}})] \leq \overline{D}_{\mathrm{B}}(T_{\mathrm{B}}) + \frac{t_{\mathrm{dof},\beta/2} \cdot \hat{\sigma}_{\mathrm{D_B}}}{\sqrt{N_{\mathrm{B}}}} \tag{A.3}$$

Multiplying this expression by the number of blocks N_{B} yields:

$$\begin{aligned} &N_{\mathrm{B}}\left(\overline{D}_{\mathrm{B}}(T_{\mathrm{B}}) - \frac{t_{\mathrm{dof},\beta/2} \cdot \hat{\sigma}_{\mathrm{D_B}}}{\sqrt{N_{\mathrm{B}}}}\right) \leq N_{\mathrm{B}} \cdot E[D_{\mathrm{B}}(T_{\mathrm{B}})] \\ &\leq N_{\mathrm{B}}\left(\overline{D}_{\mathrm{B}}(T_{\mathrm{B}}) + \frac{t_{\mathrm{dof},\beta/2} \cdot \hat{\sigma}_{\mathrm{D_B}}}{\sqrt{N_{\mathrm{B}}}}\right) \end{aligned} \tag{A.4}$$

Since N_{B} is deterministic [MAR20a], the expected value of Eq. (A.1) results in:

$$E[D(T)] = E\left[\sum_{\mathrm{i}=1}^{\mathrm{N_B}} D_{\mathrm{B,i}}(T_{\mathrm{B}})\right] = N_{\mathrm{B}} \cdot E[D_{\mathrm{B}}(T_{\mathrm{B}})\,] \tag{A.5}$$

This result can also be obtained by noting that $E[D_{\mathrm{B}}(T_{\mathrm{B}})] = (T_{\mathrm{B}}/T) \cdot E[D(T)]$. Substituting into Eq. (A.4) and considering the approximation $\hat{\sigma}_{\mathrm{D}} \cong \sqrt{N_{\mathrm{B}}} \cdot \hat{\sigma}_{\mathrm{D_B}}$ of Eq. (A.2), the confidence interval expression for $E[D(T)]$ when considering only one time-history $x(t)$ is [MAR20a]:

$$D(T) - t_{\mathrm{dof},\beta/2} \cdot \hat{\sigma}_{\mathrm{D}} \leq E[D(T)] \leq D(T) + t_{\mathrm{dof},\beta/2} \cdot \hat{\sigma}_{\mathrm{D}} \tag{A.6}$$

which coincides with the confidence interval expression also reported in Chapter 7.

Appendix B

EXPRESSIONS OF THE ELAPSED TIME FOR THE STANDARD ALGORITHM

This section develops the analytical equations to estimate the elapsed time for the standard algorithm in Chapter 8. They refer to one and multiple simulation runs. In a single simulation run, for the sequence of 'for/end' loops in the Matlab code (see Chapter 8), the number of scanned planes in one simulation run is $n_{\mathrm{p}} = n_{\phi} n_{\theta} + n_{\psi} + n_{\gamma}$. Based on the interval width (in degrees) over which each angle is defined, the expression can be written as a function of a common value of Δ:

$$\begin{aligned} n_p &= \left(\frac{360}{\Delta} + 1\right)\left(\frac{180}{\Delta} + 1\right) + \left(\frac{360}{\Delta} + 1\right) + \left(\frac{360}{\Delta} + 1\right) \\ &= 3 + \frac{1260}{\Delta} + \frac{64800}{\Delta^2} \end{aligned} \tag{B.1}$$

The first constant term is generally negligible compared to the others. As Δ becomes very small ($\Delta \leq 3°$), the third term dominates over the others, and n_{p} approximates as follows:

$$n_{\mathrm{p}} \cong \frac{64800}{\Delta^2} \qquad \text{for } \Delta \leq 3° \tag{B.2}$$

This formula also shows that, in the limit $\Delta \to 0°$, it is $n_{\mathrm{p}} \to \infty$ (and the elapsed time, too), which confirms how the resolution cannot decrease indefinitely if the simulation time has to remain within acceptable limits.

The goal is to find the expression of the simulation (or elapsed) time $T_1(n_{\mathrm{p}})$ after which the standard algorithm completes the critical plane search in one run (that is, after it analyses one stress PSD matrix).

Some preliminary assumptions can be made. First, the computer has a 'linear' behavior. This means that, if 10 seconds are required to analyze 1 plane position (in 1 iteration in a 'for/end' loop), then 20 seconds are required to complete 2 iterations, 30 seconds for 3 iterations, and so on. Secondly, the computation time was demonstrated (via preliminary simulations) to be directly proportional to the number of points n_{f} in the PSD frequency axis. This condition sounds obvious, as it is related to the basic mathematical operations and storage capacity of Matlab.

Based on these two assumptions, the elapsed time can be written as $T_1(n_{\mathrm{p}}) = A_{\mathrm{PC}} \cdot n_{\mathrm{f}} \cdot n_{\mathrm{p}}$, where n_{f} is the number of frequency points, and A_{PC} is a parameter calibrated on the computer characteristics. The final expression then is:

$$T_1(n_{\mathrm{p}}) = A_{\mathrm{PC}} n_{\mathrm{f}} \left(3 + \frac{1260}{\Delta} + \frac{64800}{\Delta^2}\right) \tag{B.3}$$

or simplified if $\Delta \leq 3°$:

$$T_1(n_{\mathrm{p}}) \cong A_{\mathrm{PC}} n_{\mathrm{f}} \frac{64800}{\Delta^2} \tag{B.4}$$

Obviously, Eq. (B.3) and (B.4) hold for 1 simulation run. If the algorithm has to be applied iteratively to locate a number of critical planes equal to n_{runs}, the elapsed time

can be written as $T_{\mathrm{tot}}(n_{\mathrm{runs}}) = n_{\mathrm{runs}} \cdot T_1(n_{\mathrm{p}})$. This expression, too, follows from the hypothesis of a 'linear' computer (i.e. if T_1 is the time to search for 1 critical plane, then $n_{\mathrm{runs}} \cdot T_1$ is the time to search for n_{runs} planes). By substituting the expression for $T_1(n_{\mathrm{p}})$, it is possible to obtain:

$$T_{\mathrm{tot}}(n_{\mathrm{runs}}) = A_{\mathrm{PC}}\, n_{\mathrm{f}} \left(3 + \frac{1260}{\Delta} + \frac{64800}{\Delta^2}\right) n_{\mathrm{runs}} \tag{B.5}$$

This shows that T_{tot} versus n_{runs} is a straight line, with slope inversely proportional to Δ.

It now comes easy to determine the constant A_{PC}. The number of frequency points, n_{f}, is known from the power spectra $G_{\mathrm{ij}}(f)$ to be analysed. It is convenient to choose a large Δ value (for example, 20°) so that the simulation will not be so time-demanding, and then to measure the corresponding time $\tilde{T}_{\mathrm{tot}}(1)$ to complete 1 simulation run ($n_{\mathrm{runs}} = 1$). The constant A_{PC} follows by inverting Eq. (B.3). For the example in Chapter 8, $n_{\mathrm{f}} = 1247$ and $n_{\mathrm{p}} = 228$ planes (for $\Delta = 20°$). For one simulation run ($n_{\mathrm{runs}} = 1$), the measured elapsed time is $\tilde{T}_{\mathrm{tot}}(1) = 6.716$ seconds (the 64-bit computer has CPU 3.8 GHz, 32 GB RAM). By inverting the previous equation, $A_{\mathrm{PC}} = 2.362 \cdot 10^{-5}$ seconds is obtained. Eq. (B.5) can now be extrapolated to other values of n_{runs}. For example, for $\Delta = 10°$ and $n_{\mathrm{runs}} = 15000$, the computation time would be approximately 95 hours.

ACKNOWLEDGEMENTS

I would like to thank my supervisor Denis Benasciutti and co-supervisor Roberto Tovo who played an important role during my PhD. They have always supported me and have given me enthusiasm for science. I am very grateful for their contribution that has raised the quality of this thesis. In particular, I feel deeply indebted to Denis Benasciutti for his invaluable guidance, encouragement, and generous help.

Thanks to the referees, Adam Niesłony and Filippo Cianetti, for their helpful comments during the review process of this thesis.

My thankfulness is also to my ex-colleague and friend, Davide Zanellati, for all discussions and helpful suggestions.

My gratitude also goes to my family, There and Michele, for their love.

Finally, I consider myself to be extremely fortunate to have had the great opportunity to work with Tovo-Benasciutti research group at the Department of Engineering of the University of Ferrara.